

AD _____

Award Number: W81XWH-05-1-0221

TITLE: Development of an Automated Modality-Independent
Elastographic Image Analysis System for Tumor Screening

PRINCIPAL INVESTIGATOR: Jao J. Ou

CONTRACTING ORGANIZATION: Vanderbilt University
Nashville, TN 37235

REPORT DATE: February 2008

TYPE OF REPORT: Annual Summary

PREPARED FOR: U.S. Army Medical Research and Materiel Command
Fort Detrick, Maryland 21702-5012

DISTRIBUTION STATEMENT: Approved for Public Release;
Distribution Unlimited

The views, opinions and/or findings contained in this report are those of the author(s) and should not be construed as an official Department of the Army position, policy or decision unless so designated by other documentation.

REPORT DOCUMENTATION PAGE				Form Approved OMB No. 0704-0188	
Public reporting burden for this collection of information is estimated to average 1 hour per response, including the time for reviewing instructions, searching existing data sources, gathering and maintaining the data needed, and completing and reviewing this collection of information. Send comments regarding this burden estimate or any other aspect of this collection of information, including suggestions for reducing this burden to Department of Defense, Washington Headquarters Services, Directorate for Information Operations and Reports (0704-0188), 1215 Jefferson Davis Highway, Suite 1204, Arlington, VA 22202-4302. Respondents should be aware that notwithstanding any other provision of law, no person shall be subject to any penalty for failing to comply with a collection of information if it does not display a currently valid OMB control number. PLEASE DO NOT RETURN YOUR FORM TO THE ABOVE ADDRESS.					
1. REPORT DATE 25-02-2008		2. REPORT TYPE Annual Summary		3. DATES COVERED 26 JAN 2007 - 25 JAN 2008	
4. TITLE AND SUBTITLE Development of an Automated Modality-Independent Elastographic Image Analysis System for Tumor Screening				5a. CONTRACT NUMBER	
				5b. GRANT NUMBER W81XWH-05-1-0221	
				5c. PROGRAM ELEMENT NUMBER	
6. AUTHOR(S) Jao J. Ou Email: jjo@alumni.duke.edu				5d. PROJECT NUMBER	
				5e. TASK NUMBER	
				5f. WORK UNIT NUMBER	
7. PERFORMING ORGANIZATION NAME(S) AND ADDRESS(ES) Vanderbilt University Nashville, TN 37235				8. PERFORMING ORGANIZATION REPORT NUMBER	
9. SPONSORING / MONITORING AGENCY NAME(S) AND ADDRESS(ES) U.S. Army Medical Research and Materiel Command Fort Detrick, Maryland 21702-5012				10. SPONSOR/MONITOR'S ACRONYM(S)	
				11. SPONSOR/MONITOR'S REPORT NUMBER(S)	
12. DISTRIBUTION / AVAILABILITY STATEMENT Approved for Public Release; Distribution Unlimited					
13. SUPPLEMENTARY NOTES					
14. ABSTRACT The objective of this project is to further develop modality-independent elastography as a system that is able to reproducibly detect regions of increased stiffness within the breast based on pre- and post- compression input images of the anatomy. As stated in the proposal, the original specific aims are concerned with enhancement of the method, investigation of texture and statistical analyses for evaluating the success of the method, and engineering of a device that can generate proper forces on mock setups within current available clinical imaging systems. To date, progress on each of these aims has been made in handling increased computational complexity, developing and testing metrics for the evaluation of reconstructions, and the fabrication of a compression chamber tested on a tissue-like polymer phantom.					
15. SUBJECT TERMS elastography, breast cancer screening, image processing					
16. SECURITY CLASSIFICATION OF:			17. LIMITATION OF ABSTRACT	18. NUMBER OF PAGES	19a. NAME OF RESPONSIBLE PERSON
a. REPORT	b. ABSTRACT	c. THIS PAGE			USAMRMC
U	U	U	UU	65	19b. TELEPHONE NUMBER (include area code)

Table of Contents

	Page
Introduction.....	1
Body.....	1
Key Research Accomplishments.....	6
Reportable Outcomes.....	6
Conclusions.....	7
References.....	7
Appendices.....	8

Introduction

An important initial screening step in the detection of breast cancer is the ability to identify select areas of atypical density that require further evaluation. Currently, mammography is the clinical standard for screening and provides useful but at times ambiguous information, which can necessitate further invasive workup of benign lesions. Alternative methods such as elastography have shown potential in enhancing the diagnostic process by providing information about the tissue composition [1, 2]. Modality-independent elastography (MIE) is a novel image processing technique that combines finite element models of soft-tissue deformation with measures of image similarity in order to reconstruct elastic property distributions throughout the tissue. The basic requirements for the method are two images of the tissue in different states of deformation (e.g. compression). MIE then updates the estimate of the material properties via a matching process between the two images. The final result is a map of the breast (or other tissue of interest) that reflects material inhomogeneity, such as in the case of a tumor mass that disrupts the surrounding structure of normal tissue. Because MIE works on probing the differences between images, it can be used to not only work in concert with more traditional screening techniques but also address a possible gap when those methods are unable to directly discern tissues of interest.

Body

As stated in the original proposal, three main aims of this project are to (1) expand and refine the current MIE technique to enhance its efficiency and capabilities, (2) to perform analyses on texture in input images and quantify statistical parameters capable of estimating and evaluating the success of elastographic reconstruction, and (3) to engineer a device that can accurately produce compressive forces necessary for phantom setups within current imaging systems, providing the basis for a future device that can be used in a clinical setting. In this past year, progress on all three aims has been made. The original specific aim and the relevant proposed work for each is listed below and addressed.

Specific Aim #1 stated: “To expand and refine the current MIE technique to enhance its efficiency, as well as add new capabilities such as handling a full 3D or combined 2D/3D elastodynamic model for improved accuracy.”

A framework utilizing parallel processing techniques has been designed and implemented to accommodate a fully three-dimensional version of the MIE algorithm. A key component, but also the bottleneck, of the MIE methodology is the calculation of a Jacobian matrix sensitive to spatial discretization. Each column of the Jacobian matrix represents a single “forward solve” of the problem and corresponds to a single ‘elasticity region’ within the domain, encompassing a solution of the finite element model, image deformation, and similarity metric calculation. In 2D, a fairly large number of regions (about 400) were already needed to adequately sample the area of study and attempt to search for a presumed lesion. For an organ that is most properly analyzed as a three-dimensional system, such as the breast, our initial empiric calculations indicated that the increase in dimensionality would necessitate upwards of 3200 regions to be partitioned over a [typical] volume. In this case, the size of the finite element model itself is increased by nearly two orders of magnitude as well. It was therefore apparent that the code

complexity and computational resource demands of 3D MIE far surpass the capabilities of the original 2D MATLAB/FORTRAN/LAPACK design. In order to perform what would otherwise be an intractable computational problem, the MPI standard of parallel communication was used to split up the Jacobian formation process as a static SPMD (single-process, multiple-data) scheme within a C/C++ Gauss-Newton optimization. In addition, the Portable Extensible Toolkit for Scientific Computation (PETSc) toolkit [3,4] was interfaced to provide the necessary efficient sparse matrix system solvers. We utilized a share of 100 CPUs on the Vanderbilt University Advanced Computing Center for Research and Education cluster to demonstrate that each iteration of the optimization could be achieved on the order of 30 minutes, as opposed to original estimates on available sequential processing machines of upwards of 5000 minutes. We note, however, that to effectively traverse the entire multi-dimensional objective function space requires several (perhaps tens of) iterations would be required, underscoring the innately high computational load of the method.

We have completed a preliminary study that demonstrates the new MIE framework in action, using simulated deformation based on clinical data obtained from both CT and MR scans. The test cases involved the simulated implantation of a stiff and radiographically occult 2-cm spherical tumor at the center of the breast. Guided by a finite element mesh deformation using prescribed boundary displacements (designed to mimic a compression source as described in Specific Aim 3), a target image volume was created. Discretizations of the model and image domains as per the MIE methodology were then used to reconstruct the inclusion. In both cases, MIE indicated that a lesion $\sim 2\times$ stiffer than surrounding tissue existed and was localized to the known position. However, due to inexact partitioning of the mesh elements, the algorithm actually detected a tumor closer to 3 cm in diameter, leading to a pseudo-compensatory decrease in elasticity contrast in the model (the true difference in stiffness was a factor of 6). This was explained by performing an *a priori* classification of the mesh elements into two material types according to their spatial membership in the 3200 regions. After this adjustment in overlap, the constrained reconstructions much more favorably followed an objective function minimization that resulted in a stiffness contrast matching the original reconstruction. Based on these experiments, it is our current assertion that shaping the objective function by dynamically rearranging the spatial discretization of the model during the optimization can lead to improved elasticity contrast resolution, and studies are underway to address this issue. The details of the work described are provided within Appendix A of this document.

As a further note, we acknowledge that originally proposed work involving the use of a combined 2D-3D model is still being considered as a means of reducing the scope of the problem with respect to dimensionality. However, the current implementation is deemed viable with sufficient allocation of computational resources. In addition, further research into the effects of dimensionality was pursued in the context of another possible application for MIE, that is, in dermoscopic examination. We simulated a spectrum of geometrical variation in size for a posited lesion embedded within skin (e.g. radius and depth of penetration). Our findings indicate that while a thin-membrane system is capable of differentiating a stiff object from its surroundings for most scenarios, inevitably, a 2D approximation of the model has its limitations, and it is quite difficult to avoid the need to account for full spatial dimensionality. For further discussion, please refer to Appendix B of this document.

Specific Aim #2 stated: “**To perform texture analysis on input images in order to quantify a statistical parameter capable of estimating the success of elastographic reconstruction.**”

Tolerance to improper input has been tested with statistical quantification of reconstruction success. Our observations during the ongoing development and testing of the MIE method prompted questions concerning the quality of data necessary and sufficient to achieve satisfactory results, as well as how to evaluate the fidelity of the reconstructed elasticity image. The primary inputs to the reconstruction method are the acquired images and the delineated boundary conditions on the domain. Our investigation began by examining a two-dimensional system and attempting to defeat the algorithm with increasing levels of degraded input. We briefly summarize the key results of these studies as described in a previous Annual Report. The first experiment used additive image noise to obscure the underlying texture to reflect possible scenarios of corruption during acquisition. Noise fields were created from a zero-mean Gaussian random distribution along the variance of non-background pixels and scaled according to the total power at 1, 5, 10, 15, 20, 25, and 30%. It was found that the reconstruction was tolerant of image noise up to approximately 10%. Figure 1 demonstrates the degradative effects of image noise. The second experiment involved boundary condition selection error. A gold standard set of boundary conditions known to produce an accurate reconstruction was modified using randomized vectors of equal magnitude (0.1, 0.2, 0.3, 0.5, 0.75, 1.0, 1.5, and 2.0 pixel units) reflecting a range of typical localization skill for users from poor to expert. It was noted that randomizing all the vectors can actually result in twisting of elements that resulted in significant alterations of displacements in the interior of the mesh, leading to grossly inaccurate model deformations.

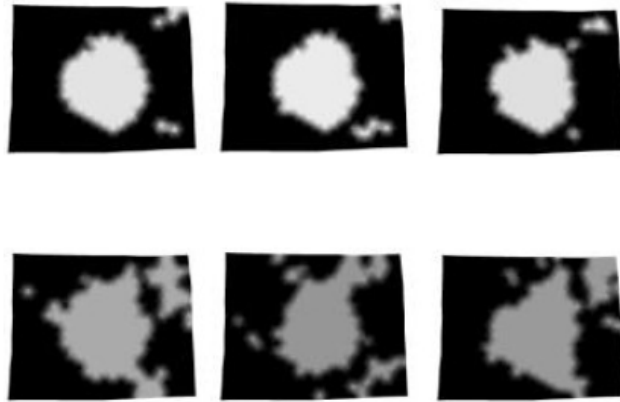


Figure 1. 2D reconstructions resulting from the distortion of the target image using additive Gaussian random noise (from top left: 1, 5, 10, 20, 25, 30%). The true elasticity distribution is a centrally located and roughly circular region, and the noise progressively confounds the reconstruction.

We also note that the ‘quality of reconstruction score’ (QRS) was developed within the context of this project in order to quantify the retrospective localization accuracy of the method. In comparison and conjunction with more standard measures in the elastography field such as contrast-to-noise ratio [5], QRS has been used to determine relevant positional and material characterization in both simulation and data studies. The metric is determined by a classification of the reconstruction [6] that is then compared to the (known) segmentation of the actual

elasticity distribution. By examining the rate of accurately selecting an element of the domain to be of the correct material class, a conditional probability closely related to the positive predictive value of the test is obtained; we have determined *a posteriori* that a QRS>80% is typically indicative of a successful reconstruction. The use of QRS was similarly applied to the analysis of our 3D MIE simulation reconstruction experiments as included in Appendix A.

While we are continuing to examine the possibility of analyzing image texture prospectively for the purposes of predicting MIE success, we acknowledge that variability among acquisition systems and subjects has thus far made this extremely difficult. Proposed work involving the use of a feature tracking and frequency domain analysis is under investigation but not completed at this time. As more data is collected, it is hoped that establishing a pattern for understanding the reconstruction algorithm behavior will become statistically relevant. However, partially based on our preliminary findings, we believe that the natural heterogeneity of tissue is typically sufficient for reconstruction purposes. Our efforts have therefore been refocused on addressing the practical aspects of implementing MIE outside of an *in silico* environment, especially with regards to the degradation of quality due to the (mis)estimation in the process of boundary condition assignment. It is the propagation of error from this source into the model and downstream to the other components of the algorithm that appears to be the greatest contributor in an unsatisfactory reconstruction (as demonstrated in the work presented in Appendix A and C). In pursuing this line of work, a number of novel as well as standard means for determining point correspondence to provide an accurate surface registration have been developed and tested. At this time, our conclusion is that utilizing a thin-plate spline is the best method. Because this requires the tracking of surface markers, an level set-matching method using Laplace's equation is deemed appropriate for use in the event that such fiducials are not available.

Specific Aim #3 stated: **“To engineer a device that can accurately produce compressive forces necessary for phantom setups within current clinical imaging systems, providing the basis for a future device that can be used in a clinical setting.”**

A compression device has been constructed and tested in magnetic resonance (MR) and X-ray computed tomography (CT) imaging systems using a polyvinyl alcohol phantom and contrast agents. The compression device is composed of a rectangular Plexiglas frame that traps the phantom in at least two directions with a sliding wall and the compression plate, which houses an air bladder in a polycarbonate frame (see Figure 2). When inflated, the air bladder provides a deformation of up to 5 cm. The prototypical phantom used has been fabricated as a polyvinyl alcohol cryogel (~250 cc, 7% wt/vol) in a manner consistent with the methods presented in [7, 8]. A notable difference in the manufacturing process has been the addition of 10% v/v glycerol to the base solution. A spherical mold is used to create a tumor replica after the application of a 24-hour freeze-thaw cycle, which is then suspended within a primary mold for the phantom and frozen again within the remaining bulk material. Contrast agents (e.g. iodine, barium, or copper sulfate) are added as needed to provide intensity variation depending on the imaging modality. The result is a domed breast-like shape approximately 10-11 cm at the base and tapering over a depth of about 5-6 cm. A study of this system as used in a CT scanner has been completed, with elastic contrasts obtained by MIE reconstruction having been compared against independent mechanical testing of the cryogel materials. Key results obtained are being prepared for a manuscript to be submitted soon after the preparation of this report.

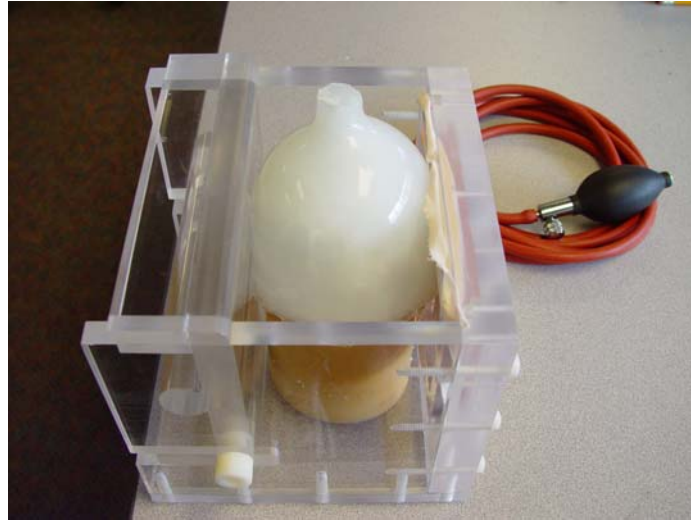


Figure 2. Top row: Photographs of the polyvinyl alcohol phantom inside the compression device without (left) and with compression (right).

A prototype compression chamber that is more clinically oriented has been designed to fit into the chassis of a Philips Intera MR breast coil unit. It has been fabricated from clear acrylic tube segments in which the air bladders are attached using polycarbonate pins and then covered with an expandable nylon sheet. A small series of human volunteer trials have been performed to test the usage of the device. To this date, no negative feedback has been given regarding its effects on the patient. Figure 3 below shows the schematic design of the system as well as an overhead view of its assembly.

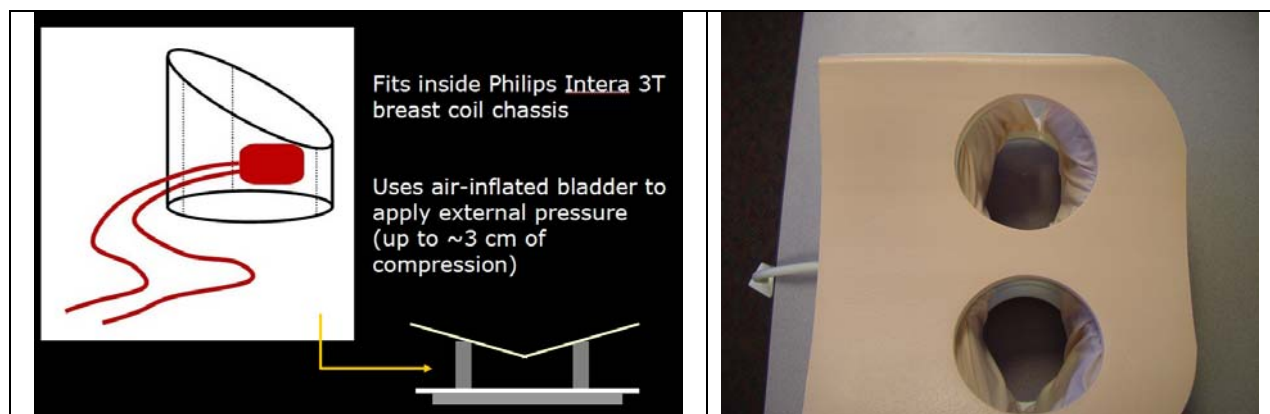


Figure 3. Left: Schematic of compression device designed for clinical use breast coil. Right: Photograph of assembly looking down into the Philips Intera chassis.

Key Research Accomplishments

- 3D implementation – Computationally complex challenges have been addressed to create an effective parallelized version of MIE for full three-dimensional analysis
- Phantom and material creation – design, fabrication, and testing of PVA-C for the creation of appropriate tissue mimicking systems
- Testing with phantoms – Initial testing has been performed on semi-anthropomorphic and appropriate breast phantoms for elastography research. Initial testing has also been performed on phantoms designed for surgical simulations

Reportable Outcomes

Work on the MIE method during this period has resulted in three conference papers and an additional poster presentation as well as acceptance of a peer-reviewed journal article. Didactic coursework requirements for the PhD degree have been completed at this time as well as successful presentation of the thesis proposal to a faculty committee.

Poster Presentations

Vanderbilt University Medical Scientist Training Program retreat (June 2006)

Conference papers

M. I. Miga, J. J. Ou, and D. L. Ellis, 'An elastography framework for use in dermoscopy', Medical Imaging 2007: Physiology, Function and Structure from Medical Images, San Diego, CA.

J. J. Ou, R. E. Ong, and M. I. Miga, 'An Evaluation of 3D Modality Independent Elastography Robustness to Boundary Condition Noise', Medical Imaging 2007: Physiology, Function and Structure from Medical Images, San Diego, CA.

R. E. Ong, J. J. Ou, and M. I. Miga, 'Using Laplace's Equation for Non-rigid Registration of Breast Surfaces', Medical Imaging 2007: Visualization and Image-Guided Procedures, San Diego, CA.

Peer-reviewed publications

J. J. Ou, R. E. Ong, T. E. Yankeelov, and M. I. Miga, 'Evaluation of 3D modality-independent elastography for breast imaging: a simulation study', Physics in Medicine and Biology, Vol. 53, No. 1, pp. 147-163, 2008.

Conclusions

The current results and progress denoted in this report are within the proposed statement of work and are encouraging towards completion of the overall objectives with further effort. No significant deviations are reported at this time, although in certain regards as noted within the text, our efforts are being refocused towards relevant practical issues of the project that have become more prominent as the work has progressed. Notable accomplishments at this time include the implementation of a fully 3D MIE application, further analysis of factors influencing elastographic reconstruction fidelity, and engineering of devices suitable for MIE data acquisition in both phantom and human studies. Future work will be directed towards following up in all of these areas, as well as newer studies into *ex vivo* tissue characterization and collaborative clinical efforts generated from interest regarding our project.

References

- [1] Garra BS, Cespedes EI, Ophir J, Spratt SR, Zuurbier RA, Magnant CM, and Pennanen MF. Elastography of breast lesions: Initial clinical results. *Radiology*, vol. (202): pp. 79–86, 1997.
- [2] McKnight AL, Kugel JL, Rossman PJ, Manduca A, Hartmann LC, and Ehman RL. MR Elastography of Breast Cancer: Preliminary Results. *Am J Roentgenol*. vol. (178): pp. 1411-1417, 2002.
- [3] Balay S, Buschelman K, Eijkhout V, Gropp WD, Kaushik D, Knepley MG, McInnes LC, Smith BF, Zhang H. “PETSc Users Manual”, ANL-95/11 Revision 2.1.5. Argonne National Laboratory, 2004.
- [4] Balay S, Gropp WD, McInnes LC, Smith BF. “Efficient Management of Parallelism in Object Oriented Numerical Software Libraries”, Modern Software Tools in Scientific Computing. Birkhauser Press, pp. 163-202, 1997.
- [5] Dooley MM, Weaver JB, Van Houten EEW, Kennedy FE, Paulsen KD. “Thresholds for detecting and characterizing focal lesions using steady-state MR elastography,” *Medical Physics*, vol. 30(4): pp. 495-504, 2003.
- [6] Otsu N. “A threshold selection method from gray-level histograms,” *IEEE Trans Syst Man Cybern*, vol. 9: pp. 62-66, 1979.
- [7] Chu KC and Rutt BK. Polyvinyl alcohol cryogel: an ideal phantom material for MR studies of arterial flow and elasticity. *Magn Reson Med*. vol. 37(2): pp. 314-319, 1997.
- [8] Brusseau E, Fromageau J, Finet G, Delachartre P, Vray D. “Axial strain imaging of intravascular data: results on polyvinyl alcohol cryogel phantoms and carotid artery,” *Ultrasound Med Biol*, vol. 27(12): pp. 1631-1642, 2001.

Appendix

The following is a listing of original works referred to in the Body of the Report. Full reprints and other relevant supplemental material are provided after this description.

		Page
A.	J. J. Ou, R. E. Ong, T. E. Yankeelov, and M. I. Miga, 'Evaluation of 3D modality-independent elastography for breast imaging: a simulation study', Physics in Medicine and Biology, Vol. 53, No. 1, pp. 147-163, 2008.	9
B.	M. I. Miga, J. J. Ou, and D. L. Ellis, 'An elastography framework for use in dermoscopy', Medical Imaging 2007: Physiology, Function and Structure from Medical Images, San Diego, CA.	26
	(Condensed slides of presentation)	37
C.	J. J. Ou, R. E. Ong, and M. I. Miga, 'An Evaluation of 3D Modality Independent Elastography Robustness to Boundary Condition Noise', Medical Imaging 2007: Physiology, Function and Structure from Medical Images, San Diego, CA.	41
	(Condensed slides of presentation)	50
D.	R. E. Ong, J. J. Ou, and M. I. Miga, 'Using Laplace's Equation for Non-rigid Registration of Breast Surfaces', Medical Imaging 2007: Visualization and Image-Guided Procedures, San Diego, CA.	51
	(Condensed slides of presentation)	62

Evaluation of 3D modality-independent elastography for breast imaging: a simulation study

J J Ou¹, R E Ong¹, T E Yankeelov^{1,2,3,4} and M I Miga^{1,2,3}

¹ Department of Biomedical Engineering, Vanderbilt University, Nashville, TN 37235, USA

² Department of Radiology and Radiological Sciences, Vanderbilt University Medical Center, Nashville, TN 37232, USA

³ Vanderbilt University Institute of Imaging Science, Nashville, TN 37232, USA

⁴ Department of Physics and Astronomy, Vanderbilt University, Nashville, TN 37235, USA

E-mail: jao.ou@vanderbilt.edu and michael.i.miga@vanderbilt.edu

Received 26 April 2007, in final form 1 November 2007

Published 19 December 2007

Online at stacks.iop.org/PMB/53/147

Abstract

This paper reports on the development and preliminary testing of a three-dimensional implementation of an inverse problem technique for extracting soft-tissue elasticity information via non-rigid model-based image registration. The modality-independent elastography (MIE) algorithm adjusts the elastic properties of a biomechanical model to achieve maximal similarity between images acquired under different states of static loading. A series of simulation experiments with clinical image sets of human breasts were performed to test the ability of the method to identify and characterize a radiographically occult stiff lesion. Because boundary conditions are a critical input to the algorithm, a comparison of three methods for semi-automated surface point correspondence was conducted in the context of systematic and randomized noise processes. The results illustrate that 3D MIE was able to successfully reconstruct elasticity images using data obtained from both magnetic resonance and x-ray computed tomography systems. The lesion was localized correctly in all cases and its relative elasticity found to be reasonably close to the true values (3.5% with the use of spatial priors and 11.6% without). In addition, the inaccuracies of surface registration performed with thin-plate spline interpolation did not exceed empiric thresholds of unacceptable boundary condition error.

1. Introduction

Breast cancer is the most common cancer of women in the United States, the second most common cause of cancer death in women and the leading cause of death in women aged 45 to 55. Estimates for the year 2007 indicate that 178 480 American women will be diagnosed with the disease and 40 910 women will die from it (ACS 2007). While many advances have been made in the treatment of the disease, the ability to detect its presence for either screening

or diagnostic purposes remains an area of active research involving many novel forms of imaging. The characterization of the mechanical properties of breast tissue is an important potential source of clinical information because of the long-standing association of palpable differences in stiffness with possible pathological states. A minimally invasive methodology for analyzing tissue elasticity through imaging and/or image processing techniques is a central goal of the field of elastography (Parker *et al* 2005), with the application of various techniques being found not only in the interrogation of the breast (McKnight *et al* 2002, Melodelima *et al* 2006, Sinkus *et al* 2000), but also in skin (Miga *et al* 2005, Tsap *et al* 1998, Zhang *et al* 2004), prostate (Curiel *et al* 2005, Egorov *et al* 2006) and other accessible organ systems.

Many of the current elastography methods are founded in ultrasound (US) (Ophir *et al* 1991, 2000) and magnetic resonance (MR) (Manduca *et al* 2001, Muthupillai *et al* 1995) imaging and involve the estimation of induced displacements within the tissue of interest to infer the elasticity distribution. We have recast the problem as a physically constrained, non-rigid image registration utilizing numerical models of static deformation with image similarity metrics to reconstruct the spatial distribution of elasticity parameters. This technique has been termed ‘modality-independent elastography’ (MIE) (Miga 2002, 2003, Washington and Miga 2004) because of its ability to handle anatomical images from different sources with relatively simple modifications to the acquisition procedure. To date, data from MR, x-ray computed tomography (CT) and digital photography have been used to successfully drive the algorithm in two-dimensional (2D) work. Others have also pursued similar approaches within the context of ultrasound elastography (Garra *et al* 1997, Gokhale *et al* 2004, Sarvazyan *et al* 1995), optical image analysis (Tsap *et al* 1998) and to a lesser extent with magnetic resonance elastography (Fowlkes *et al* 1995). While the use of MIE in 2D has been illuminating for algorithmic development and may have its own applications in studying the more planar system of the skin, ultimately, translation of the method to utilize volumetric data is desirable (if not necessary) in order to provide an accurate representation of organs such as the breast as a whole. In this work, we present a newly realized three-dimensional (3D) version of MIE along with simulation experiments to evaluate its performance. In addition, some potential effects of degraded input quality are addressed by examining robustness of the algorithm to inaccuracies under specified boundary conditions and then comparing the reconstruction fidelity of three different techniques developed for semi-automatic generation of boundary conditions.

2. Methods and materials

2.1. MIE reconstruction framework

The conceptual framework for our elastographic reconstruction has been previously described in Miga (2002, 2003), Miga *et al* (2005) and Washington and Miga (2004)). To review, an image of a tissue of interest (*source*) is deformed by a biomechanical model and compared against an acquired image of the same tissue in a mechanically loaded state (*target*). Iterative updates of elasticity parameters to the model are performed until a suitable match in image similarity is achieved in a least-squares manner to satisfy a nonlinear optimization scheme. This process as illustrated in figure 1 can be classified as an inverse problem, with model-based deformation and registration of the source image representing the forward problem.

The three major components of the reconstruction algorithm are the biomechanical model, image comparison and the optimization routine. Although there are a number of models for soft-tissue mechanics, it is reasonably appropriate to begin with a general elastic body. The partial differential equation (PDEs) that expresses a state of mechanical equilibrium is

$$\nabla \cdot \sigma = 0 \quad (1)$$

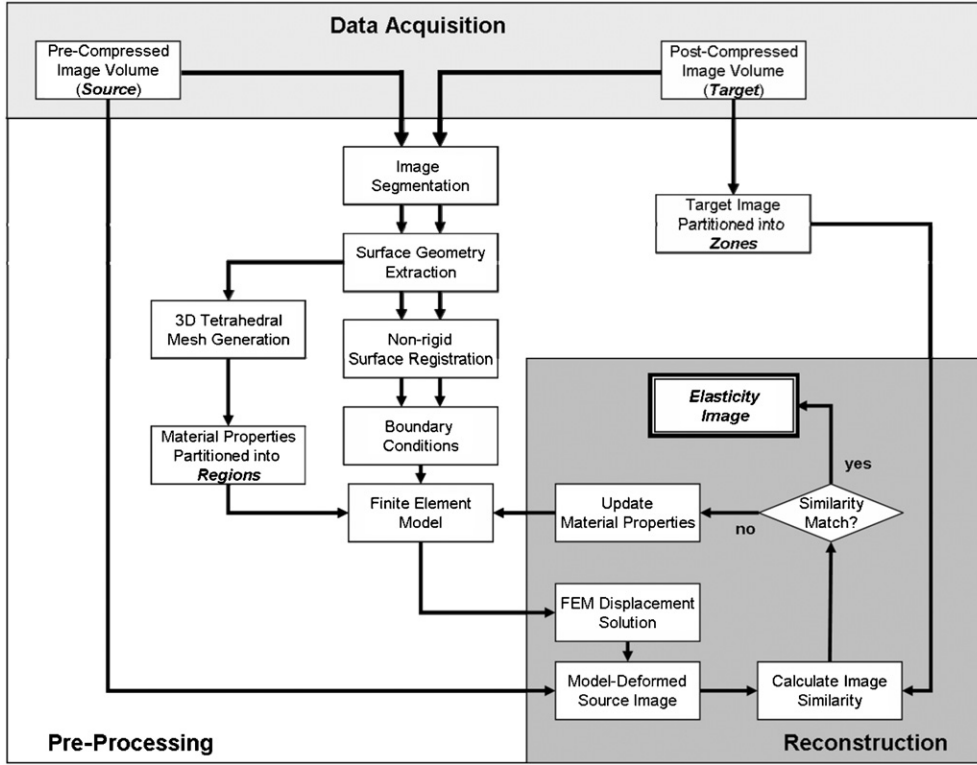


Figure 1. Schematic of MIE framework. After acquisition of image data, surface representations are segmented from the pre- and post-deformation volumes (*source* and *target*, respectively). A number of pre-processing steps are performed to generate boundary conditions for the biomechanical model, which produces a deformed image that can be compared with the true target volume. The optimization routine updates the elasticity distribution until the best similarity is achieved.

where σ is the Cartesian stress tensor (Boresi and Chong 1999). We have elected to describe the constitutive tissue behavior using Hooke's law of linear elasticity, which states that the strain is proportional to the applied stress, and further assume that materials are isotropic and nearly incompressible in nature. The description of the constitutive relationship between stress and strain is ultimately expressed in terms of the elasticity parameters E (Young's modulus) and ν (Poisson's ratio).

A finite element representation of the model is constructed from the source image. Elements of the mesh are grouped using a K-means algorithm by initializing a number (N) of seed points that are the centers of the clusters and iteratively minimizing their summed distance to all element centroids in the mesh. This process defines a set of nearly equally sized but spatially non-uniform *regions* that are homogeneous with respect to their material properties and establish the 'resolution' of the reconstructed elasticity image. After assigning appropriate boundary conditions based on estimated displacement or stress, the standard Galerkin method of weighted residuals (Lapidus and Pinder 1982) is used to construct a matrix system. The solution of that system yields displacements that are used to deform the source image. A second discretization is performed by binning the target image into M groups of contiguous voxels termed *zones*. The model-deformed image is then compared to the target by summing

the similarity metric evaluated for all zones. The correlation coefficient (Fitzpatrick *et al* 2000) is used throughout this work as it has empirically demonstrated better performance for our method over other intensity-based metrics such as the sum of squared differences and normalized mutual information. Optimization of the elasticity parameters is taken as the minimization of the objective function:

$$\Psi = |S_{\text{TRUE}} - S_{\text{EST}}|^2 \quad (2)$$

where S_{TRUE} is the set of similarity values achieved when comparing the target image to itself, S_{EST} is the similarity between the target and model-deformed source images using current estimates of the elastic modulus distribution and $|\bullet|$ denotes the vector L^2 -norm. Note that by definition, S_{TRUE} for the correlation coefficient has a constant value of 1. Differentiating (2) with respect to the elasticity distribution and setting the resulting expression equal to zero generates a series of nonlinear equations that can be solved using the Levenberg–Marquardt method:

$$\begin{aligned} [\mathbf{J}^T \mathbf{J} + \alpha I] \{\Delta E\} &= [\mathbf{J}^T] \{S_{\text{TRUE}} - S_{\text{EST}}\} \\ \alpha^2 &= \lambda \left[\frac{1}{N} \sum_{i=1}^N (\mathbf{J}^T \mathbf{J})_{ii} \right] \Psi^2 \end{aligned} \quad (3)$$

where \mathbf{J} is the Jacobian matrix of size $M \times N$ and ΔE is the vector of updates to the material property distribution defined by the regions. The regularization parameter α uses an empirical scalar factor λ as determined by the methods described in Joachimowicz *et al* (1991). Each column of the Jacobian matrix is a finite difference approximation of the change in image similarity over all zones due to the perturbation of a single material property region, such that

$$J \equiv \frac{\partial S_{\text{EST}}}{\partial E} = \begin{bmatrix} \frac{\partial S_1}{\partial E_1} & \frac{\partial S_1}{\partial E_2} & \cdots & \frac{\partial S_1}{\partial E_N} \\ \frac{\partial S_2}{\partial E_1} & \ddots & & \vdots \\ \vdots & & \ddots & \vdots \\ \frac{\partial S_M}{\partial E_1} & \cdots & \cdots & \frac{\partial S_M}{\partial E_N} \end{bmatrix}. \quad (4)$$

Modulus values contained in E are updated by ΔE until an error tolerance on the relative objective function error evaluation is reached or a maximum number of iterations are completed. Spatial averaging of elasticity values in the model and solution relaxation between iterations are also utilized to improve the stability of the optimization.

2.2. Parallel computing framework

The transition of this method from 2D to 3D entails a much higher computational overhead that affects all parts of the reconstruction. The mesh needed to describe the entire breast as opposed to a single slice is at least 20–40 times greater in the number of structural components (nodes and elements), and the model must account for an additional degree of freedom. The resulting system of equations to be solved is thus nearly two orders of magnitude larger. The finite difference approximation of each column of the Jacobian matrix requires a ‘forward solve’ consisting the biomechanical model, image deformation and evaluation of the similarity metric. Because this must be done for every elasticity region, attempting to adequately sample the spatial domain makes the building of this matrix the primary expenditure of computing resources.

In order to achieve a reasonable level of performance, the Message Passing Interface standard for parallel processing is used to distribute formation of the Jacobian among a number of communicating nodes controlled within a static single process, multiple data (SPMD) scheme. The Portable Extensible Toolkit for Scientific Computation (PETSc) (Balay *et al* 2004, 1997) has provided the necessary coding base for interfacing sparse matrix system solvers with our C/C++ Gauss–Newton optimization routine. This design scales readily to the number of processors available; it has been tested on a homogeneous cluster of 18 processors (2.0 GHz Pentium4 Xeon, 1 GB RAM) located in the laboratory, as well as a heterogeneous cluster of hundreds of processors available through the Vanderbilt Advanced Computing Center for Research and Education project. The use of many processors is capable of producing a nearly linear speedup and otherwise agrees in principle with the performance impact suggested by Ahmdahl’s law (Ahmdahl 1967).

2.3. Simulation experiment setup

For this work, a simulation experiment is defined by the creation of an idealized target image volume from a deformation achieved by the specification of boundary conditions at the surface of the breast. This ensures data fidelity in order to effectively evaluate reconstruction performance in the optimization and model characteristics. Two image volumes of human breast were made available to further test the modality independence of the algorithm. The first was obtained from a dedicated breast CT scanner ($256 \times 256 \times 130$, voxel size 0.6 mm^3) as described in Boone *et al* (2006), (2001) and Boone and Lindfors (2006) and the second from a Philips Achieva 3.0 T MR unit ($256 \times 256 \times 98$, voxel size 1.0 mm^3) using a clinically approved transmit–receive double-breast coil to acquire a 3D T1-weighted exam with a fat-nulling inversion pulse ($\text{TR/TE/a/NEX} = 4.6 \text{ ms}/2.3 \text{ ms}/10^\circ/1$) (Yankeelov *et al* 2007). The surfaces of the breast were segmented (ANALYZE 6.0, Mayo Clinic, Rochester, MN) to create tetrahedral meshes composed of 39 013 nodes connected in 214 163 elements for the CT volume and 20 623 nodes and 111 142 elements for the MR volume. A 2 cm spherical tumor was synthetically implanted in the center of each mesh by assigning a stiff modulus to appropriate member elements that was six times higher than the surrounding material (Krouskop *et al* 1998, Samani *et al* 2007). Tissue deformation was performed by creating a set of displacements calculated to approximate a Gaussian stress distribution applied to a rectangular area on the lateral surface of the breast. The displacements were then applied to the original volumes in order to create the desired target images. Figure 2 illustrates the setup of the simulation data.

2.4. Reconstruction experiments

Reconstructions using spatial *a priori* knowledge of the location and size of the inclusion were first performed in order to constrain the problem, as well as the computational expense of the Jacobian matrix, to a two-material discrimination of relative stiffness (elastic contrast). A second set of experiments was then used to address the viability of the method to perform a generalized detection of the lesion with no knowledge of the actual structure of the domain. To run these naive reconstructions for the CT data set, 3180 material regions and 733 voxel similarity zones were partitioned, while in the MR data set, 3166 regions and 768 zones were used. In all cases, the reconstruction was initialized with a homogeneous elasticity distribution, and the value of Poisson’s ratio held constant at $\nu = 0.485$ to represent a nearly incompressible material.

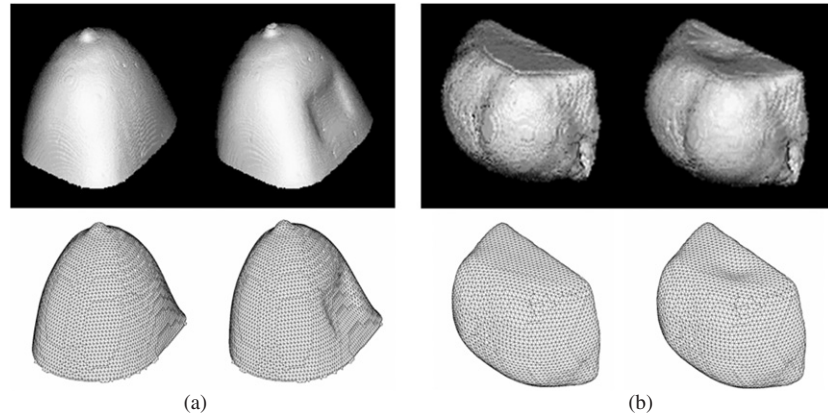


Figure 2. (a) CT data set and (b) MR data set used for 3D MIE simulations. Surface renderings of the image volumes (top row) and meshes (bottom row) are shown for the pre- (*source*) and post-deformation (*target*) scenarios.

2.5. Evaluating boundary condition influence

In addition to image acquisition, the other major input to the reconstruction algorithm is the delineation of boundary conditions on the region of interest over which the model is applied. While relatively easy to control in simulation, in a real clinical situation, this presents the challenge of accurately determining point correspondences between the source and target breast surfaces. The effect of any inaccuracies is cumulative, as errors are propagated from the model to the image deformation and finally the similarity measurements. In previous 2D work, manual delineation of boundary conditions was possible with guidance and correction using standard computer input devices (i.e. a mouse). However, the increased complexity of mesh geometry in 3D necessitates a more automated technique of determining correspondence between two surfaces. Potentially non-trivial random and/or operator-dependent noise is introduced into any generated boundary conditions. Therefore, the following experiments were performed to examine the ability of the algorithm to tolerate various types of mis-mappings.

2.5.1. Robustness to randomized boundary errors. The gold standard boundary conditions used to create the simulated target image volumes were deliberately disrupted to examine the effect of random noise on reconstruction fidelity. A series of magnitudes ranging from 0.01 to 2.0 voxel units (mesh coordinates normalized by their respective spacing in image space) were applied to the CT and MR data sets. Therefore, every boundary position is displaced by the same amount but in a completely unpredicted manner, as illustrated in figure 3. These altered boundary conditions sets were utilized in the reconstruction of the *a priori* two-material test case, and the tolerance of the method was evaluated by calculating the average reconstructed elasticity contrast ratios over four trials of each level of noise, with deviations less than 20% from the true stiffness being deemed acceptable.

2.5.2. Feasibility of automated boundary condition generating methods. Three methods of surface registration and point correspondence were considered as the basis of a semi-automated method for determining boundary conditions input to the reconstruction algorithm. Two were

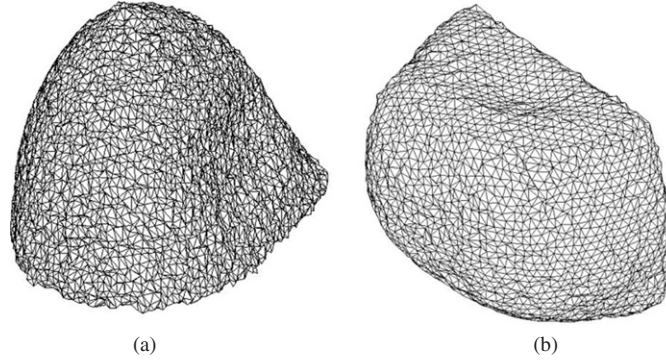


Figure 3. Examples of distortion due to additive randomized error. For effect, noise of 2.0 voxel units is shown as applied to the gold standard boundary condition set for CT (a) and MR (b). At these extreme levels, the smooth surface of the breast as originally captured in figure 2 is completely lost, and the forced reconfiguration of internal elements in the finite element mesh adversely affects all aspects of the reconstruction.

specifically developed for this work by attempting to use potential energy distributions derived from classic PDEs for surface matching, and the other is a free-form geometrical warping.

If the flow of a hypothetical substance over both the source and target breast surfaces is taken to be a conserved process and modeled using potential theory, correspondence can be assigned by matching areas of similar energy deposition, that is, the equivalent level sets. The algorithm for the PDE-based surface matching methods can be summarized in the following steps:

- (1) *Determine an energy distribution for each surface.* Laplace's equation is commonly used to describe the steady-state distribution of potential energy Φ in a system:

$$-\nabla^2 \Phi = 0. \quad (5)$$

Similarly, the diffusion equation describes the temporal change in potential over a region:

$$\frac{\partial \Phi}{\partial t} = D \nabla^2 \Phi \quad (6)$$

where D is the diffusion coefficient. Each PDE is solved over both breast surfaces (source and target). For both equation (5) and (6), the nipple is assigned as an area of high potential energy. Additionally, with equation (5), nodes at the chest wall are assigned a value of 0 in order to obtain a non-trivial solution, whereas the propagating front produced by (6) is artificially halted at the chest wall boundary. While both PDE solutions similarly establish an energy gradient over the breast surfaces, their application in the following steps results in more apparent differences.

- (2) *Determine correspondence between energy distributions.* From the solution of the PDEs on the source surface, a series of spatially distributed isocontours representing distinct potentials are determined. For each level set, an isocontour of equivalent potential energy is found on the target surface and the two curves matched according to the symmetric closest point method described by Papademetris *et al* (2002).
- (3) *Generate boundary conditions.* By extracting a number of isocontours of different values, the resulting point correspondence vectors define a relatively dense 3D displacement field. The displacement for each boundary node can then be interpolated from the set of its nearest neighbors.

The final method employs thin-plate splines (Goshtasby 1988) to generate a set of boundary conditions. In this well-established method of non-rigid transformation, a number of control points with known correspondences establish constraints on the deflection of a hypothetical thin sheet of material in order to best warp the two surfaces together. Displacements at each boundary node are then simply interpolated from the calculated fit. For these simulation experiments, a subset of boundary nodes was used to represent physical markers on the breast surface. Forty points were uniformly distributed over the CT mesh and eighty for the MR mesh in order to handle the more highly variegated shape of the latter data set.

The automated methods were initially evaluated according to their target registration error (TRE), which was calculated as the average Euclidean distance between the generated and true boundary conditions. Because the deployment of these fits represents a more correlated form of noise, these boundary conditions were also applied to the two-material (*a priori*) scenario and the reconstructed elasticity contrast values compared to the trials of additive randomized error for which the magnitude was approximately equal to the TRE. Finally, a mapping of the objective function space was performed by calculating the similarity values for model-based image deformations over a range of elasticity contrasts from 0.5:1 to 30:1. An interpolating curve was fit to extract the minimum objective function value and associated contrast ratio to determine a theoretical optimal reconstruction as constrained by the estimated boundary conditions.

3. Results

3.1. MIE reconstructions

Because the use of *a priori* spatial information about the inclusion limits the reconstruction to a two-material system, the fidelity of the reconstruction is simply evaluated by examining the elastic contrast between the inclusion and the normal tissue of the breast (ideal of 6:1). Figure 4 demonstrates the behavior of the algorithm in optimizing the objective function while successfully characterizing the stiffness of the inclusion to within 5% of the actual value (6.02:1 and 6.21:1 for the CT and MR data sets, respectively).

The fidelity of the generalized reconstruction experiments (using no *a priori* knowledge of the domain) was primarily evaluated on its ability to detect the presence of an inclusion based on classification of the material property distribution as well as the retrospective accuracy of localizing the lesion. The final elasticity values were treated as a Gaussian mixture of two classes and separated by a threshold established via the method described in Otsu (1979). The likelihood of discriminating a lesion in the resulting elasticity image was found using the contrast-to-noise ratio (CNR) as defined by Bilgen (1999) and Doyley *et al* (2003):

$$\text{CNR} = \sqrt{\frac{2(\mu_L - \mu_B)^2}{\sigma_L^2 + \sigma_B^2}} \quad (7)$$

where μ and σ^2 are the sample mean and variance of a material property distribution and the subscripts L and B denote the lesion and normal material types, respectively. As a quantitative assessment of the localization of the lesion, the positive predictive value of correctly identifying a lesion material within the known segmented region of the inclusions was also calculated as a ‘quality of reconstruction score’ (QRS). This value is significant because identification of the lesion border and material classification are done independently, so user knowledge of the test scenario does not influence the performance of the measure. The ‘true positive’ (TP) elements of the mesh are counted as the number correctly identified as tumor and lying within the

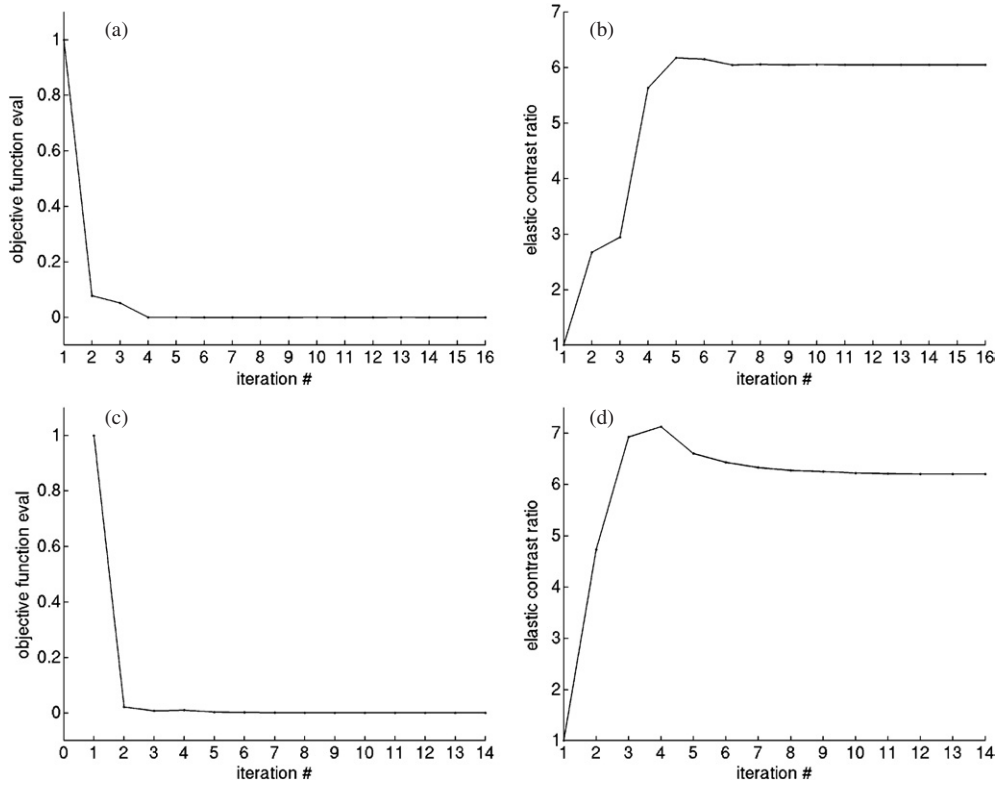


Figure 4. Optimization behavior of reconstructions using *a priori* knowledge of the inclusion location. For the CT simulation, the objective function evaluation (normalized to the initial dissimilarity value of a homogeneous elasticity distribution) and elastic contrast over several iterations of the algorithm are shown in panels (a) and (b), respectively. Similarly, this behavior for the MR data set is displayed in (c) and (d). In each case, the minimum value is achieved quickly and stably, with the corresponding contrast ratio matching the true value of 6:1 very closely (6.02:1 and 6.21:1 for CT and MR, respectively).

Table 1. Evaluation of reconstruction fidelity for lesion detection.

	CNR	QRS (%)	Max CR (\times :1)	Optimal CR (\times :1)
CT	3.55	99.4	2.66	3.01
MR	3.93	99.7	2.02	2.26

Max CR: maximum elasticity contrast between lesion and normal tissue in naive reconstruction.
Optimal CR: optimal elasticity contrast after accounting for overlap in elasticity region partitioning.

known segmentation of the lesion, while the ‘false positive’ (FP) elements are those identified as tumor but in an incorrect location. Thus, the calculation of QRS is simply $TP/(TP + FP)$. Cutoffs for successful detection and localization were set at $CNR \geq 2.2$ as noted by Doyley *et al* (2003) and $QRS \geq 80\%$ as empirically determined by a prior study in 2D MIE work (Ou *et al* 2006a, 2006b), and both the CT and MR reconstructions successfully identified the embedded lesions according to these criteria (see table 1).

The peak modulus contrast value of a reconstruction was calculated by taking the ratio of the average elasticity for manually selected homogeneous regions of the approximately equal area known to be representative of the two materials. As reported in table 1 and visualized

Table 2. Effect of applied random boundary condition noise on objective function space and reconstructed elasticity contrast ratio. The respective ranges where a cutoff in reconstruction tolerance was observed are listed for each simulation set.

CT		MR	
Randomized vector magnitude (voxel units)	Mean optimal elasticity contrast value ($\times 1$)	Randomized vector magnitude (voxel units)	Mean optimal elasticity contrast value ($\times 1$)
0.1	5.62 ± 0.421	0.01	6.33 ± 0.096
0.2	5.70 ± 0.588	0.02	6.75 ± 0.058
0.3	5.97 ± 0.846	0.03	6.93 ± 0.634
0.5	2.36 ± 0.393	0.05	7.60 ± 0.821
1.0	2.47 ± 0.266	0.1	9.35 ± 1.27
2.0	2.17 ± 0.422	0.2	11.3 ± 0.866

Table 3. Reconstruction performance as affected by semi-automated boundary condition generation methods. The mean error of surface registration is related to the accuracy of characterizing the lesion stiffness.

Method	CT		MR	
	TRE (mm)	Elasticity contrast ($\times 1$)	TRE (mm)	Elasticity contrast ($\times 1$)
Diffusion	1.5	17.5	0.61	348
Laplace	0.52	5.02	0.48	673
Thin-plate spline	0.26	5.66	0.023	6.26

in figures 5 and 6, the characterization of the relative stiffness is less than the true elasticity contrast by nearly a factor of 3 in both cases. This reveals a difficulty with large inverse problems in 3D where a need for reasonable performance can lead to a tradeoff in accuracy. By choosing approximately 3200 regions to cover the domain of the breasts for the naive reconstructions, the number of degrees of freedom presented to the optimization scheme is quite high. However, this is also relatively coarse in the sense of visualizing the reconstruction, as it roughly corresponds to a $15 \times 15 \times 15$ image volume. Because the elasticity regions do not conform perfectly to the actual lesion borders and furthermore comprise both the tumor and healthy tissue, it seemed reasonable to surmise that in this mis-estimation of spatial extents the algorithm was forced to attempt a best-fit compromise. To test this hypothesis, we agglomerated all regions in the original partitioning that overlapped the tumor and then ran the reconstruction again as a two-material characterization. Upon inspection, this re-grouping was clearly a larger entity than the tumor itself (closer to 3 cm in diameter) and resulted in a shift of the global optimum to a lower elasticity contrast. In effect, the model reacted to this new, oversized tumor by reducing its stiffness in order to achieve the proper image similarity match. When viewed in light of this analysis as summarized in table 1, the elasticity contrast found by the naive reconstruction is then actually quite accurate.

3.2. Evaluating boundary condition influence

3.2.1. Robustness to randomized noise. Table 2 demonstrates that as the magnitude of the applied randomized noise vectors was increased, changes in the reconstructed elasticity contrast reflected a decreased ability to achieve a successful result (recall that the correct ratio

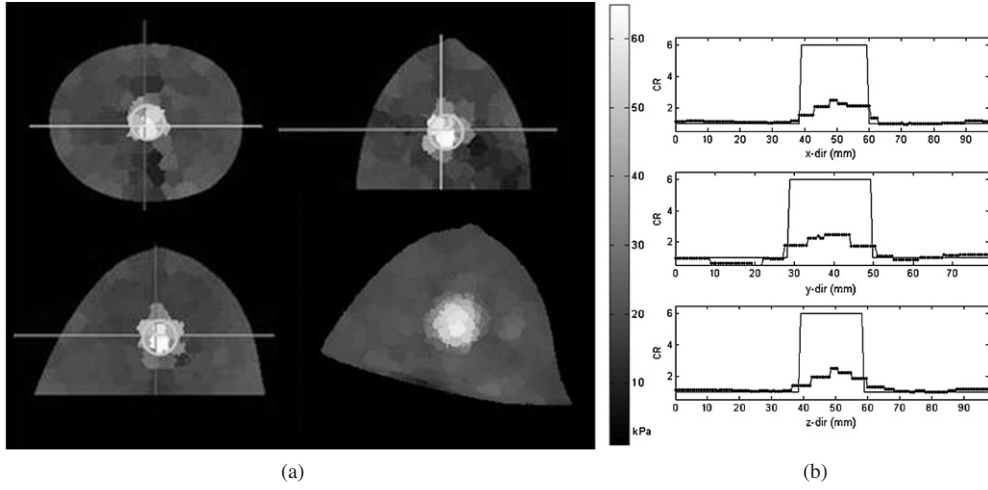


Figure 5. Reconstruction used for lesion detection in the CT data set. (a) Orthogonal views taken through the center of the elasticity image volume are shown along with a projection surface rendering (lower right). The simulated inclusion implanted in the mesh is visually distinguished from the surrounding tissue. The color bar indicates the range of elasticity values ($\sim 7\text{--}42$ kPa) designated by the reconstruction, with higher (stiffer) values shown in the white end of the grayscale mapping. (b) Transect plots through the center of the volume along the cardinal directions show the profile of elasticity contrast (dotted lines) overlaid by the true profile of the simulation (solid lines).

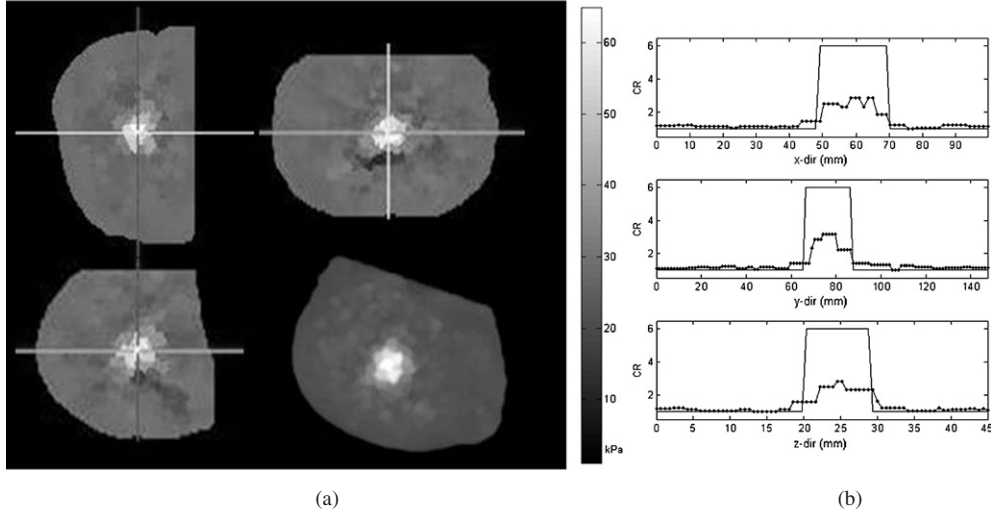


Figure 6. Reconstruction used for lesion detection in the MR data set. (a) Orthogonal views taken through the center of the elasticity image volume are shown along with a projection surface rendering (lower right). Once again, the inclusion appears to have a recognizably different elasticity, with values on the color bar ranging from $\sim 10\text{--}57$ kPa. (b) Transect plots through the center of the volume along the cardinal directions show the profile of elasticity contrast (dotted lines) overlaid by the true profile of the simulation (solid lines).

is 6:1). For the CT simulation, on average, errors of 0.5 voxel units or greater showed a dramatically reduced ability to accurately characterize the stiffness of the lesion. Similarly, though at a much smaller scale, the MR simulation began to have noticeable difficulty in

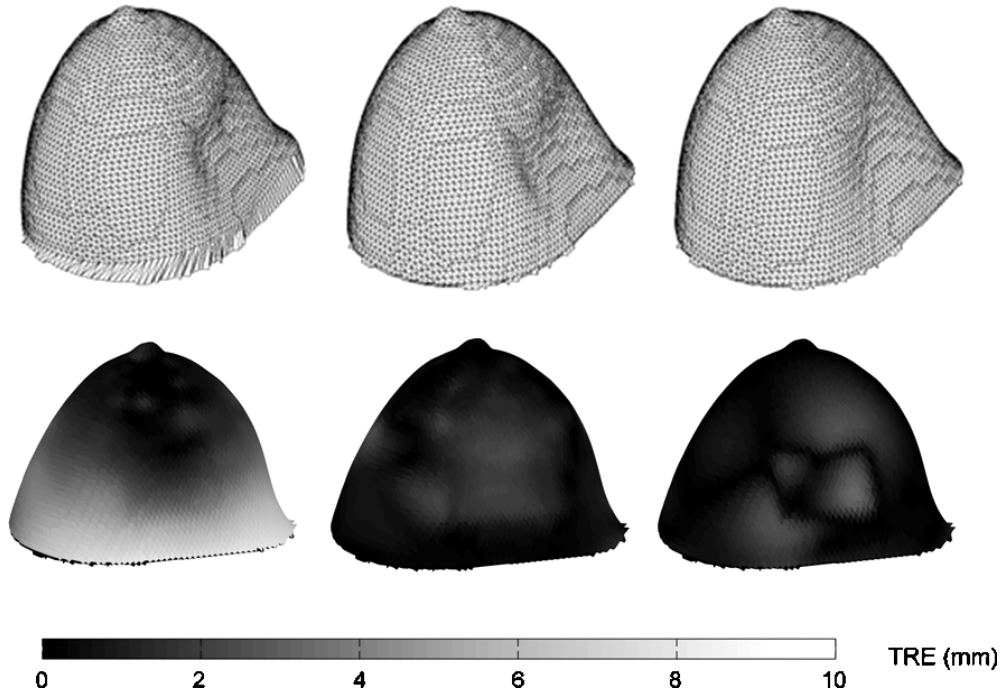


Figure 7. Three candidate automated methods for MIE boundary condition generation applied to simulation CT data. Top row, from left to right: surface deformations calculated from diffusion energy matching, Laplace solution energy and thin-plate spline interpolation. Bottom row: target registration error (TRE) distribution for each method when compared against the gold standard of known correspondence. The diffusion-based mesh is both qualitatively and quantitatively the worst performer. The Laplace solution appears to capture the shape of the bladder indentation more precisely, but the thin-plate spline has the best overall accuracy in determining point correspondence.

achieving a reasonable reconstruction at noise levels of 0.05 voxel units. These values were taken as suitably conservative measures for evaluating the efficacy of boundary conditions generated by the semi-automated methods.

3.2.2. Reconstruction effects of generated boundary conditions. The accuracy of each automated boundary condition technique described in section 2.5.2 was assessed by the TRE with respect to the gold standard boundary condition set and its ability to characterize the elastic contrast in the two-material reconstruction test case. Figure 7 depicts the deformation fields as applied to the CT data. Qualitatively, the displacements found by the diffusion method are quite different from the true set, while the results from the solution of Laplace's equation and the thin-plate spline interpolation appear to be more satisfactory. As shown in table 3, the mean TRE of the three methods confirms that the spline-based method has the best performance (0.26 mm), the Laplace method next (0.52 mm) and the diffusion method being the worst (1.5 mm). Inspection of figures 8 and 9 further demonstrates that the imposition of an inexact boundary condition set on the model has a distinct effect on the optimization by shifting the objective function minimum value to a different optimal elastic contrast ratio. Additionally, the convexity of the objective function is lost in the cases with a higher TRE. The differences in the generated boundary condition sets for the MR simulation are not easily visualized but follow a similar performance trend (TRE of spline 0.023 mm, Laplace method

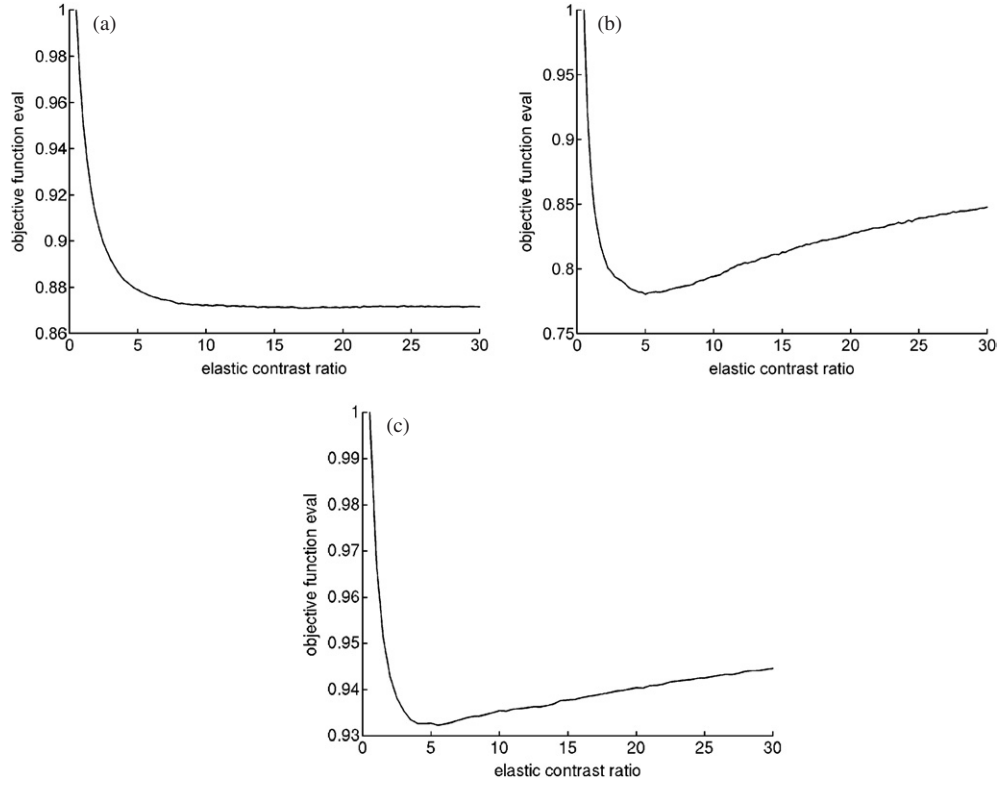


Figure 8. Mappings of objective function value versus elasticity contrast ratio (tumor:breast) affected by the boundary condition sets generated from the different automated methods of surface point correspondence as applied to the CT data set. The minimum value of each curve corresponds to the altered optimal elasticity contrast when constrained by the inaccuracies of the methods: (a) diffusion, (b) Laplace and (c) thin-plate spline interpolations. The ordinate is normalized to the initial value of each case. The global minimum of (a) is out of range of the plot.

0.48 mm, diffusion 0.61 mm). For both simulations, there exists a direct relationship between a low TRE and increased reconstruction fidelity in characterization of the elasticity contrast of the lesion.

4. Discussion

As other researchers have noted, the incorporation of *a priori* information can greatly enhance the performance of their elastography methods (Doyley *et al* 2005, 2006). We recognize that the judicious use of information regarding lesion morphology as obtained from conjunctive imaging studies and post-processing would potentially aid MIE as well, especially in reducing the number of search parameters and improving initialization of the algorithm. The reconstructions using *a priori* spatial knowledge of the inclusion were initially intended to simply illustrate that the objective function space formed by using an image similarity metric was smooth and readily traversed by the algorithm in a manner expected for a Gauss–Newton optimization. However, they also provide a stark contrast to the naive lesion detection test cases, which were performed to evaluate the inverse problem framework and demonstrate its ability to analyze the full 3D domain of the breast. The results of the generalized reconstructions are very encouraging in having successfully identified

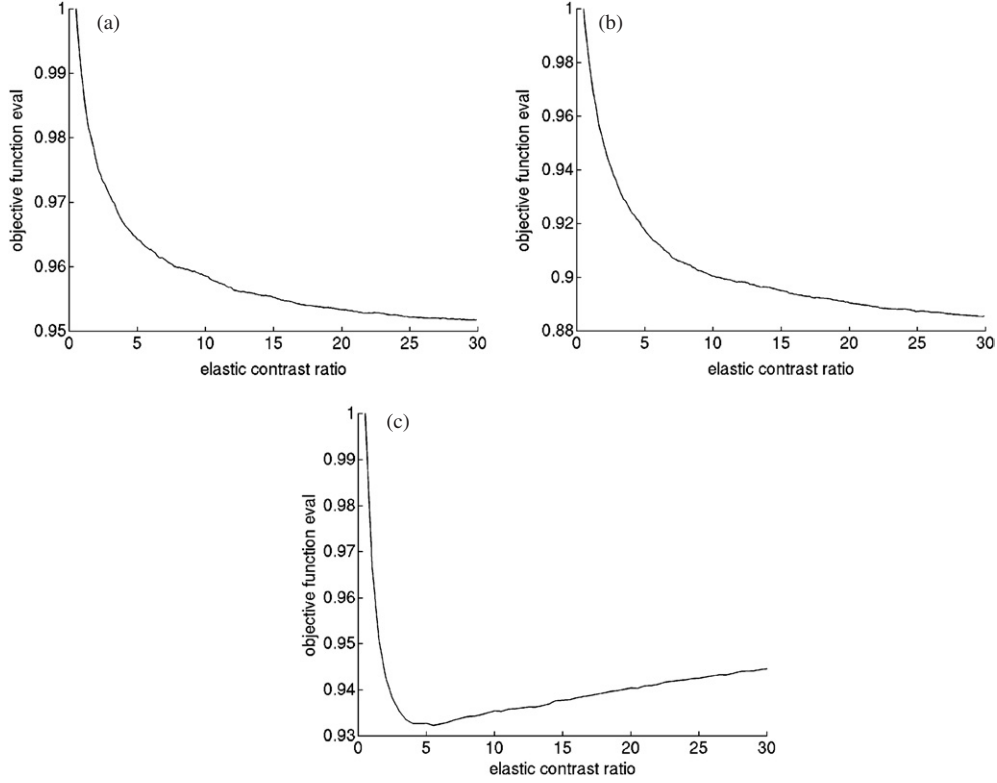


Figure 9. Mappings of objective function value versus elasticity contrast ratio (tumor:breast) affected by the boundary condition sets generated from the different automated methods of surface point correspondence as applied to the MR data set. The minimum value of each curve corresponds to the altered optimal elasticity contrast when constrained by the inaccuracies of the methods: (a) diffusion, (b) Laplace and (c) thin-plate spline interpolations. Again, the ordinate is normalized to the initial value and should not be interpreted as an equivalent scale for each case. The global minima of (a) and (b) are out of range of the plot.

and localized the inclusions. Although the discretizations of the meshes did not achieve particularly accurate material characterizations, the optimal elasticity contrast as dictated by the available objective function was matched in each case to within 12%. The observation that mis-estimation of the lesion extent altered the underlying test scenarios suggests that investigating methods of dynamically adjusting region assignment could facilitate shape resolution and concomitantly better elasticity contrast ratio values.

In translating MIE and its associated technologies to a clinical setting, a number of factors must be considered for realistic deployment. From an implementation and performance perspective, the large size of the inverse problem necessitated the careful selection of matrix solvers and programming of parallel computing routines that proved effective with the availability of a number of processors. Initial predictions based on sequential execution times needed to handle the high degrees of freedom in the naive reconstructions were thus reduced from two weeks to several hours. Additional challenges were eventually overcome in the pre-processing load of image segmentation, model generation and partitioning schemes.

The results presented in this paper also further our understanding of how the loss of input data quality, whether through design limitations or unpredictable factors, could have a significant impact on the end reconstruction. In particular, the proper application of accurate

boundary conditions plays a critical role in MIE reconstruction success. This is due to the link between surface shape matching and subsequent interpolation of internal displacements in affecting sub-surface image intensities and similarity measurements. The results of the boundary condition noise experiment are interesting because they indicate that some level of improper localization of surface point correspondence is reasonably tolerated by the algorithm. However, perturbations greater than an empirically observed threshold can impair its ability to determine the underlying elasticity distribution. This is a similar result to prior work done in 2D systems for which successful reconstructions correlated to boundary condition selection errors limited to half a pixel length (Ou *et al* 2006b). It also confirms that randomizing the vectors for the additive noise experiments poses a considerable challenge to the algorithm because of the introduction of grossly non-physical deformations in the finite element mesh that decrease the stability of the numerical model. We observed that the threshold for the MR simulation was an order of magnitude less than that of the CT set and initially seemed to require an unfeasible level of accuracy, as well as quite a few more fiducials. These key differences are likely related to image resolution (the MR volume had fewer slices and a larger voxel spacing) and to the inherent differences in soft-tissue contrast between the two modalities. Both issues present interesting questions that will be explored in future work.

The implausibility of performing manual selection on all boundary nodes of a 3D mesh (there were 6319 points for the CT and 5416 for the MR set) underscores the importance of finding an automated method for determining point correspondences. In general, energy matching from the solutions of the diffusion and Laplace equations yielded boundary condition sets that were inadequate for reconstructing a proper elasticity contrast. This can be partly explained because the TRE of those surface registration techniques (as compared to the gold standard) was typically greater than the permissible value established by the robustness tests. The primary manifestation of these poor matches was that the model often had difficulty in obtaining a stable solution. Indeed, only the boundary conditions generated by thin-plate spline method, which had the least error, were able to consistently achieve successful reconstructions while also satisfying the putative cutoffs. Overall, the reconstruction behavior for this method was consistent to within 6% of the true value. This appears to recommend the use of thin-plate spline interpolation as a strong candidate for generating boundary conditions for MIE.

5. Conclusions

In this work, we have presented the first fully 3D realization of the MIE algorithm and preliminary evaluation of accompanying strategies for automated boundary condition deployment. The use of parallel processing enabled a practical implementation of a computational problem that might otherwise prove intractable. Simulation experiments demonstrate the viability of the method to utilize images obtained from different sources in reconstructing an embedded lesion with or without the benefit of *a priori* information concerning its location and size. We have also characterized the robustness of the elastography method to inaccuracies in boundary condition inputs derived from either random noise or by surface point correspondence methods. These results should prove valuable in the customization and streamlining of data acquisition and pre-processing for forthcoming clinical tests.

Acknowledgments

The authors would like to acknowledge John Boone, PhD (University of California-Davis Medical Center, Department of Radiology), for the donation of the CT data set, and Prashanth

Dumpuri, PhD (Vanderbilt University, Department of Biomedical Engineering), for software development support. Additional thanks goes to the Vanderbilt Advanced Computing Center for Research and Education for the use of cluster resources. This work was funded by a Breast Cancer Research Program Predoctoral Traineeship Award (BC043661) of the Congressionally Directed Medical Research Program along with a Whitaker Foundation Young Investigator Award. TE Yankeelov is supported by NIBIB 1K25EB005936-01.

References

- ACS 2007 *Cancer Facts and Figures* (Atlanta: American Cancer Society)
- Ahmdahl G 1967 Validity of the single processor approach to achieving large-scale computing capabilities *AFIPS Conf. Proc.* pp 483–5
- Balay S, Buschelman K, Eijkhout V, Gropp W, Kaushik D, Knepley M, McInnes L, Smith B and Zhang H 2004 *PETSc Users Manual* (Argonne, IL: Argonne National Laboratory)
- Balay S, Gropp W D, McInnes L C and Smith B F 1997 *Modern Software Tools in Scientific Computing* (Basle: Birkhauser) pp 163–202
- Bilgen M 1999 Target detectability in acoustic elastography *IEEE Trans. Ultrason. Ferroelectr. Freq. Control* **46** 1128–33
- Boone J M, Kwan A L, Yang K, Burkett G W, Lindfors K K and Nelson T R 2006 Computed tomography for imaging the breast *J. Mammary Gland Biol. Neoplasia* **11** 103–11
- Boone J M and Lindfors K K 2006 Breast CT: potential for breast cancer screening and diagnosis *Future Oncol. (London, England)* **2** 351–6
- Boone J M, Nelson T R, Lindfors K K and Seibert J A 2001 Dedicated breast CT: radiation dose and image quality evaluation *Radiology* **221** 657–67
- Boresi A and Chong K P 1999 *Elasticity in Engineering Mechanics* (New York: Wiley-Interscience)
- Curiel L, Souchon R, Rouviere O, Gelet A and Chapelon J Y 2005 Elastography for the follow-up of high-intensity focused ultrasound prostate cancer treatment: initial comparison with MRI *Ultrasound Med. Biol.* **31** 1461–8
- Doyley M M, Srinivasan S, Dimidenko E, Soni N and Ophir J 2006 Enhancing the performance of model-based elastography by incorporating additional *a priori* information in the modulus image reconstruction process *Phys. Med. Biol.* **51** 95–112
- Doyley M M, Srinivasan S, Pendergrass S A, Wu Z and Ophir J 2005 Comparative evaluation of strain-based and model-based modulus elastography *Ultrasound Med. Biol.* **31** 787–802
- Doyley M M, Weaver J B, Van Houten E E, Kennedy F E and Paulsen K D 2003 Thresholds for detecting and characterizing focal lesions using steady-state MR elastography *Med. Phys.* **30** 495–504
- Egorov V, Ayrapetyan S and Sarvazyan A P 2006 Prostate mechanical imaging: 3-D image composition and feature calculations *IEEE Trans. Med. Imaging* **25** 1329–40
- Fitzpatrick J M, Hill D L G and Maurer C R 2000 *Handbook of Medical Imaging* (Bellingham, WA: SPIE Optical Engineering Press) pp 447–513
- Fowlkes J B, Emelianov S Y, Pipe J G, Skovoroda A R, Carson P L, Adler R S and Sarvazyan A P 1995 Magnetic-resonance imaging techniques for detection of elasticity variation *Med. Phys.* **22** 1771–8
- Garra B S, Cespedes E I, Ophir J, Spratt S R, Zurbier R A, Magnant C M and Pennanen M F 1997 Elastography of breast lesions: initial clinical results *Radiology* **202** 79–86
- Gokhale N, Richards M, Oberai A, Barbone P E and Doyley M M 2004 Simultaneous elastic image registration and elastic modulus reconstruction *IEEE Int. Symp. on Biomedical Imaging* (Arlington, VA: IEEE Press) pp 543–6
- Goshtasby A 1988 Registration of images with geometric distortions *IEEE Trans. Geosci. Remote Sens.* **26** 60–4
- Joachimowicz N, Pichot C and Hugonin J P 1991 Inverse scattering: an iterative numerical method for electromagnetic imaging *IEEE Trans. Biomed. Eng.* **39** 1742–52
- Krouskop T A, Wheeler T M, Kallel F, Garra B S and Hall T 1998 Elastic moduli of breast and prostate tissues under compression *Ultrason. Imaging* **20** 260–74
- Lapidus L and Pinder G F 1982 *Numerical Solution of Partial Differential Equations in Science and Engineering* (New York: Wiley)
- Manduca A, Oliphant T E, Dresner M A, Mahowald J L, Kruse S A, Amromin E, Felmlee J P, Greenleaf J F and Ehman R L 2001 Magnetic resonance elastography: non-invasive mapping of tissue elasticity *Med. Image Anal.* **5** 237–54
- McKnight A L, Kugel J L, Rossman P J, Manduca A, Hartmann L C and Ehman R L 2002 MR elastography of breast cancer: preliminary results *AJR Am. J. Roentgenol.* **178** 1411–7

- Melodelima D, Bamber J C, Duck F A, Shipley J A and Xu L 2006 Elastography for breast cancer diagnosis using radiation force: system development and performance evaluation *Ultrasound Med. Biol.* **32** 387–96
- Miga M I 2002 A new approach to elastographic imaging: modality independent elastography *Med. Imag. 2002: Image Processing* (San Diego, CA: SPIE Press) pp 604–11
- Miga M I 2003 A new approach to elastography using mutual information and finite elements *Phys. Med. Biol.* **48** 467–80
- Miga M I, Rothney M P and Ou J J 2005 Modality independent elastography (MIE): potential applications in dermoscopy *Med. Phys.* **32** 1308–20
- Muthupillai R, Lomas D J, Rossman P J, Greenleaf J F, Manduca A and Ehman R L 1995 Magnetic resonance elastography by direct visualization of propagating acoustic strain waves *Science* **269** 1854–7
- Ophir J, Cespedes I, Ponnekanti H, Yazdi Y and Li X 1991 Elastography: a quantitative method for imaging the elasticity of biological tissues *Ultrason. Imaging* **13** 111–34
- Ophir J, Garra B, Kallel F, Konofagou E, Krouskop T, Righetti R and Varghese T 2000 Elastographic imaging *Ultrasound Med. Biol.* **26** (Suppl 1) S23–9
- Otsu N 1979 Threshold selection method from gray-level histograms *IEEE Trans. Syst. Man Cybern.* **9** 62–6
- Ou J J, Barnes S L and Miga M I 2006a Application of multi-resolution modality independent elastography for detection of multiple anomalous objects *Medical Imaging 2006: Physiology, Function and Structure from Medical Images* (San Diego, CA: SPIE Press) pp 614310-1–9
- Ou J J, Barnes S L and Miga M I 2006b Preliminary testing of sensitivity to input data quality in an elastographic reconstruction method *IEEE Int. Symp. Biomed. Imaging* (Arlington, VA: IEEE Press) pp 948–51
- Papademetris X, Sinusas A J, Dione D P, Constable R T and Duncan J S 2002 Estimation of 3-D left ventricular deformation from medical images using biomechanical models *IEEE Trans. Med. Imaging* **21** 786–800
- Parker K J, Taylor L S, Gracewski S and Rubens D J 2005 A unified view of imaging the elastic properties of tissue *J. Acoust. Soc. Am.* **117** 2705–12
- Samani A, Zubovits J and Plewes D 2007 Elastic moduli of normal and pathological human breast tissues: an inversion-technique-based investigation of 169 samples *Phys. Med. Biol.* **52** 1565–76
- Sarvazyan A P, Skovoroda A R, Emelianov S Y, Fowlkes J B, Pipe J G, Adler R S, Buxton R B and Carson P L 1995 *Acoustical Imaging* ed J P Jones (New York: Plenum) pp 223–40
- Sinkus R, Lorenzen J, Schrader D, Lorenzen M, Dargatz M and Holz D 2000 High-resolution tensor MR elastography for breast tumour detection *Phys. Med. Biol.* **45** 1649–64
- Tsap L V, Goldgof D B, Sarkar S and Powers P S 1998 A vision-based technique for objective assessment of burn scars *IEEE Trans. Med. Imaging* **17** 620–33
- Washington C W and Miga M I 2004 Modality independent elastography (MIE): a new approach to elasticity imaging *IEEE Trans. Med. Imaging* **23** 1117–28
- Yankeelov T E *et al* 2007 Integration of quantitative DCE-MRI and ADC mapping to monitor treatment response in human breast cancer: initial results *Magn. Reson. Imaging* **25** 1–13
- Zhang Y, Goldgof D B and Sarkar S 2004 Significance of elastic properties in physics-based nonrigid motion modeling: a numerical sensitivity analysis *CVPRW* p 21

An Elastography Framework for Use in Dermoscopy

Michael I. Miga^{1,2,a}, Jao J. Ou¹, Darrel L Ellis³

¹Vanderbilt University, Department of Biomedical Engineering, Nashville, TN 37235

²Vanderbilt University Medical Center, Department of Radiology and Radiological Sciences,
Nashville, TN 37232

³Vanderbilt University Medical Center, Department of Medicine, Division of Dermatology,
Nashville, TN 37232

^acorresponding author

(Michael.I.Miga, Jao.J.Ou, Darrel.L.Ellis)@vanderbilt.edu

ABSTRACT

Multiple skin conditions exist which involve clinically significant changes in elastic properties. Early detection of such changes may prove critical in formulating a proper treatment plan. However, most diagnoses still rely primarily on visual inspection followed by biopsy for histological analysis. As a result, there would be considerable clinical benefit if a noninvasive technology to study the skin were available. The primary hypothesis of this work is that skin elasticity may serve as an important method for assisting diagnosis and treatment. Perhaps the most apparent application would be for the differentiation of skin cancers, which are a growing health concern in the United States as total annual cases are now being reported in the millions by the American Cancer Society. In this paper, we use our novel modality independent elastography (MIE) method to perform dermoscopic skin elasticity evaluation. The framework involves applying a lateral stretching to the skin in which dermoscopic images are acquired before and after mechanical excitation. Once collected, an iterative elastographic reconstruction method is used to generate images of tissue elastic properties and is based on a two-dimensional (2-D) membrane model framework. Simulation studies are performed that show the effects of three-dimensional data, varying subdermal tissue thickness, and nonlinear large deformations on the framework. In addition, a preliminary in vivo reconstruction is demonstrated. The results are encouraging and indicate good localization with satisfactory degrees of elastic contrast resolution.

KEY WORDS: Elastography, Dermoscopy, Mechanical Properties, Finite Element, Image Similarity, Elasticity Imaging

1. INTRODUCTION

Because multiple conditions exist which involve clinically significant changes in skin elasticity, early detection of such changes could prove critical in formulating a proper treatment plan. However, most diagnoses still rely primarily on visual inspection followed by biopsy of suspect areas for histological analysis. Perhaps the most apparent application would be for the differentiation of skin cancers, which are a growing health concern in the United States as total annual cases are now being reported in the millions by the American Cancer Society¹. Of the three major types of skin cancer reported annually, basal cell carcinoma (BCC) makes up approximately 800,000+, squamous cell carcinoma (SCC) cases number approximately 200,000+, and a remaining 60,000+ melanoma cases. With respect to BCC, approximately 5-10% of these can be aggressive and infiltrate the surrounding tissue and sometimes into bone and cartilage. It rarely metastasizes but can cause scars and disfigurement. With respect to SCC, early detection is the key to successful treatment. If left unchecked, SCC can also cause

disfigurement and typically approximately 3-4% of cases results in metastasis which is usually fatal. Melanoma is the most fatal. Melanoma is malignant and if left unchecked, it will spread to other parts of the body, becomes difficult to treat, and can be fatal. If one were to include among the common cancer statistics, aggressive BCC's and metastatic SCC's, skin cancer would likely be the second most prevalent among newly diagnosed cancers.

While the above statistics are compelling, when speaking to lethality, skin cancer is less significant than its more fatal counterparts in breast, lung, colon/rectal, and prostate. However when considering the economic cost that skin cancer incurs on US healthcare, the pursuit of skin cancer characterization has considerable merit. The ability to differentiate benign from malignant, and aggressive from non-aggressive skin lesions would provide considerable savings to health care costs within the United States. Each year it is estimated that approximately 5-7 million patients undergo biopsies for skin cancer with only a fraction resulting in malignancies. While complete multi-center biopsy studies have not been performed, one study that took place documented the percentage of skin biopsy specimens that were malignant, i.e. they termed this the "malignancy ratio"². In this study, the malignancy was approximately 40% with a very wide variability among the 22 dermatologists (13.4-86.6%) that participated in the study. If one considers 5 million biopsies, this would translate to approximately 3 million unnecessary biopsies per year, and approximately \$300-600 million in saved expenditures per year^{3,4}. Furthermore, this does not even include cosmetic surgery costs in the case of scarring or complications associated with bleeding and infections. If an inexpensive imaging device could differentiate lesions with reasonably high specificity and sensitivity, it would have considerable significance.

It should also be noted that measuring cutaneous elasticity is also potentially important to medical areas outside of clinical dermatology. For instance, in a recent study of 100 women receiving hormone replacement therapy, Pierard *et al* demonstrated a positive correlation between bone mass density and skin elasticity^{5,6}. Another study conducted by Yoon *et al* showed a similar relevance for patients afflicted with diabetes mellitus⁷. Further uses for evaluating skin elasticity range from surgery (minimization of scarring, chronic graft versus host disease) to rheumatology (scleroderma, lupus) to obstetrics (striae development in pregnancy)⁸⁻¹².

With respect to diagnostic technological advances, developments have been concerned with obtaining a better view of the skin, either via improved optics (i.e. dermoscopy) or by more advanced and novel imaging systems ranging from high-frequency ultrasound to confocal laser microscopy^{13,14}. Other strategies involving electrical impedance mismatch¹⁵, Raman spectroscopy¹⁶, and cytological smears¹⁴ have also been forthcoming. In lieu of these methods that capitalize on electrical, optical, and biochemical phenomena, we have chosen to pursue an approach which is based on analyzing mechanical behavior of the skin. Detecting changes in tissue by palpation and then associating them with a disease state has a long-standing history in clinical medicine, and utilizing changes in the mechanical properties to specifically characterize the skin does have precedent. A thoughtful review by Edwards and Marks discusses the complex mechanical behavior of skin when subjected to in vitro and in vivo testing¹⁷. Their review highlights extensive methodologies being used to quantify skin properties (e.g. uni-axial and bi-axial extensometry, torsion stimulators, indentometry, ballistometric tests, shear wave application devices, dynamic suction methods, ultrasonics, and electrodynamicometry) and also emphasizes the difficulties in comparing across these methods. One of the authors' conclusions is that the need for quantitative reproducible methods to assess skin health is necessary given the considerable subjectivity in clinical analysis.

Following previous work in¹⁸, we are developing a new method we have termed 'modality-independent elastography' (MIE) that combines image processing with an inverse problem. More specifically, image similarity metrics routinely used with image registration methods are recast to satisfy an inverse elasticity problem framework whereby mechanical properties within a biomechanical model of deforming tissue become the driving parameters for improved image similarity. In this way, MIE circumvents two potential limitations of current elastographic techniques. First, it is not inherently

dependent on pre-processing steps such as homologous feature selection and tracking which drive active contour models¹⁹⁻²¹ and other traditional displacement-based iterative methods²²⁻²⁴, although such techniques can aid in the determination of boundary conditions. Secondly, because it is an image processing methodology, MIE is not reliant on a particular imaging modality (such as in ultrasound and magnetic resonance elastography) as long as the acquired images provide sufficient pattern to allow for comparison. Building upon recently with a multi-resolution implementation²⁵, this paper presents analysis using a tissue model that incorporates geometric nonlinearities, the effects of the three-dimensional nature of the problem which include varying subcutaneous layer thicknesses, and varying lesion depth. In addition, a relatively crude preliminary *in vivo* result is also demonstrated.

2. MATERIALS AND METHODS

2.1. Modality Independent Elastography

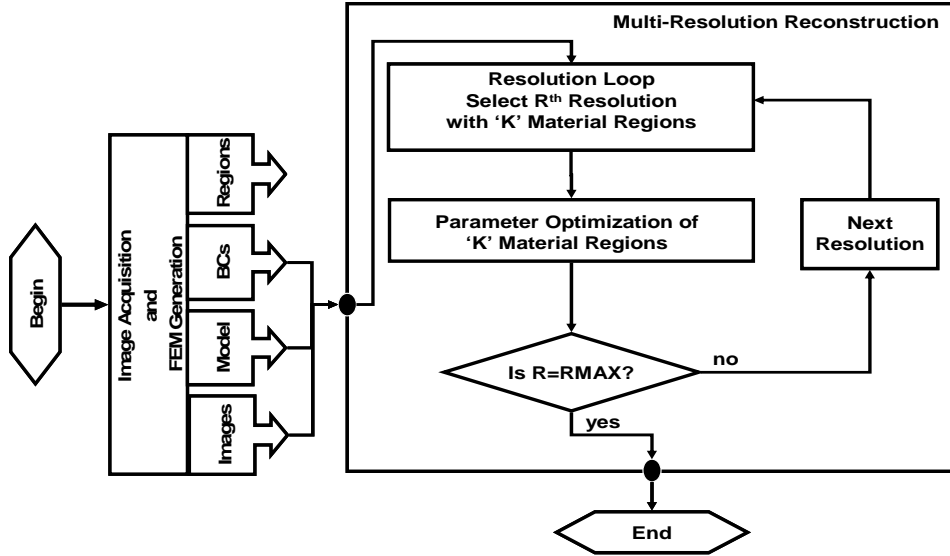


Fig 1. MIE framework.

MIE begins with the acquisition of an image series consisting of an image acquired prior to and after an applied deformation. The method is “independent” because it does not require any specific imaging modality but rather that sufficient pattern is present within the acquired images such that material properties can be assessed from pattern changes within the acquisition-pair. This is a similar requirement for many methods of non-rigid image registration. At its core MIE is an image analysis method whereby a model-generated deformation field is applied to the pre-deformed image series (*source*) and compared to its acquired deformed counterpart (*target*). This comparison is nested within a Levenberg-Marquardt optimization routine such that the material properties become the parameters of interest in matching the model-deformed *source* image to the acquired *target* image. The methods and development of this technique have been reported in detail elsewhere^{18, 25-29}.

With respect to the optimization framework for MIE, it can be represented as a least squared error objective function:

$$\phi(\vec{E}) = \min \left\{ \left\| \mathbf{S}(\vec{E}_t) - \mathbf{S}(\vec{E}_E) \right\|^2 \right\} \quad (1)$$

where $\mathbf{S}(\vec{E}_t)$ is the similarity value achieved when comparing the target image to itself (i.e. the maximum value for the similarity measure, so for the correlation coefficient $\mathbf{S}(\vec{E}_t) = 1$) and $\mathbf{S}(\vec{E}_E)$ is the similarity between the model-deformed source image and the acquired target image using the current estimate of the

elastic modulus. Eq. (1) is optimized by setting the partial derivative equal to zero and solved using a Levenberg-Marquardt approach:

$$[\mathbf{J}^T][\mathbf{J}] + \alpha[\mathbf{I}]\{\Delta\bar{\mathbf{E}}\} = [\mathbf{J}^T]\{\mathbf{S}(\bar{\mathbf{E}}_t) - \mathbf{S}(\bar{\mathbf{E}}_E)\} \quad (2)$$

where $[\mathbf{J}]$ is the $M \times N$ Jacobian matrix of the form $\mathbf{J} = \frac{\partial \mathbf{S}(\bar{\mathbf{E}}_E)}{\partial \bar{\mathbf{E}}}$ and M is the number of similarity measurements (i.e. zones) being made and N is the number of material property regions. Because $[\mathbf{J}^T][\mathbf{J}]$ (an approximation to the Hessian matrix) tends to be ill-conditioned, it is regularized with an empirically determined α parameter found in the standard Levenberg-Marquardt approach³⁰. The determination of this regularization parameter is described in³¹. The multi-resolution framework to MIE is shown in Fig. 1. The methodology used involves a hierarchical material parameter resolution series. This has been reported elsewhere^{25, 27} and has been shown to assist in avoiding local minima that are associated with the decorrelation of patterned data.

2.2. Model for Skin

One critical component within all model-based inverse problem frameworks is the selection of the computer model to represent the continuum of interest. In previous phantom, simulation, and in vivo studies, we have elected to employ a plane stress linear elastic model to simulate the skin. This model is a two dimensional approximation of the three dimensional system which assumes a symmetric, isotropic, thin specimen in equilibrium, and stresses that are constrained to lie within the plane. These assumptions simplify Cauchy's law from 36 stiffness constants to 2 and use the equation:

$$\nabla \cdot \boldsymbol{\sigma} = \mathbf{0} \quad (3)$$

where $\boldsymbol{\sigma}$ is the 2D Cartesian stress tensor and is defined below followed by the plane stress constitutive equations:

$$\begin{bmatrix} \sigma_x \\ \sigma_y \\ \tau \end{bmatrix} = \frac{E}{(1-\nu)^2} \begin{bmatrix} 1 & \nu & 0 \\ \nu & 1 & 0 \\ 0 & 0 & \frac{1-\nu}{2} \end{bmatrix} \begin{bmatrix} \partial u / \partial x \\ \partial v / \partial y \\ \partial v / \partial x + \partial u / \partial y \end{bmatrix} \quad (4)$$

where E is Young's modulus, and ν is Poisson's ratio. For this work, we have determined that a Poisson's ratio of 0.485 for our skin phantoms and tissue work has performed reasonably well. This value would correlate with a ~32:1 ratio of the Lamé' constants ($\lambda : \mu$, with μ the shear modulus, and λ being the second Lamé' constant) which is reasonably below the convention for Poisson locking (sometimes called mesh locking and typically has $\lambda \gg \mu$) although one could argue that hyperelastic models may be the more appropriate model and will need to be explored in the future. Using the Galerkin weighted residual method to integrate and solve this set of partial differential equations, a finite element framework is generated and can be solved to represent a displacement field for a given distribution of Young's modulus.

In this paper, the plane stress model has been enhanced to incorporate the full Green-Lagrange strain tensor as defined by:

$$\varepsilon_{i,j} = \frac{1}{2} \left(\frac{\partial \mathbf{u}_i}{\partial \mathbf{x}_j} + \frac{\partial \mathbf{u}_j}{\partial \mathbf{x}_i} + \frac{\partial \mathbf{u}_k}{\partial \mathbf{x}_i} \frac{\partial \mathbf{u}_k}{\partial \mathbf{x}_j} \right). \quad (6)$$

Use of this tensor description abandons the traditional small-strain approximation in favor of one compatible with large deformations. The difference in solutions between small and large deformation theory can be seen in the 2D simulations shown in Fig. 2. Fig. 2 compares the boundary shape of a

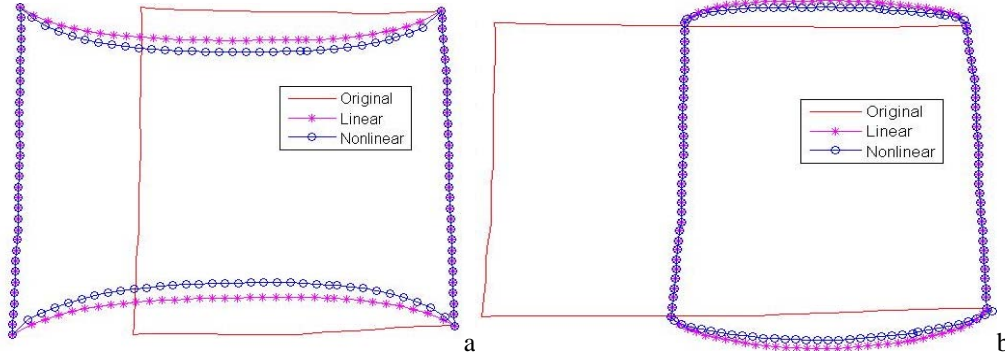


Fig. 2. (a) Fixed ~30-40% tensile strain applied to original with linear and nonlinear model, (b) ~30-40% compressive strain.

Hookean linear elastic membrane to a 2D Hookean geometrically nonlinear elastic model. For these simulations, a plane stress approximation was performed *for comparison only* of the solution due to nonlinear terms (i.e. a ~30-40% compressive stress could never be applied to a thin specimen, the material would buckle well before). The important aspect to notice is that more necking and less bulging occur in the nonlinear than the linear model in tension, and compression, respectively. With respect to the difference in the linear model among Fig. 2a and 2b, 2b is the reverse of 2a (this is a characteristic of linear theory). However, the lack of this symmetry for the nonlinear model is characteristic of the Green-Lagrange strain tensor and is caused by the interplay between the linear and quadratic terms in the tensor. In this paper, the results from the linear and nonlinear model will be compared.

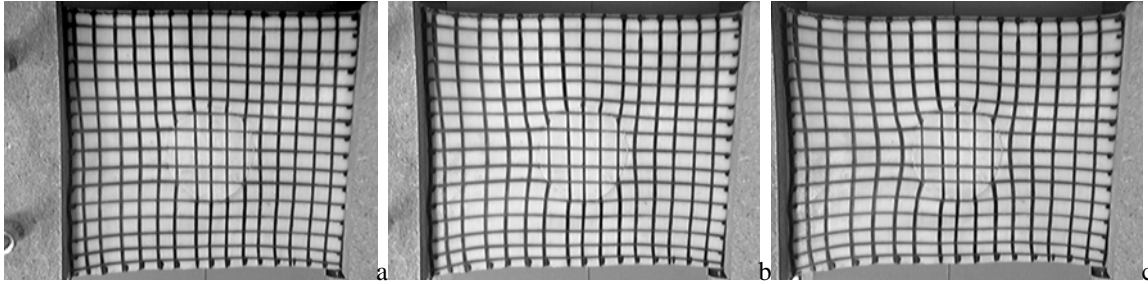


Fig 3. Phantom membrane stretches (a) baseline, (b) 1 cm stretch, (c) 2 cm stretch.

2.3. Nonlinear Model Experiments

In previous work, a phantom of simulated skin was generated from using a polyurethane membrane 25 cm long, 15 cm wide, and approximately 2 mm thick containing two types of materials. The bulk material, representing “normal” skin, was chosen to be Evergreen 10 (Smooth-On, Easton, PA), while the stiffer Evergreen 50 was used to create a 5 cm circular inclusion of full depth and was placed at the center of the phantom. The visible surface of the phantom was modified by drawing a regular grid of horizontal and vertical lines spaced about 1 cm apart in either direction. Fig. 3 shows the skin phantom as acquired by an optical camera at the baseline, 1 cm, and 2cm stretch levels. Separate mechanical tests on the membrane were conducted using the EnduraTEC ELF 3200 material tester (EnduraTEC Systems Group, Bose Corporation, Minnetonka, MN)²⁵. Table 1 reports the expected Young’s Modulus contrast ratio based on a Hookean solid fitted to each respective stretch/strain level. The scale of lesion to field-of-view size is the anticipated aspect ratio for a dermoscopic system. This

Stretch	CR (Linear)	CR (Nonlinear)
1 (0.5 cm)	5.7	5.0
2 (1.0 cm)	5.0	4.8
3 (1.5 cm)	4.6	4.7
4 (2.0 cm)	4.2	4.4

Table 1. Expected elastic contrast ratio.

image data was used as an input to the MIE framework, and reconstructions comparing the linear and nonlinear model were generated.

2.4. Three-Dimensional Model Experiments

In an effort to test the MIE algorithm with more realistic images of the skin as would be expected in the clinic, a simulation study was performed on an image obtained from the Dermatology Image Atlas project (www.dermatlas.org, “melanoma_1_040510”, contributed by Eric Ehlers, M.D., Fig. 4a). Dermoscopic images provide the challenge of relying on the natural pattern instead of the structured grid used in the membrane phantom experiments (although the skin could be printed upon with an ink grid). Previous simulation work on this image can be found in ²⁵.

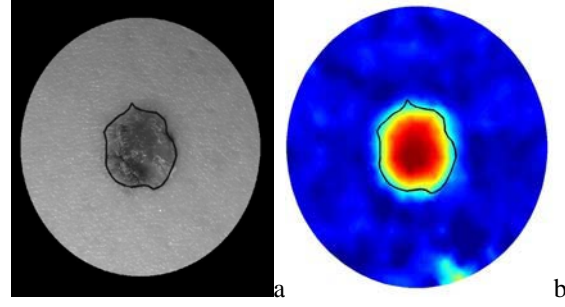


Fig. 4. (a) Melanoma lesion, with (b) sample reconstruction.

One possible critique of this dermoscopic framework is the fear that underlying layers would confound the approach. As a result, we have modified the simulation study reported in ²⁵ (e.g. Fig. 4b) to be more realistic. Fig. 5a-5c shows the setup of the new simulation study. In this study, six $10\text{ cm} \times 10\text{ cm}$ domains were constructed which had different layered structures. Three domains were 6mm in total thickness ($\sim 4\text{mm}$ epidermis/dermis, 2mm subcutaneous) and had 1cm central inclusions varying in depth 1mm , 2mm , and 3mm , respectively. The remaining three domains were the same except that the subcutaneous layer thickness was increased to 7mm . The selection of subcutaneous layer thickness ^{32, 33} and stiffness values ³⁴ were based on the literature. Using this domain, a mechanical aperture that stretched the skin was simulated, 3D displacements were calculated (Fig. 5b), and then projected on to the

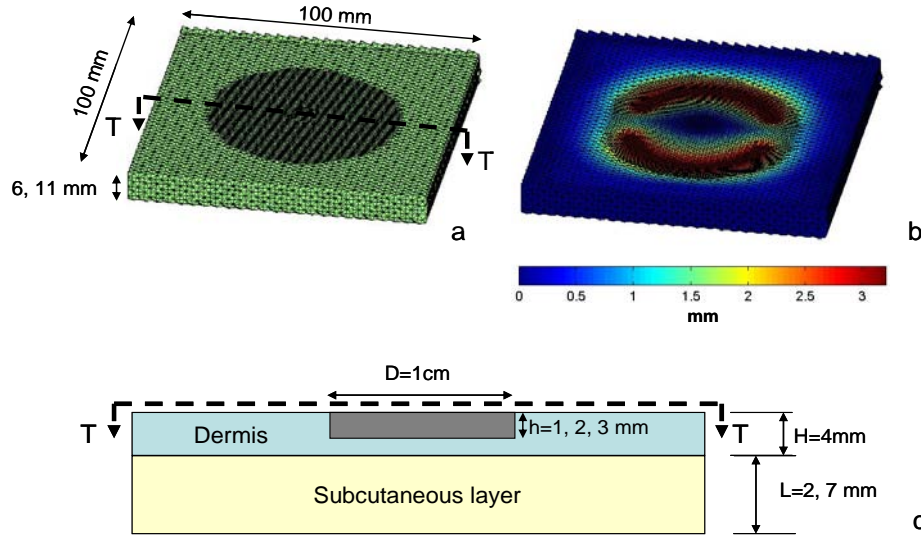


Fig. 5. (a) Mesh with refinement in lesion area, (b) simulated compression of skin by device, and (c) depth variation (transect T is shown in (a)).

original 2D mesh. A new set of simulated images (deforming Fig. 4) was generated and then used as input to the 2D MIE algorithm.

2.5 Noninvasive In Vivo Experiments

In addition to the simulation experiments, a second camera and deformation system was constructed using a Sony XCD-X710CR CCD camera with a Schneider 12 mm lens and a circular

polarizing filter for the optics mounted over a crude spring-loaded standard set of pincers that were pressed against the skin surface and bound with commercial adhesive. Digital images (800 x 600 resolution) of a common nevus of palpable stiffness that was 2-3 mm in diameter and located on the volar aspect of the left forearm of a male volunteer were acquired in both relaxed and stretched states. It was determined that the reflection and scattering of ambient fluorescent lighting interfered with this particular setup and affected the input image quality, so an artificial grid was imposed to counteract specularly.

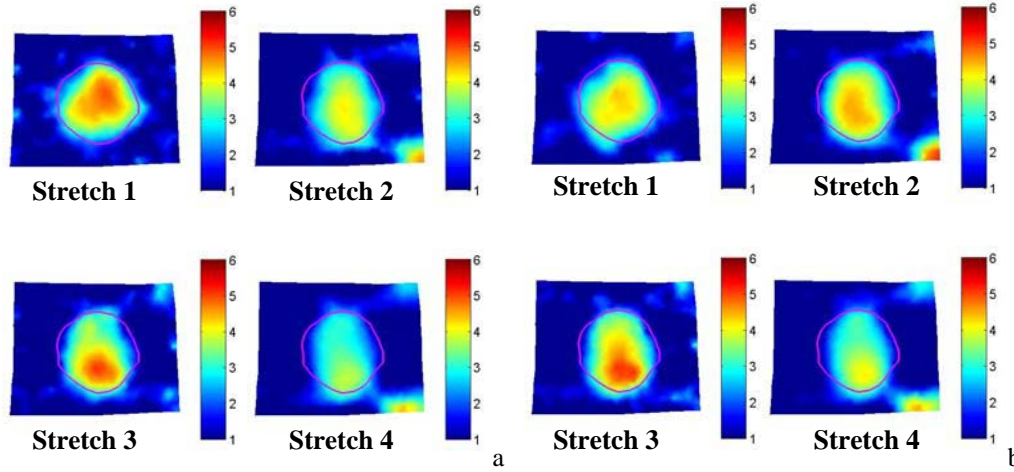


Fig 6. (a) Linear Hookean reconstructions for each stretch state, and (b) the geometrically nonlinear Hookean reconstructions. Contour shows inclusion border.

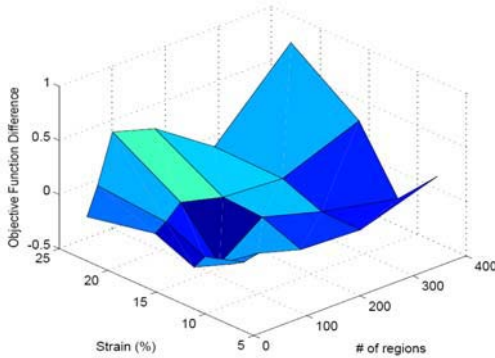


Fig 7. Objective function difference between linear and nonlinear models over all stretches and resolutions.

approximate contrast ratio of the lesion-to-bulk material for each of the cases shown in Fig. 8. Fig 9. illustrates the results from the *in vivo* experiment conducted. Fig. 9 shows (a) the nevus, (b) the finite element grid, and (c,d) reconstructed elasticity images. Fig. 9c-d illustrate the effect of incorporating increasing degrees of *a priori* knowledge of the actual location and elasticity distribution into the algorithm. Fig. 9c is a general elasticity reconstruction of the nevus with lesion-related initial guess, and Fig. 9d maintains the spatial *prior* of Fig. 9c for the entire duration of the reconstruction process.

4. DISCUSSION

With respect to Fig. 6, the most important features to note are a very subtle improvement in satisfying the inclusion contour, and the decrease in variability of the contrast in the geometric nonlinear reconstructions. This is consistent with the behavior in Table 1 and indicates that the geometric nonlinear reconstruction is performing as predicted. One thing to note is that if the membrane were a true Hookean

Images were acquired in the baseline and stretched state and given to the MIE algorithm.

3. RESULTS

Fig. 6 illustrates the reconstructions of the phantom membrane system using the linear and nonlinear models, respectively. Fig. 7 reports how the objective function varies between the linear and nonlinear model reconstructions of Fig. 6. Fig. 8 demonstrates the dependence of resolving stiffness (3:1, 6:1, 12:1) on depth (1, 2, 3 mm) for the 18 combinations (combinations of 3 depths, 3 contrast ratios, and 2 subcutaneous layer thicknesses). Table 2 reports an

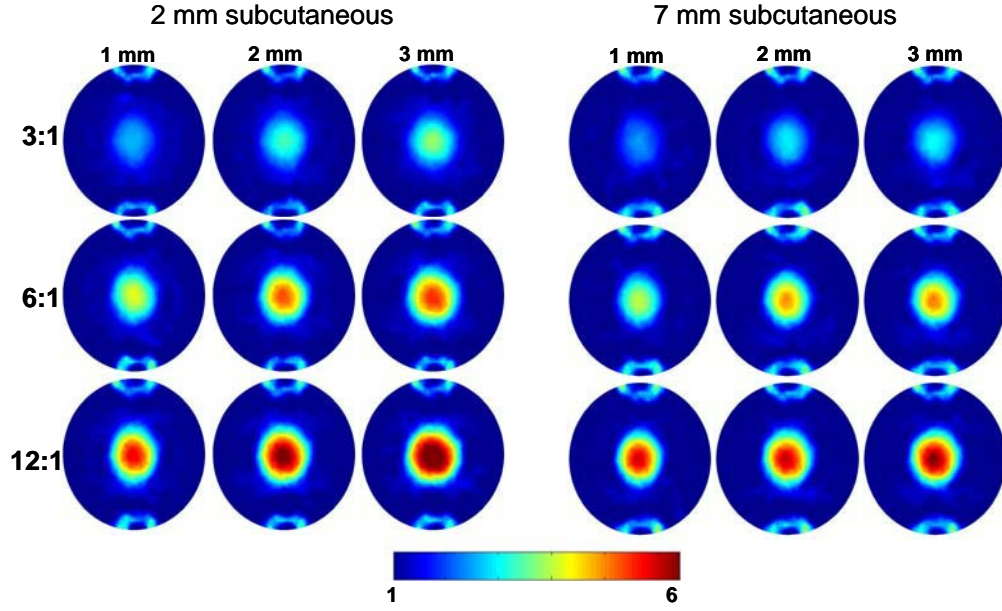


Fig. 8. 3-D effects on elasticity images with varying lesion depth and subcutaneous layer depth. Ratio on left shows actual contrast while colorbar shows reconstructed. Fig. 4 shows the lesion contour.

2mm SQ	1 mm	2 mm	3 mm
3:1	2.12	2.55	2.79
6:1	3.08	3.76	4.00
12:1	4.11	4.71	5.15

7mm SQ	1 mm	2 mm	3 mm
3:1	1.93	2.27	2.34
6:1	2.87	3.49	3.55
12:1	4.03	4.28	4.53

Table 2. Lesion-to-bulk contrast ratio at each lesion depth (1mm, 2mm, 3mm) and target contrast level (3:1, 6:1, 12:1) for 2mm (top) and 7mm (bottom) subcutaneous thicknesses.

nonlinear solid, the CR would be the same across all stretches, i.e. strain levels. While the variability across levels was reduced between the linear and nonlinear models for strain, the data supports a more complex constitutive model for this phantom system. Fig. 7 also demonstrates some consistency with the extension to a nonlinear model. Here we see that at the largest stretch values, the difference between the two models is highest with the nonlinear model outperforming the linear.

With respect to Fig. 8, and Table 2, despite not reaching the expected contrast ratio values, each result localized the lesion and demonstrated sensitivity to depth and contrast. With respect to contrast ratio, this

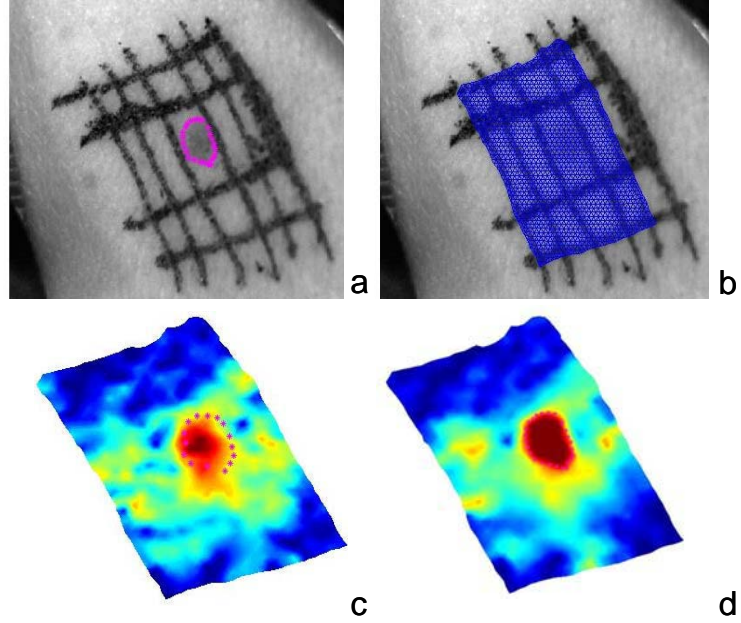


Fig. 9. (a) Dermoscopic scale interrogation (magenta border is about 3 mm in diameter), (b) reconstruction mesh, (c) general elasticity reconstruction, (d) incorporation of lesion border as *a priori* information.

simulation was more challenging than previous work. The results indicate that varying subcutaneous thicknesses has a very modest effect in confounding lesion reconstructions for the contrast regime shown. Fig. 8 does suggest that at some contrast levels there may be overlap (e.g. a 3mm, 3:1 lesion with 2mm subcutaneous layer may be confused with a 1mm, 6:1 lesion with 7mm subcutaneous layer). This could be potentially confounding if left in the absence of other information. However, Horejsi et al. and Moller et al.^{32, 33} do provide guidance for estimating the subcutaneous tissue thickness in a general population. Additionally, they use a relatively inexpensive optical device to make these measurements. There is little doubt that using this *a priori* information would reduce variability in interpretation. It is interesting to speculate that if a particular lesion type was of a known stiffness *a priori* then perhaps the reconstruction contrast could be used to estimate lesion depth. Looking across the grids of a particular property contrast, there is a definitive change in the reconstruction as a function of depth.

Fig. 9 demonstrates a preliminary attempt of applying the framework to an *in vivo* system. Considering there was very little control over this system and no ground truth was available, these results qualitatively confirm the potential utility of MIE in evaluating an area of skin with a region of differing elasticity. While the results in Fig. 9 c,d are not completely satisfying at this time, it should be emphasized that the camera-system employed a coarse resolution, and the skin-to-device coupling system was extremely crude. Given this somewhat ad-hoc experiment, the detection of any anomaly in the correct region is encouraging for this approach. It was also interesting to note the increase in performance by adding the lesion extents to the information provided to the algorithm.

5. CONCLUSIONS

The results from the experiments above demonstrate an ability to use the MIE framework within the dermoscopy setting. Methodological concerns regarding the use of geometric nonlinear models, three-dimensional effects, and *in vivo* conditions are addressed. The results indicate that while geometric nonlinearities do modestly affect reconstructions, nonlinear material models may be needed to correct for remaining discrepancies. A modest improvement was shown using the geometric nonlinear model especially at large strain values which is consistent with the theoretical development. The three-dimensional effects of lesion depth and varying subcutaneous layer thicknesses are assessed. Lesion depth does affect contrast ratio whereas subcutaneous layers affect the reconstructions to a significantly lesser degree. Avenues to detect lesion depth in the presence of *a priori* knowledge of a lesion's stiffness may have surgical implications. Preliminary *in vivo* work suggests that lesion characterization is possible although specificity and sensitivity of the method await further study and will need a considerably more robust acquisition system.

6. ACKNOWLEDGEMENTS

This work was supported by the Whitaker Foundation's Young Investigator Program and the Whitaker Foundation's Continuation Program. This work was also supported by the Congressionally Directed Medical Research Program—Breast Cancer Research Program.

7. REFERENCES

1. American Cancer Society, "Cancer Facts and Figures 2006," A. C. Society, ed. (Atlanta, GA, 2006).
2. A. R. Green, G. W. Elgart, F. Ma, D. G. Federman, and R. S. Kirsner, "Documenting dermatology practice: Ratio of cutaneous tumors biopsied that are malignant," *Dermatol. Surg.* **30**, 1208-1209 (2004).

3. G. J. Chen, C. B. Yelverton, S. S. Polisetty, T. S. Housman, P. M. Williford, H. V. Teuschler, and S. R. Feldman, "Treatment patterns and cost of nonmelanoma skin cancer management," *Dermatol. Surg.* **32**, 1266-1271 (2006).
4. K. A. Freedberg, A. C. Geller, D. R. Miller, R. A. Lew, and H. K. Koh, "Screening for malignant melanoma: A cost-effectiveness analysis," *Journal of the American Academy of Dermatology* **41**, 738-745 (1999).
5. G. E. Pierard, C. Pierard-Franchimont, S. Vanderplaetsen, N. Franchimont, U. Gaspard, and M. Malaise, "Relationship between bone mass density and tensile strength of the skin in women," *Eur. J. Clin. Invest.* **31**, 731-735 (2001).
6. G. E. Pierard, S. Vanderplaetsen, and C. Pierard-Franchimont, "Comparative effect of hormone replacement therapy on bone mass density and skin tensile properties," *Maturitas* **40**, 221-227 (2001).
7. H. S. Yoon, S. H. Baik, and C. H. Oh, "Quantitative measurement of desquamation and skin elasticity in diabetic patients," *Skin Res. Technol.* **8**, 250-254 (2002).
8. C. Braham, D. Betea, C. Pierard-Franchimont, A. Beckers, and G. E. Pierard, "Skin tensile properties in patients treated for acromegaly," *Dermatology* **204**, 325-329 (2002).
9. D. Carrino, J. Sorrell, and A. Caplan, "Age-related changes in the proteoglycans of human skin," *Archives of Biochemistry and Biophysics* **373**, 91-101 (2000).
10. J. A. Clark, J. C. Y. Cheng, and K. S. Leung, "Mechanical properties of normal skin and hypertrophic scars," *Burns* **22**, 443-446 (1996).
11. H. Dobrev, "In vivo study of skin mechanical properties in psoriasis vulgaris," *Acta Derm.-Venereol.* **80**, 263-266 (2000).
12. H. Sumino, S. Ichikawa, M. Abe, Y. Endo, O. Ishikawa, and M. Kurabayashi, "Effects of aging, menopause, and hormone replacement therapy on forearm skin elasticity in women," *J. Am. Geriatr. Soc.* **52**, 945-949 (2004).
13. A. A. Marghoob, L. D. Swindle, C. Z. M. Moricz, F. A. S. Negron, B. Slue, A. C. Halpern, and A. W. Kopf, "Instruments and new technologies for the in vivo diagnosis of melanoma," *Journal of the American Academy of Dermatology* **49**, 777-797 (2003).
14. E. Ruocco, G. Argenziano, G. Pellacani, and S. Seidenari, "Noninvasive imaging of skin tumors," *Dermatol. Surg.* **30**, 301-310 (2004).
15. R. Dua, D. G. Beetner, W. V. Stoecker, and D. C. Wunsch, "Detection of basal cell carcinoma using electrical impedance and neural networks," *IEEE Trans. Biomed. Eng.* **51**, 66-71 (2004).
16. M. Gniadecka, P. A. Philipsen, S. Sigurdsson, S. Wessel, O. F. Nielsen, D. H. Christensen, J. Hercogova, K. Rossen, H. K. Thomsen, R. Gniadecki, L. K. Hansen, and H. C. Wulf, "Melanoma diagnosis by Raman spectroscopy and neural networks: Structure alterations in proteins and lipids in intact cancer tissue," *J. Invest. Dermatol.* **122**, 443-449 (2004).
17. C. Edwards, and R. Marks, "Evaluation of biomechanical properties of human skin," *Clin. Dermatol.* **13**, 375-380 (1995).
18. M. I. Miga, "A new approach to elastography using mutual information and finite elements," *Phys. Med. Biol.* **48**, 467-480 (2003).
19. L. V. Tsap, D. B. Goldgof, and S. Sarkar, "Nonrigid motion analysis based on dynamic refinement of finite element models," *IEEE Trans. Pattern Anal. Mach. Intell.* **22**, 526-543 (2000).
20. L. V. Tsap, D. B. Goldgof, and S. Sarkar, "Fusion of physically-based registration and deformation modeling for nonrigid motion analysis," *IEEE Trans. Image Process.* **10**, 1659-1669 (2001).
21. L. V. Tsap, D. B. Goldgof, S. Sarkar, and P. S. Powers, "A vision-based technique for objective assessment of burn scars," *IEEE Trans. Med. Imaging* **17**, 620-633 (1998).
22. T. L. Chenevert, A. R. Skovoroda, M. O'Donnell, and S. Y. Emelianov, "Elasticity reconstructive imaging by means of stimulated echo MRI," *Magn. Reson. Med.* **39**, 482-490 (1998).
23. J. Ophir, S. K. Alam, B. Garra, F. Kallel, E. Konofagou, T. Krouskop, and T. Varghese, "Elastography: ultrasonic estimation and imaging of the elastic properties of tissues," *Proc. Inst. Mech. Eng. Part H-J. Eng. Med.* **213**, 203-233 (1999).

24. E. E. W. Van Houten, M. I. Miga, J. B. Weaver, F. E. Kennedy, and K. D. Paulsen, "Three-dimensional subzone-based reconstruction algorithm for MR elastography," *Magn.Reson.Med.* **45**, 827-837 (2001).
25. M. I. Miga, M. P. Rothney, and J. J. Ou, "Modality independent elastography (MIE): Potential applications in dermoscopy," *Medical Physics* **32**, 1308-1320 (2005).
26. M. I. Miga, "A new approach to elastographic imaging: Modality independent elastography," *Medical Imaging 2002: Image Processing: Proc. of the SPIE* **4684**, 604-611 (2002).
27. J. J. Ou, S. L. Barnes, and M. I. Miga, "Application of multi-resolution modality independent elastography for detection of multiple anomalous objects," in *Medical Imaging 2006: Physiology, Function, and Structure from Medical Images: Proc. of the SPIE*, (SPIE, San Diego, CA, 2006).
28. J. J. Ou, S. L. Barnes, and M. I. Miga, "Preliminary testing of sensitivity to input data quality in an elastographic reconstruction method," in *International Symposium on Biomedical Imaging 2006*, (Washington, D.C., 2006).
29. C. W. Washington, and M. I. Miga, "Modality independent elastograph ({MIE}): {A} new approach to elasticity imaging," *IEEE Trans. Med. Imaging* (**in press**), (2004).
30. D. W. Marquardt, "An algorithm for least-squares estimation of nonlinear parameters," *SIAM Journal of Applied Mathematics* **11**, 431-441 (1963).
31. N. Joachimowicz, C. Pichot, and J. P. Hugonin, "Inverse scattering: an iterative numerical method for electromagnetic imaging," *IEEE Trans. Biomed. Eng.* **39**, 1742-1752 (1991).
32. R. Horejsi, R. Moller, T. R. Pieber, S. Wallner, K. Sudi, G. Reibnegger, and E. Tafeit, "Differences of subcutaneous adipose tissue topography between type-2 diabetic men and healthy controls," *Exp. Biol. Med.* **227**, 794-798 (2002).
33. R. Moller, E. Tafeit, K. H. Smolle, T. R. Pieber, O. Ipsiroglu, D. M., C. Huemer, K. Sudi, and G. Reibnegger, "Estimating percentage total body fat and determining subcutaneous adipose tissue distribution with a new non-invasive optical device LIPOMETER," *Americal Journal of Human Biology* **12**, 221-230 (2000).
34. F. M. Hendriks, D. Brokken, J. T. W. M. van Eemeren, C. W. J. Oomens, F. P. T. Baaijens, and J. B. A. M. Horsten, "A numerical-experimental method to characterize the non-linear mechanical behavior of human skin," *Skin Res. Technol.* **9**, 274-283 (2003).

An elastography framework for use in dermoscopy

Michael I. Miga, Jao J. Ou, Darrel L. Ellis
Vanderbilt University
Vanderbilt University Medical Center
February 20, 2007



Skin Cancer & Significance

- Typical Discerned Facts for Skin Cancer:
 - 3 types – basal cell carcinoma (BCC), squamous cell carcinoma (SCC), and melanoma
 - 1,000,000+ new cases are diagnosed each year
 - 800,000+ BCCs, 200,000+ SCCs, 60,000+ melanomas
 - Annually, melanoma ranks 6th highest among newly diagnosed cancers
 - Melanoma is most lethal
 - Skin lesion scoring for monitoring (ABCDE, etc.)
 - Diagnosis is performed by biopsy
 - **Skin cancer is rarely fatal and is largely treatable**

If so, why pursue this?



Skin Cancer & Significance

- Less Discerned Facts for Skin Cancer:
 - **1,000,000+ newly diagnosed skin cancers involve an estimated 5-7 million biopsies**
 - **Management of NMSC is considerable**

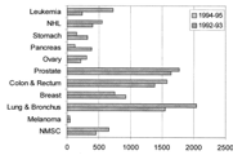


Fig. 4. Mean cost to Medicare in millions of US dollars per cancer for 1992 to 1993 and 1994 to 1995. NHL, Non-Hodgkin's lymphoma; NMSC, non-melanoma skin cancer.
Housman et al., *Journal of the American Academy of Dermatology*, vol. 48, pp. 425-429, Mar 2003.



Skin Cancer & Significance

- Green et al., *Dermatologic Surgery*, vol. 30, pp. 1208-1209, Sep 2004.
 - 22 Dermatologists participated to determine how many biopsies taken were cancerous
 - "Malignancy ratio" (# of malignant biopsies to total biopsies performed)
 - Findings:
 - 40% mean malignancy ratio (ratios varied greatly 13-85%)
 - Age correlated with better malignancy ratio's (2% increase with year of experience)

Annual biopsy costs are in the \$100's of millions



Motivation

- Total direct cancer costs are approximately 78.2 billion per year
- If a low-cost dermoscopic probe, with elastographic imaging capabilities was to have high sensitivity and specificity for skin cancers, this would translate to a significant reduction in health care expenditure.
- **While skin cancer may lack significance in lethality, it is quite significant with respect to healthcare costs.**

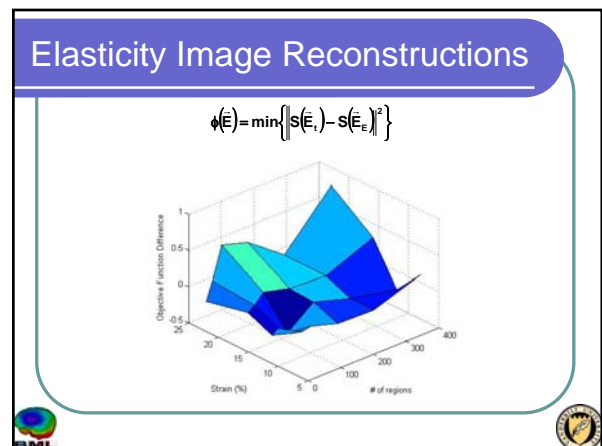
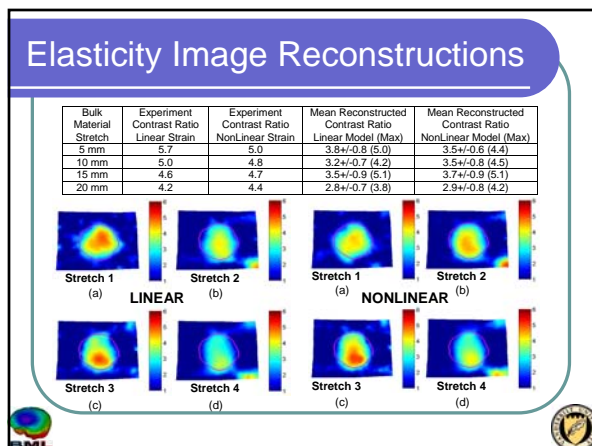
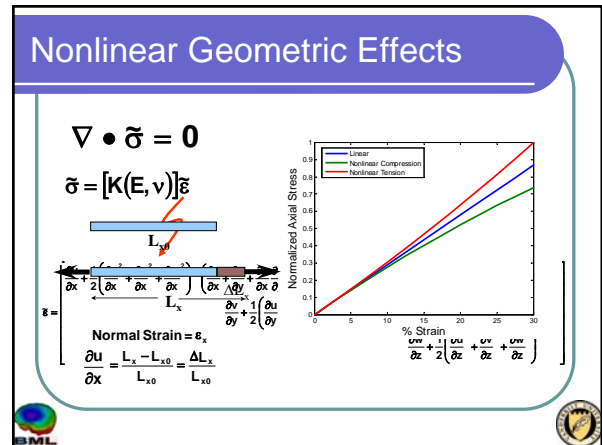
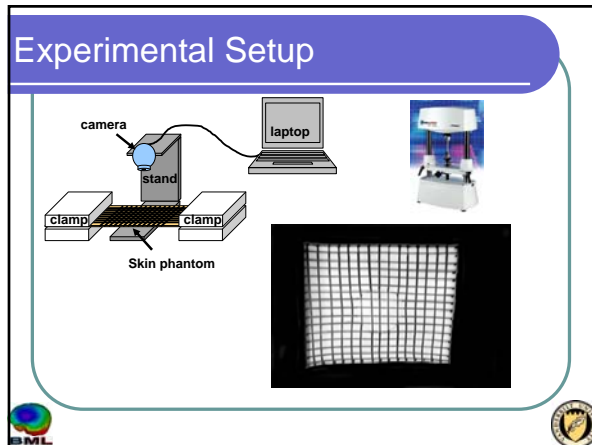
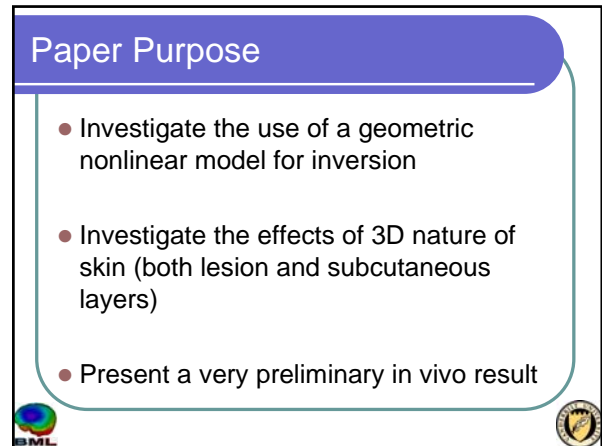
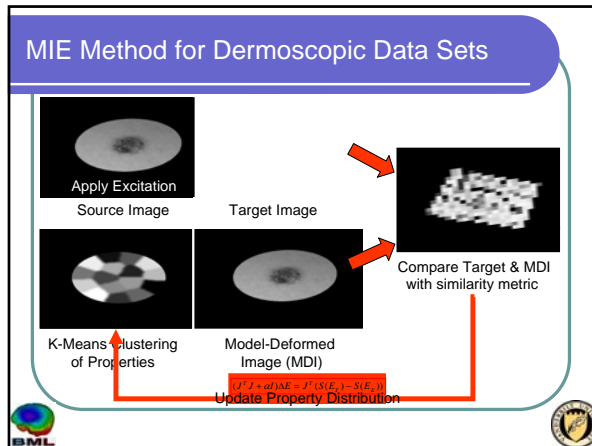


Elasticity Imaging Approach

- Computational Modeling
 - Patient-specific finite element models
 - Physics-based simulations and image deformation
- Image Similarity
 - Metrics of image comparison
- Non-linear Optimization
 - Cornerstone in model-based image reconstruction methods
 - Inverse problem

A Modality Independent Elastography (MIE)





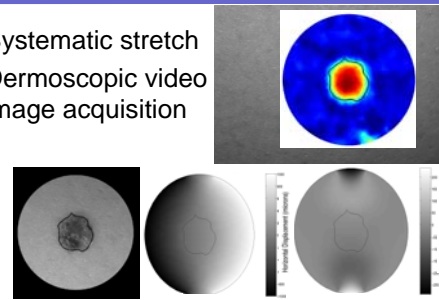
Paper Purpose

- Investigate the use of a geometric nonlinear model for inversion
- Investigate the effects of 3D nature of skin (both lesion and subcutaneous layers)
- Present a very preliminary in vivo result

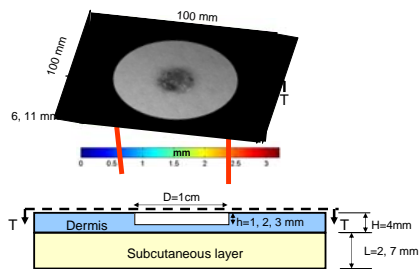


Simulation Setup

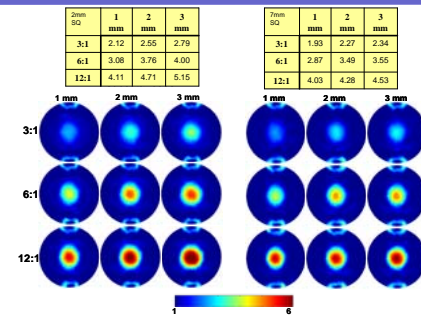
- Systematic stretch
- Dermoscopic video image acquisition



3D Effects Investigation



Results



Paper Purpose

- Investigate the use of a geometric nonlinear model for inversion
- Investigate the effects of 3D nature of skin (both lesion and subcutaneous layers)
- Present a very preliminary in vivo result

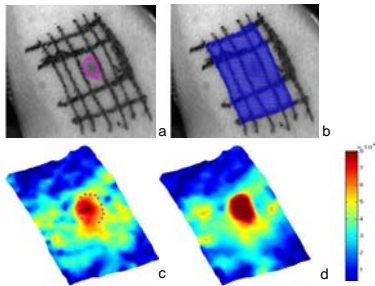


Investigating In Vivo

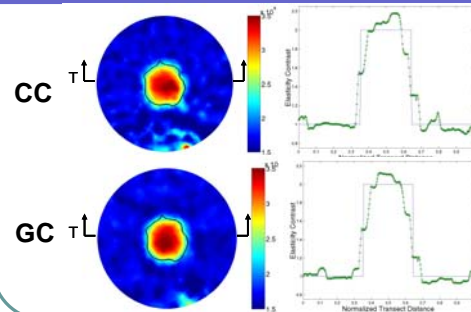
- Spring-loaded grips bounded to the skin with adhesive



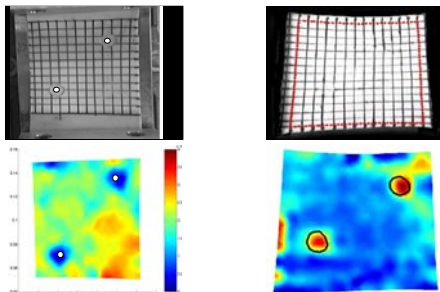
Results



Results



Other Membrane Experiments



Conclusions

- Geometric nonlinear effects are mild
 - Boundary conditions are likely to be the most important aspect
 - 5-10% improvement in objective function value
 - Qualitative improvement in lesion border
- Material nonlinearities are next step
- Subcutaneous layers have little effect
- Depth differentiation with contrast
 - Overlap in contrast may be problem
- In vivo results indicate a nevus lesion has increased stiffness

Future Work

- Device
- MIE's robustness
- Integration
- 3D Extension

An Evaluation of 3D Modality Independent Elastography Robustness to Boundary Condition Noise

Jao J. Ou*, Rowena E. Ong, Michael I. Miga*

{jao.ou,rowena.ong,michael.i.miga}@vanderbilt.edu

Vanderbilt University, Department of Biomedical Engineering, Nashville, TN 37235

ABSTRACT

This work explores an inverse problem technique of extracting soft tissue elasticity information via nonrigid model-based image registration. The algorithm uses the elastic properties of the tissue in a biomechanical model to achieve maximal similarity between image data acquired under different states of loading. A framework capable of handling fully three-dimensional models and image data has been recently developed utilizing parallel computing and iterative sparse matrix solvers. For this preliminary investigation, a series of simulation experiments with clinical image data of human breast are used to test the robustness of the algorithm to expected mis-estimation of displacement boundary conditions encountered in real-world situations. Three methods of automated point correspondence are also examined as means of generating boundary conditions for the algorithm.

Keywords: elastography, computational modeling, inverse problem, non-rigid registration

1. INTRODUCTION

The characterization of the mechanical properties of tissue is an important potential source of information for detection and diagnosis of disease processes. For example, there is a long-standing clinical appreciation of evaluating tissue elasticity through palpation in the physical examination and correlating differences in stiffness with possible pathological states. A minimally invasive methodology for analyzing tissue deformation through imaging and/or image processing techniques is a central goal of the field of elastography [1,11]. Application of such methods to the interrogation of the breast [2,3], skin [4-6], prostate [7], and other accessible organ systems is an active area of research.

Many of the current elastography methods are founded in ultrasound (US) and magnetic resonance (MR) imaging and involve the estimation of induced displacements within the tissue of interest to infer the elasticity distribution. We have recast the problem as a physically-constrained non-rigid image registration utilizing quasi-static deformation and image similarity metrics that reconstruct the spatial distribution of elasticity parameters. This technique has been termed 'modality-independent elastography' (MIE) [8-10] because of its ability to handle native anatomical images from different sources with relatively simple modifications to the acquisition procedure. To date, data from MR, X-ray computed tomography (CT), and digital photography have been used to drive the algorithm. In addition to the necessary preparation and effort involved in gathering images, the other major input to this reconstruction method is the delineation of boundary conditions on the region of interest. Because this process currently involves varying levels of manual interaction, there is a need to develop a protocol that is both effective and mostly automated for determining point correspondences. The objectives of this work are to test the effects of degradation in input data quality on the end reconstruction and examine candidate methods for generation of displacement boundary conditions. This is done in the context of evaluating the robustness of a newly realized three-dimensional version of MIE by performing simulation experiments with randomized noise processes and comparing the fidelity of reconstructions resulting from boundary conditions generated by three different techniques of determining surface point correspondence.

2. METHODS

2.1 Elastographic reconstruction framework

The conceptual framework for our elastographic reconstruction has been previously described in [6,8-10]. In brief, an image of a tissue of interest (*source*) is deformed by a biomechanical computer model and compared against an acquired image of the same tissue in a mechanically loaded state (*target*). Iterative updates of elasticity parameters to the model

are performed until a suitable match in intramodal image similarity is achieved in a least squares manner to satisfy a non-linear optimization scheme. This process can be classified as an inverse problem, with model-based deformation of the source image representing the forward problem. The three major components of the algorithm are the model, image comparison, and optimization, each of which is described in more detail below.

The partial differential equation that expresses a state of mechanical equilibrium can be written as [12]:

$$\nabla \cdot \sigma = 0 \quad (1)$$

where σ is the Cartesian stress tensor. We have elected to model the constitutive tissue behavior using Hooke's Law of linear elasticity, which states that the strain is proportional to the applied stress, and assume that materials are isotropic and incompressible in nature. This leads to the formulation of Cauchy's Law as

$$\begin{pmatrix} \epsilon_{xx} \\ \epsilon_{yy} \\ \epsilon_{zz} \\ \epsilon_{xy} \\ \epsilon_{yz} \\ \epsilon_{xz} \end{pmatrix} = \begin{pmatrix} \frac{\sigma_{xx}}{E} - \frac{\nu}{E}(\sigma_{yy} + \sigma_{zz}) \\ \frac{\sigma_{yy}}{E} - \frac{\nu}{E}(\sigma_{xx} + \sigma_{zz}) \\ \frac{\sigma_{zz}}{E} - \frac{\nu}{E}(\sigma_{xx} + \sigma_{yy}) \\ \frac{\sigma_{xy}}{2G} \\ \frac{\sigma_{yz}}{2G} \\ \frac{\sigma_{xz}}{2G} \end{pmatrix} \quad (2)$$

which describes the constitutive relationship between stress and strain in terms of the elasticity parameters E (Young's modulus) and ν (Poisson's ratio). The shear modulus G is defined as $\frac{E}{2(1+\nu)}$.

A finite element (FE) representation of the model is constructed from the source image and assigned appropriate boundary conditions based on estimated displacement or stress. The standard Galerkin method of weighted residuals [13] is used to construct and solve the system, which yields a set of displacements that are used to deform the source image. This model-deformed image is then compared to the target using an intensity-based image similarity calculated for a series of voxel groupings determined by a downsampling of the image set overlap. The correlation coefficient (CC) [14] is the method of choice, as it has empirically demonstrated superior performance over other metrics such as the sum of squared differences and normalized mutual information.

The elasticity parameter optimization can be written as the minimization of the least squares error objective function

$$\Psi = |S_{TRUE} - S_{EST}|^2 \quad (3)$$

where S_{TRUE} is the set of similarity values achieved when comparing the target image to itself, S_{EST} is the similarity between the model-deformed source and the target images using current estimates of the elastic modulus distribution, and $|\cdot|$ denotes the vector L_2 norm. Note that by definition, S_{TRUE} for CC has a constant value of 1. Using a Levenberg-Marquardt approach, the residual form of equation (3) becomes

$$[J^T J + \alpha I] \{\Delta E\} = [J^T] \{S_{TRUE} - S_{EST}\} \quad (4)$$

where $\mathbf{J} = \partial \mathbf{S}_{\text{EST}} / \partial \mathbf{E}$ is the Jacobian matrix and the regularization parameter α is determined using the methods described in [15]. Modulus values are updated by $\Delta \mathbf{E}$ until an error tolerance is reached or a maximum number of iterations have been completed. Spatial averaging of elasticity values in the model and solution relaxation between iterations are also utilized to improve the stability of the optimization.

It should be noted that the size of the Jacobian matrix is dependent on the number of material properties to be reconstructed, with each column requiring a forward solve of the FE model. For the general lesion detection problem, a fine discretization of the mesh requires many solutions such that the building of this matrix consumes a considerable portion of computational resources. This fact is exacerbated with the use of three-dimensional data and necessitates a parallelized system. Recent work using the Portable Extensible Toolkit for Scientific Computation (PETSc) toolkit [16,17] has provided the necessary coding base for interfacing sparse matrix system solvers with a C/C++ optimization framework in order to supersede the original MATLAB/FORTRAN framework. This new version is designed to scale readily between the complexity of the model and the number of processors available; it has been tested on a homogeneous cluster of ten processors, with further active development taking place in conjunction with the Vanderbilt ACCRE project, which houses hundreds of CPUs.

2.2 Simulation experiment setup

A CT volume of a human breast, obtained from UC-Davis Dept. of Radiology, was used as the source image (256 x 256 x 130, 0.6mm x 0.6mm x 0.6mm voxel spacing) for the remainder of this work. The surface of the breast was segmented (ANALYZE 6.0, Mayo Clinic, Rochester, MN) to create a three-dimensional mesh composed of 39,013 nodes connected as 214,163 tetrahedral elements. In order to ensure initial data fidelity for reconstruction experiments, an idealized target image volume and gold standard boundary condition set were created. A 2-cm spherical tumor was implanted in the center of the mesh by assigning a stiff modulus value to the member elements that was six times higher than the surrounding material [18]. Tissue deformation from the inflation of a rectangular air bladder against the lateral surface of the breast was numerically simulated to qualitatively match observed mechanical loading of an existing device on a breast-mimicking phantom of polyvinyl alcohol cryogel. The stress distribution over a rectangular contact area was modeled as the cross-section of a Gaussian pressure field with its maximum value located at the center of the bladder; the base of the breast was fixed in place as if pinned to the chest wall. The deformation field throughout the domain was calculated using a direct forward solve of the finite element model and then applied to the intensity field of the source image to create a target volume. Displacements at the surface nodes were used to make a final description comprised of all Type I (Dirichlet) boundary conditions. Figure 1 below illustrates the setup of the data used.

All reconstructions were performed using *a priori* knowledge of the location and size of the inclusion in order to limit the scope of the problem (e.g. the expense of the Jacobian matrix) to a two-material discrimination of relative stiffness (elastic contrast). Having a defined physical model and synthetic image comparison also allows for examination of the optimization behavior separately from the other MIE components in order to best evaluate the effect of input inaccuracies on the final elasticity distribution. The reconstruction algorithm begins by assigning a homogeneous elasticity distribution, with Poisson's ratio held constant at $\nu = 0.485$ to represent a nearly incompressible material. For this data set, 733 similarity zones were discretized from the target image volume.

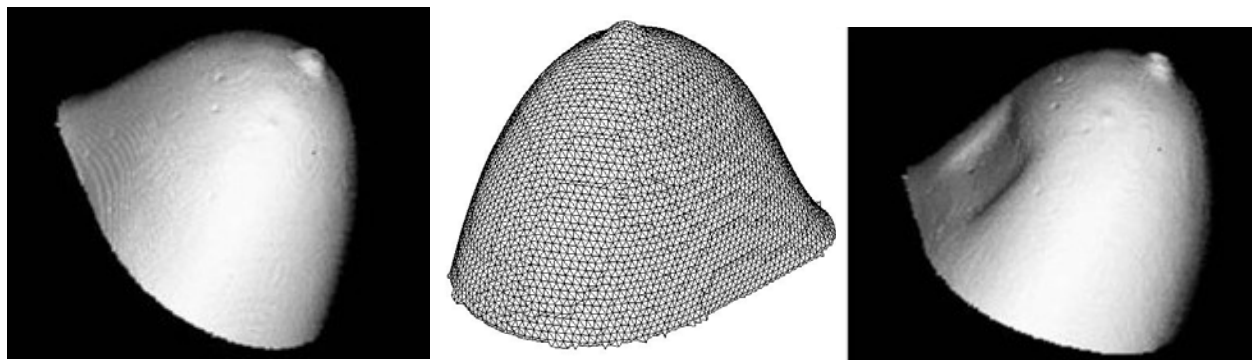


Figure 1. Surface renderings of CT breast volume used in MIE simulation experiments. From left to right: source image, finite element mesh, and target image with deformation created by presumed inflation of an air bladder.

2.3 Testing robustness of the algorithm

The current method of selecting boundary conditions as derived from experiences in 2D work requires manual interaction to guide or correct point correspondence for every surface node. Assuming that visible markers are available in an image, but that an input device (e.g. a mouse) is needed to identify the specific coordinates, this introduces an operator-dependent noise process in localizing any given point. The cumulative effect of these inaccuracies is propagated from the model to the image deformation and then the similarity measurements. For a given reconstruction experiment, the gold standard boundary condition set was systematically disrupted by adding a Gaussian randomized vector of a particular length (0.1, 0.2, 0.5, 1.0 or 2.0 voxel units). Figure 2 shows an example of the distortion caused by the applied noise.

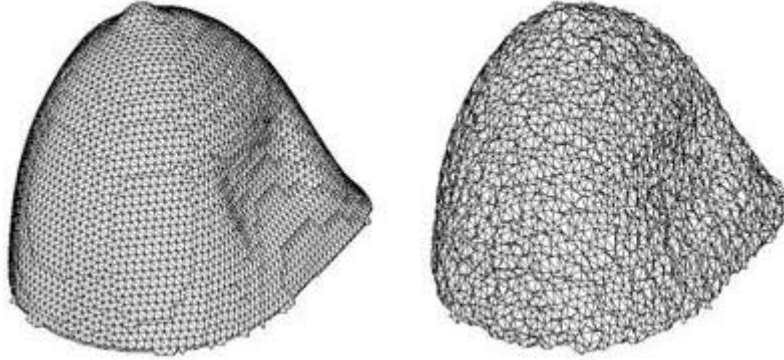


Figure 2. Example of distortion due to additive randomized error. The gold standard boundary conditions used to generate a controlled deformation produce the mesh shown on the left. For effect, the 2.0 voxel unit noise is show on the right.

2.4 Testing automated boundary condition generating methods

For this work, three methods of surface registration and point correspondence were considered for a more automated method of determining boundary conditions for the reconstruction algorithm. Two are derived from surface matching of potential energy distributions, and the other is a free-form warping.

If the flow of a substance over undeformed and deformed breast surfaces is taken to be a conserved process, then correspondence can be achieved by matching the same energy deposition between the source and target, that is, the equivalent level sets. In a physical sense, Laplace's equation can be used to describe this type of movement analogously to steady-state heat distribution:

$$\nabla^2 \Phi = 0 \quad (5)$$

where Φ would represent the temperature over a given region. Similarly, the diffusion equation describes the change in concentration or density of a material over time on a region:

$$\frac{\partial \Phi}{\partial t} = \alpha \nabla^2 \Phi \quad (6)$$

where α is the diffusivity constant.

These partial differential equations were used to calculate an energy distribution from the nipple area to the chest wall over the surface of a breast. Isocontours of particular energy values were then extracted from each surface to form a set of connected points. The symmetric closest point method described by [19] was used to determine a displacement field from which point correspondence at boundary nodes could be interpolated.

The third method involves thin-plate spline interpolation [20] to determine point correspondence. This was done to consider a widely-used method of non-rigid transform that can take advantage of fiducial information that should be present in future real-world data acquisition. The use of physical markers to track breast surface displacement during a deformation also defines a set of control points would allow the displacement boundary conditions for MIE to be simply interpolated from the local warping. In these simulation experiments, 40 surface nodes of known correspondence in each of the image volumes (due to the controlled deformation) served as fiducials.

2.5 Evaluation of reconstructions

Evaluation of the reconstruction results is performed by calculating the ratio of the elasticity of the inclusion to the rest of the breast for the distribution that yields the minimal objective function value over the course of optimization. The robustness of the MIE algorithm was tested with four trials at each of the magnitudes of randomized vectors (described above in Section 2.3), and the reconstruction results were averaged to determine a trend and possible threshold of noise tolerance for the algorithm.

For the automated boundary condition generation methods, a forward mapping of the objective function space was calculated to determine a theoretical optimum to the reconstruction. This was done by calculating the similarity values for model-based image deformations created by adjusting the elasticity contrast of the inclusion over a range of 0.5:1 to 30:1. An interpolating curve was fit and the minimum objective function value and associated elasticity contrast were extracted.

3. RESULTS

3.1 Robustness of algorithm to boundary condition noise

The following tables summarize the effects of additive noise of a particular magnitude to the gold standard boundary condition set. As the magnitude of the applied randomized vectors increased, a dramatic increase in the minimum objective function value is observed. Additionally, changes in the reconstructed elasticity contrast indicate that a cutoff exists in the ability of the algorithm to achieve a successful result (recall that the known correct ratio is 6:1) for disruption by vectors of length 0.5 voxel units or higher.

Table 1. Effect of applied random boundary condition noise on objective function space and reconstructed elasticity contrast ratio.

Randomized vector magnitude (voxel units)	Mean optimal objective function value	Mean optimal elasticity contrast value
0.1	2.85 ± 0.0382	5.62 ± 0.421
0.2	10.1 ± 0.367	5.70 ± 0.588
0.5	60.1 ± 4.19	2.36 ± 0.393
1.0	80.2 ± 0.561	2.47 ± 0.266
2.0	104 ± 3.42	2.17 ± 0.422

3.2 Use of automated point correspondence

Figure 3 depicts the deformation fields found by the various automated methods which were converted into a boundary condition sets and run through the reconstruction algorithm. Qualitatively, the displacements found by the diffusion method are quite different from the gold standard set, while the results from the solution of Laplace's equation and the thin-plate spline interpolation appear to be more satisfactory. The mean target registration error of the three methods confirms this with the spline having the best performance (0.26 mm), the Laplace method next (1.0 mm), and the diffusion method being the worst (2.0 mm). Inspection of Figure 4 further demonstrates that the imposition of an inexact boundary condition set on the model has a distinct effect on the optimization by shifting the minimum value to a different position. A comparison of the fit with the reconstruction in both objective function value and elasticity contrast is provided in Table 3 below and indicates that the algorithm is mostly in agreement with the predicted values for the Laplace and thin-plate spline methods but not as well for the diffusion method.

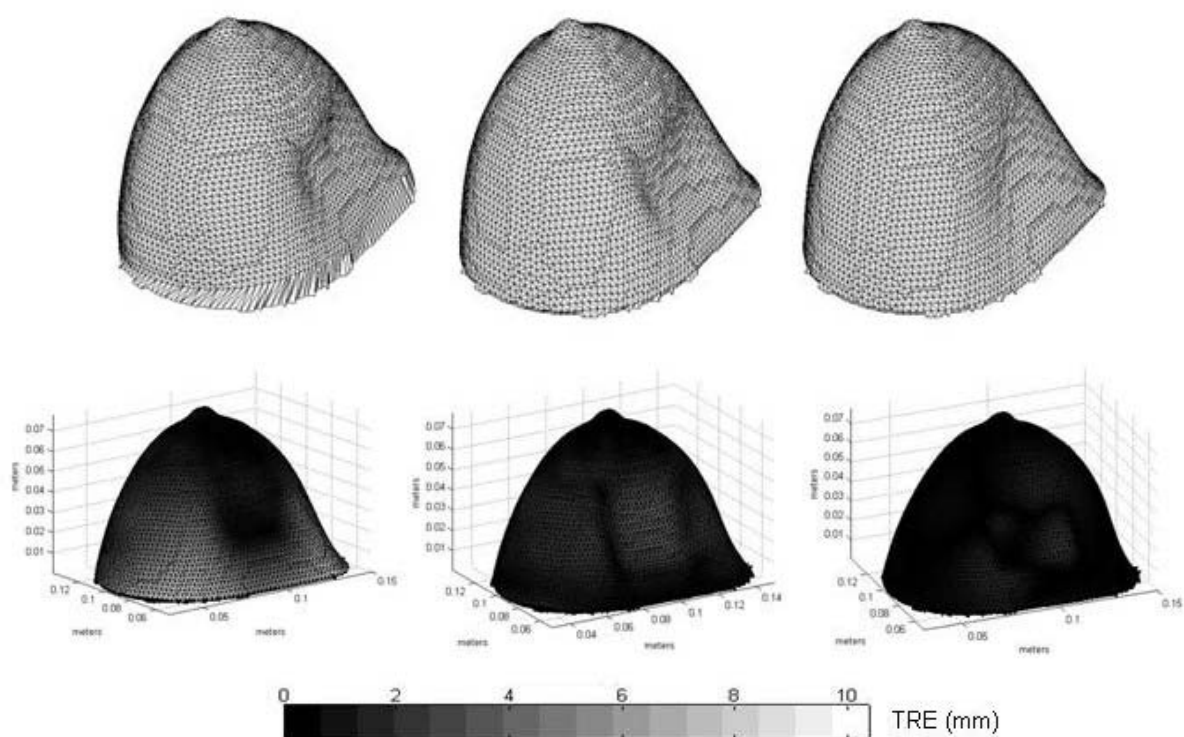


Figure 3. Three candidate automated methods for MIE boundary condition generation. Top row, from left to right: surface deformations calculated from diffusion energy matching, Laplace solution energy, and thin-plate spline interpolation. Bottom row: target registration error (TRE) distribution for each method when compared against the gold standard of known correspondence. The diffusion-based mesh is both qualitatively and quantitatively the worst performer. The Laplace solution appears to capture the shape of the bladder indentation more precisely, but the thin-plate spline has the best overall accuracy in determining point correspondence.

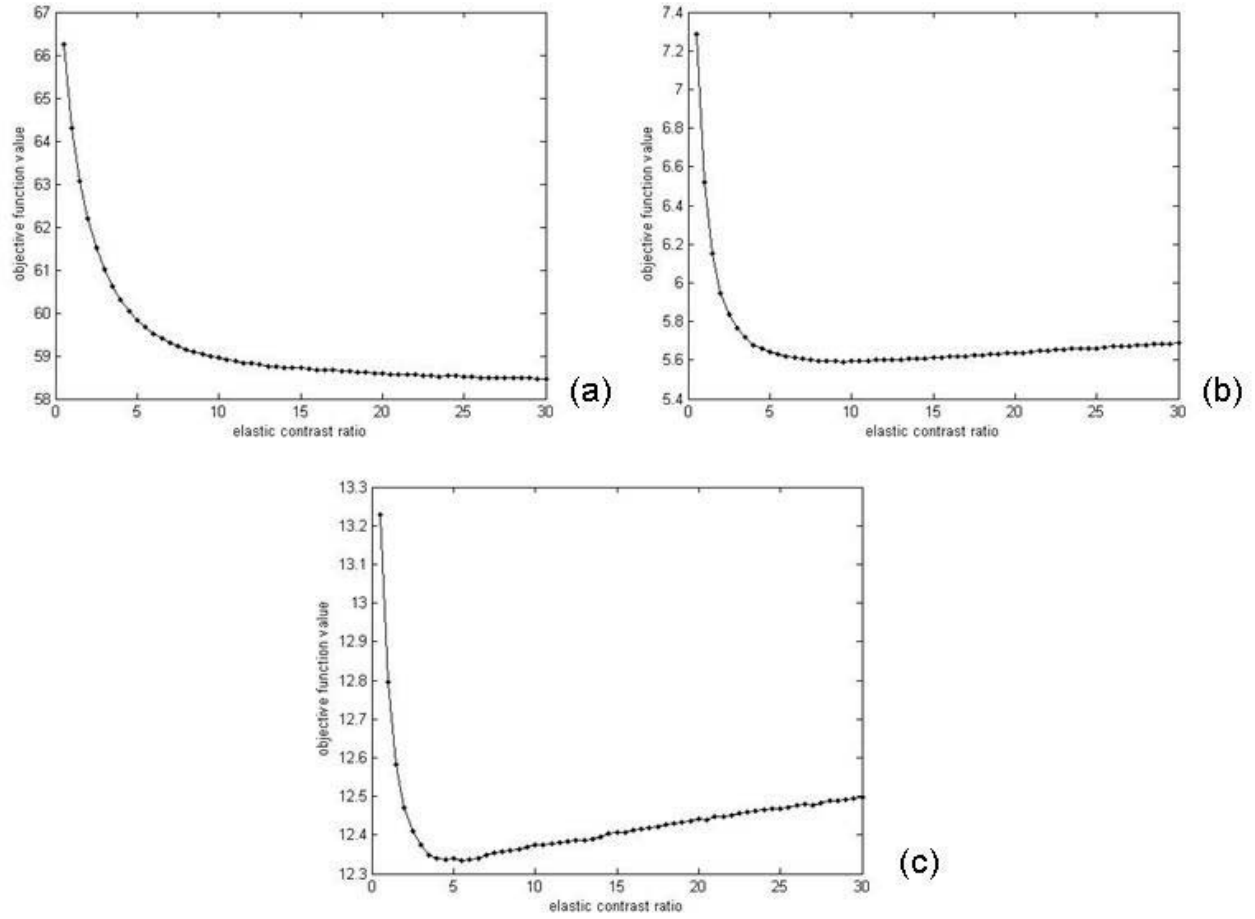


Figure 4. Mappings of objective function value vs. elasticity contrast ratio (tumor:breast) as affected by the boundary condition sets generated by different automated methods of surface point correspondence. The minimum value of each curve corresponds to the optimal elasticity contrast that can be achieved by the algorithm when constrained by the inaccuracies of the methods: (a) diffusion, (b) Laplace, and (c) thin-plate spline interpolations.

Table 3. Comparison of automated point correspondence methods on MIE reconstruction quality. Predicted values are found from the minimum point of the curves shown in Figure 4.

Method	Predicted minimum objective function value	Reconstructed minimum objective function value	Predicted optimal elasticity contrast	Reconstructed optimal elasticity contrast
Diffusion	58.5	58.8	30.0	12.6
Laplace	5.59	5.59	9.55	10.3
Thin-plate spline	12.3	12.3	5.55	5.66

4. DISCUSSION

The results of the boundary condition noise experiment are interesting because they indicate that improper localization of boundary points greater than or equal to 0.5 units of voxel spacing can introduce significant error to the reconstruction process and impair its ability to characterize the underlying elasticity distribution. This is a similar result to prior work done in two-dimensional systems in which successful reconstructions correlated to boundary condition selection error limited to half a pixel length [21]. It also confirms that randomizing the vectors is a significant challenge to the algorithm because it introduces highly non-physical deformations that cause backlash in the finite element mesh and other numerical anomalies.

The implausibility of performing manual selection on all 6,319 boundary nodes underscores the importance of finding an automated method for determining point correspondences, especially at less than 0.5 voxel units of error. In these simulation experiments, energy matching from the solutions of the diffusion and Laplace equations yield boundary condition sets that are inadequate for reconstructing a proper elasticity contrast. This can be partly explained because the mean errors of those surface registration techniques (as compared to the gold standard) are approximately 3.3 and 1.7 voxel units, respectively, which based on the randomized trials were magnitudes too large for the algorithm to handle. The diffusion-based boundary conditions also proved more difficult to obtain a stable solution for in the model, which probably contributed to the mismatch in reconstructed elasticity contrast. However, the results obtained from reconstructions using the thin-plate spline method are encouraging because the mean error was 0.43 voxel units. The reconstruction behavior in that case was consistent with the predicted objective function space and the optimal elasticity contrast was found to be within 6% of the true value. This preliminary result appears to identify the use of thin-plate spline interpolation as a strong candidate for generating boundary conditions for MIE. The use of 40 control points is also seen as a reasonable choice for data acquisition and processing in order to capture the extent of expected deformation processes.

5. CONCLUSIONS

In this work, we have demonstrated the effects of inaccuracies in boundary condition determination on an elastography method that maximizes the similarity between images of a tissue of interest acquired under two different states of mechanical loading. In order to characterize the robustness of the current version of this method, which has been updated to handle three-dimensional data in a parallelized scheme, randomized vectors were applied to distort a gold standard boundary condition set. The results were used to determine a threshold of accuracy needed in order to still achieve an accurate reconstruction. In order to streamline the pre-processing involved in the algorithm, three methods of automated point correspondence were evaluated. The success of these methods correlated with their mean error (relative to the true displacements) meeting the putative cutoff, and initial results indicate that established techniques such as thin-plate splines hold promise for generating boundary conditions.

REFERENCES

1. J. Ophir, I. Cespedes, H. Ponnekanti, Y. Yazdi, and X. Li, "Elastography - a quantitative method for imaging the elasticity of biological tissues," *Ultrasonic Imaging*. 13, 111-134 (1991).
2. A. L. McKnight, J. L. Kugel, P. J. Rossman, A. Manduca, L. C. Hartmann, and R. L. Ehman, "MR elastography of breast cancer: preliminary results," *AJR Am J Roentgenol*. 178(6), 1411-1417 (2002).
3. R. Sinkus, M. Tanter, T. Xydeas, S. Catheline, J. Bercoff, M. Fink, "Viscoelastic shear properties of *in vivo* breast lesions measured by MR elastography," *Magn Reson Imaging*. 23(2), 159-165 (2005).
4. L. V. Tsap, D. B. Goldgof, S. Sarkar, and P. S. Powers, "A vision-based technique for objective assessment of burn scars," *IEEE Trans Med Imaging*. 17, 620-633 (1998).
5. Y. Zhang, D. B. Goldgof, S. Sarkar, and L. V. Tsap, "A modeling approach for burn scar assessment using natural features and elastic property," *IEEE Trans Med Imaging*. 23, 1325-1329 (2004).
6. M. I. Miga, M. P. Rothney, and J. J. Ou, "Modality-independent elastography (MIE): potential applications for dermoscopy," *Medical Physics*. 32, 1308-1320 (2005).

7. L. Curiel, R. Souchon, O. Rouviere, A. Gelet, and J. Y. Chapelon, "Elastography for the follow-up of high-intensity focused ultrasound prostate cancer treatment: initial comparison with MRI," *Ultrasound Med Biol.* 31, 1461-1468 (2005).
8. C. W. Washington and M. I. Miga, "Modality independent elastography (MIE): a new approach to elasticity imaging," *IEEE Trans Med Imaging.* 23, 1117-1128 (2004).
9. M. I. Miga, "A new approach to elastography using mutual information and finite elements," *Phys Med Biol.* 48, 467-480 (2003).
10. M. I. Miga, "A new approach to elastographic imaging: modality independent elastography," *Proceedings of the SPIE.* 4684, 604-611 (2002).
11. K. J. Parker, L. S. Taylor, S. Gracewski, and D. J. Rubens, "A unified view of imaging the elastic properties of tissue," *J Acoustical Soc of America.* 117(5), 2705-2712 (2005).
12. A. Boresi, *Elasticity in Engineering Mechanics*, Wiley-Interscience, 2000.
13. L. Lapidus and G. F. Pinder, *Numerical Solution of Partial Differential Equations in Science and Engineering*, John Wiley & Sons, 1982.
14. J. M. Fitzpatrick, D. L. G. Hill, C. R. Maurer, "Image registration," *Handbook of Medical Imaging*, vol. 2. SPIE Press, 447-513, 2000.
15. N. Joachimowicz, C. Pichot, and J. P. Hugonin, "Inverse scattering: an iterative numerical method for electromagnetic imaging. *IEEE Trans Biomed Engineering*, 39, 1742-1752 (1991).
16. S. Balay, W. D. Gropp, L. C. McInnes, and B. F. Smith, "Efficient management of parallelism in object oriented numerical software libraries," in *Modern Software Tools in Scientific Computing*: Birkhauser Press, 163-202, 1997.
17. S. Balay, K. Buschelman, V. Eijkhout, W. Gropp, D. Kaushik, M. Knepley, L. McInnes, B. Smith, and H. Zhang, "PETSc Users Manual," Argonne National Laboratory, 2004.
18. T. A. Krouskop, T. M. Wheeler, F. Kallel, B. S. Garra, and T. Hall, "Elastic moduli of breast and prostate tissues under compression," *Ultrasonic Imaging.* 20, 260-274 (1998).
19. X. Papademetris, A. J. Sinusas, D. P. Dione, R. T. Constable, and J. S. Duncan, "Estimation of 3-D Left Ventricular Deformation from Medical Images using Biomechanical Models," *IEEE Transactions on Medical Imaging.* 21, 786-800 (2002).
20. A. Goshtasby, "Registration of images with geometric distortions," *IEEE Transactions on Medical Imaging.* 26(1), 60-64 (1988).
21. J. J. Ou, S. L. Barnes, and M. I. Miga, "Preliminary testing of sensitivity to input data quality in an elastographic reconstruction method," *IEEE International Symposium on Biomedical Imaging.* 948-951 (2006).

An Evaluation of 3D Modality Independent Elastography

Robustness to Boundary Condition Noise

Jao J. Ou*, Rowena E. Ong, Michael I. Miga*
Vanderbilt University, Department of Biomedical Engineering, Nashville, TN 37235

BACKGROUND

This work explores an inverse problem technique of extracting soft tissue elasticity information via nonrigid model-based image registration. The algorithm uses the elastic properties of the tissue in a biomechanical model to achieve maximal similarity between image data acquired under different states of loading. A framework capable of handling fully three-dimensional models and image data has been recently developed utilizing parallel computing and iterative sparse matrix solvers. For this preliminary investigation, a series of simulation experiments with clinical image data of human breast are used to test the robustness of the algorithm to expected mis-estimation of displacement boundary conditions encountered in real-world situations. Three methods of automated point correspondence are also examined as means of generating boundary conditions for the algorithm.

METHODS

The conceptual framework for the elastographic reconstruction involves three major components: a biomechanical model of the tissue, image deformation and comparison, and numerical optimization of image similarity. An image of a tissue of interest (*source*) is deformed by a prescribed computational model and compared against an acquired image of the same tissue in a mechanically loaded state (*target*). The deformation and comparison is repeated using systematic updates of elasticity parameters until a suitable match in image similarity is achieved to satisfy a non-linear least squares objective function [1]. Because the goal is to determine a spatial mapping of tissue elasticity, this process can be classified as an inverse problem, with model-based deformation of the source image representing the forward problem. For the current version of MIE, linear elasticity is used as the biomechanical model, the correlation coefficient as the image similarity metric, and a regularized Levenberg-Marquardt algorithm as the optimization method. The constitutive stress-strain relationship of the model is solved using finite elements with the Galerkin method of weighted residuals, and Dirichlet boundary conditions are selected from corresponding points in the image pair.

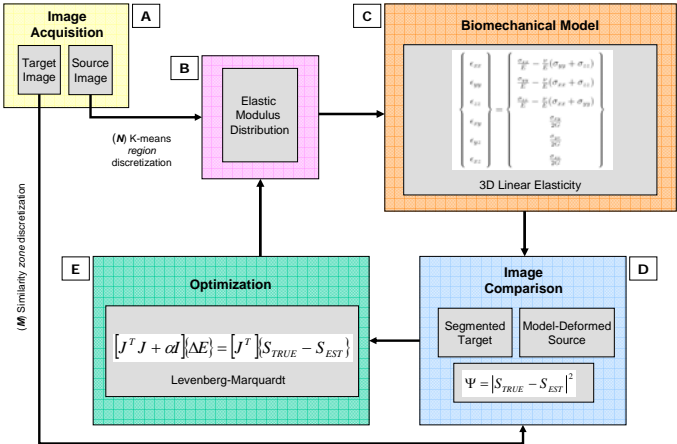


Figure 1. MIE reconstruction algorithm flowchart. After acquisition, source and target images (A) are discretized into regions and zones, respectively. The reconstruction process involves the use of iteratively updated elastic modulus values (B, E) to drive a finite element model-based image deformation (C) until the best match is found (D).

A CT volume of a human breast (obtained from the UC-Davis Dept. of Radiology) was used as the source image for this work. The surface of the breast was segmented to create a mesh composed of 39,013 nodes connected as 214,163 tetrahedral elements. An idealized target image volume and gold standard boundary condition set were created by implanting a 2-cm spherical tumor in the center of the mesh and assigning a stiff modulus value to its member elements that was six times higher than the surrounding material. Tissue deformation from the inflation of a rectangular air bladder against the lateral surface of the breast was numerically simulated to qualitatively match observed mechanically loading behavior of an existing device.

The current method of selecting displacement (Type 1) boundary conditions requires manual interaction to guide or correct point correspondence for every surface node. Assuming that an input device (e.g. a mouse) is needed to identify the specific coordinates, this introduces an operator-dependent noise process in localizing any given point. The cumulative effect of these inaccuracies is propagated from the model to the image deformation and then the similarity measurements. For a given reconstruction experiment, the gold standard boundary condition set was systematically disrupted by adding a Gaussian randomized vector of a particular length (0.1, 0.2, 0.5, 1.0 or 2.0 voxel units). Figure 2 shows an example of the distortion caused by the applied noise, and Table 1 summarizes their effects on reconstructions performed with *a priori* knowledge of the inclusion location.

The implausibility of performing manual selection on all 6,319 surface nodes underscores the importance of developing an automated method for determining boundary conditions. Three methods of surface registration and point correspondence were considered; two are derived from surface matching of potential energy distributions based on the diffusion and Laplace equations, and the other is a free-form warping in the thin-plate spline.

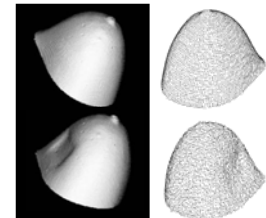


Figure 2. Top row: Surface rendering of source CT breast volume (left) and finite element mesh constructed (right). Bottom row: Target image created by simulated inflation of an air bladder (left) and example of randomized distortion of the true boundary conditions.

Table 1. Effect of applied random boundary condition noise on objective function space and reconstructed elasticity contrast ratio (ideal 6:1).

Randomized vector magnitude (voxel units)	Mean optimal objective function value	Mean optimal elasticity contrast value
0.1	2.85 ± 0.0382	5.62 ± 0.421
0.2	10.1 ± 0.367	5.70 ± 0.588
0.5	60.1 ± 4.19	2.36 ± 0.393
1.0	80.2 ± 0.561	2.47 ± 0.266
2.0	104 ± 3.42	2.17 ± 0.422

RESULTS

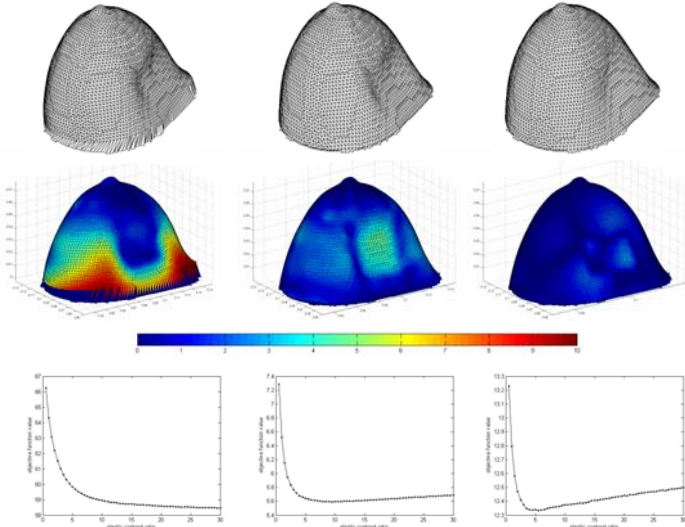


Figure 3. Three candidate automated methods for MIE boundary condition generation. Top row, from left to right: surface deformations calculated from diffusion energy matching, Laplace solution energy, and thin-plate spline interpolation. Middle row: target registration error (TRE) distribution for each method when compared against the gold standard of known correspondence. Bottom row: mappings of objective function value vs. elasticity contrast ratio (tumor:breast) as affected by the boundary condition sets generated by each method. The minimum value of each curve corresponds to the optimal elasticity contrast that can be achieved by the algorithm when constrained by the inaccuracies of the methods. The diffusion-based mesh is both qualitatively and quantitatively the worst performer. The Laplace solution appears to capture the shape of the bladder indentation more precisely, but the thin-plate spline has the best overall accuracy in determining point correspondence.

Table 2. Comparison of automated point correspondence methods on MIE reconstruction quality. Predicted values are found from the minimum point of the curves shown in Figure 3. The ideal (true) elasticity contrast is 6:1.

Method	Predicted minimum objective function value	Reconstructed minimum objective function value	Predicted optimal elasticity contrast	Reconstructed optimal elasticity contrast
Diffusion	58.5	58.8	30.0	12.6
Laplace	5.59	5.59	9.55	10.3
Thin-plate spline	12.3	12.3	5.55	5.66

DISCUSSION

The results of the boundary condition noise experiment indicate that improper localization of boundary points greater than or equal to 0.5 units of voxel spacing can introduce significant error to the reconstruction process and impair its ability to characterize the underlying elasticity distribution. This is a similar result to prior work done in two-dimensional systems in which successful reconstructions correlated to boundary condition selection error limited to half a pixel length [2]. It also confirms that randomizing the vectors is a significant challenge to the algorithm because it introduces highly non-physical deformations that cause backlash in the finite element mesh and other numerical anomalies.

Simulation experiments utilizing automated surface registration and point correspondence methods may then be evaluated in the context of this new criterion. Energy matching from the solutions of the diffusion and Laplace equations yield boundary condition sets that are inadequate for reconstructing a proper elasticity contrast. This can be partly explained because the mean errors of those surface registration techniques (as compared to the gold standard and in an equivalent sense to the tested noise levels) are approximately 3.3 and 1.7 voxel units, respectively, and are far too large for the algorithm to handle. The diffusion-based boundary conditions also proved more difficult to obtain a stable solution for in the model, which probably further contributed to the mismatch in reconstructed elasticity contrast. However, the results obtained using the thin-plate spline method are encouraging because the mean error was 0.43 voxel units, thereby satisfying the threshold while demonstrating reconstruction success. The reconstruction behavior in that case was consistent with the predicted objective function space and the optimal elasticity contrast was found to be within 6% of the true value. This preliminary result appears to identify the use of thin-plate spline interpolation as a strong candidate for generating boundary conditions for MIE. The implementation for that method required the use of 40 control points, which is seen as a reasonable choice in placing fiducials for data acquisition in order to capture the extent of anticipated deformation processes.

REFERENCES

- [1] M. I. Miga, "A new approach to elastography using mutual information and finite elements," *Phys Med Biol.* 48, 467-480 (2003).
- [2] J. J. Ou, S. L. Barnes, and M. I. Miga, "Preliminary testing of sensitivity to input data quality in an elastographic reconstruction method," *IEEE International Symposium on Biomedical Imaging*, 948-951 (2006).

Using Laplace's equation for non-rigid registration of breast surfaces

Rowena E. Ong¹, Jao J. Ou¹, Michael I. Miga^{1,2,*}

¹Vanderbilt University, Department of Biomedical Engineering, Nashville, TN 37235

²Vanderbilt University Medical Center, Department of Radiology and Radiological Sciences,
Nashville, TN 37232

ABSTRACT

Recent advances in breast cancer imaging have generated new ways to characterize the disease. Many analysis techniques require a method for determining correspondence between a pendant breast surface before and after a deformation. In this paper, an automated point correspondence method that uses the surface Laplacian or the diffusion equation coupled to an isocontour matching and interpolation scheme are presented. This method is compared to a TPS interpolation of surface displacements tracked by fiducial markers. The correspondence methods are tested on two realistic finite element simulations of a breast deformation and on a breast phantom. The Laplace correspondence method resulted in a mean TRE ranging from 1.0 to 7.7 mm for deformations ranging from 13 to 33 mm, outperforming the diffusion method. The TPS method, in part because it utilizes fiducial information, performed better than the Laplace method, with mean TRE ranging from 0.3 to 1.9 mm for the same range of deformations. The Laplace and TPS methods have the potential to be used by analyses requiring point correspondence between deforming surfaces.

Keywords: Registration, non-rigid, breast, deformation, correspondence, surface Laplacian, diffusion, finite element, thin-plate spline, interpolation

1. INTRODUCTION

As breast cancer is estimated to kill over 40,000 women and be diagnosed in more than 178,000 in 2007 [1], the detection and treatment of breast cancer is an important area of scientific research. Many novel techniques to aid in tumor detection are being developed that exploit the difference in physical properties between healthy and cancerous tissue. Some of these techniques measure the optical, electrical, or elastic properties of tissue, including near-infrared tomography [6], electrical impedance tomography (EIT) [7], ultrasound elastography (USE) [8], magnetic resonance elastography (MRE) [9], and in particular, modality-independent elastography (MIE) [2,3].

MIE is a reconstruction algorithm for elasticity imaging that can be used for detecting breast tumors. It involves imaging a pendant breast before and after a compression and using these images to reconstruct the elastic properties of the tissue using a nonlinear optimization framework, computer models of soft-tissue deformation, and standard measures of image similarity. Unique to MIE is its ability to utilize images from any modality such as MRI or CT, as well as its usage of image similarity measures that make direct displacement measurements unnecessary.

One requirement of MIE is an automated method of finding point correspondence between the pendant breast surfaces before and after compression, needed to specify the boundary conditions for the elasticity model. As the breast is composed of soft tissue that deforms non-rigidly, standard rigid registration methods cannot be applied. Previous work in non-rigid registration includes using splines and FEM models [11], as well as point-based methods such as the symmetric closest point (SCP) algorithm [10].

In this paper, two automated methods that use the Laplace and diffusion equations to establish point correspondence between deformed breast surfaces were developed and compared to a standard thin-plate spline (TPS) interpolation method [4].

*michael.i.miga@vanderbilt.edu

2. METHODOLOGY

2.1 Laplace and diffusion methods of finding point correspondence

A major investigative task of this work was to evaluate whether the energy distributions modeled by a partial differential equation (PDE) over an undeformed (*source*) surface and a deformed (*target*) surface can be used to find the correspondence between the two surfaces. In this method, the Laplace and diffusion equations were independently solved over the source and target meshes using the finite element method (FEM). Laplace's equation is most commonly used to describe potential flow problems such as in thermal, fluid, and electrostatic systems and is given by

$$\nabla \cdot (\sigma \nabla \Phi) = 0 \quad (1)$$

where Φ represents the potential and σ describes the spatially varying conductivity. The diffusion equation which allows a time-varying potential is given by

$$\frac{d\Phi}{dx} = \nabla \cdot (\alpha \nabla \Phi) \quad (2)$$

where Φ represents the potential and α is the diffusion coefficient. Let Φ_{source} refer to the solution to the Laplace or diffusion equation over the source surface, and let Φ_{target} refer to the solution over the target. The basic premise is that the potential field distributed over the source and target surfaces as calculated by the Laplace or diffusion equation will provide information about the correspondence between the source and target surfaces.

To solve the equations, Dirichlet boundary conditions were set to simulate potential flow from the nipple area to the chest wall over the surface of a pendent breast (specifically, nodes in the nipple and chestwall area were given boundary values of 1 and 0, respectively). To solve equation 1, a Galerkin finite element method is used whereby the equations are expressed along the surface orientation ($\sigma=1$). To solve equation 2, a similar scheme was used for handling the spatial component of the PDE and a fully implicit backwards Euler scheme was used for time-stepping. In the case of equation 2, a no-flux condition was prescribed at the chest wall, and the potential field was allowed to propagate from the nipple ($\alpha=1$). In this calculation, time-stepping was stopped once the potential field reached the chest wall.

After the Laplace or diffusion equation was solved over the source and target surfaces, the solutions were used to establish correspondence between the source and target nodes. This involved two distinct processes: finding correspondence between isocontours of Φ_{source} and Φ_{target} and then "interpolating" that correspondence back to every source node on the mesh. In the first step, isocontours were extracted from Φ_{source} and Φ_{target} for a set of selected isovalues. The correspondence between the source and target isocontours was determined by aligning the contours by their centroids and using the SCP algorithm. In the second step, the displacement vectors at the source isocontours were interpolated to all source nodes using a thin-plate spline. The final correspondence was found by adding these displacements to the source nodes to get the location of the corresponding point on the target surface.

The method can be summarized in the following steps:

1. Obtain the undeformed source mesh and deformed target mesh that define a breast surface before and after deformation.
2. Assign boundary conditions at nipple and/or chest wall nodes.
3. Solve PDE (diffusion or Laplace) over the source and target meshes using FEM.
4. Extract isocontours on the source and target surfaces.
5. Determine point correspondence between source and target isocontours using SCP.
6. Interpolate displacements at source isocontours to all source nodes.

2.2 Using thin-plate spline interpolation to find point correspondence

One advantage of the PDE-based correspondence methods is that they do not explicitly rely on external markers to constrain the matching process. However, when real-world data is acquired, fiducials are anticipated to be available. Therefore, TPS interpolation is another method that can be used to find point correspondence [4]. Although there are many different methods for interpolation, including polynomial splines and B-splines [11], TPS interpolation was chosen in part because it does not require a regular grid, the effects of changing a control point are localized, and it is a standard

method that has been successfully used in many non-rigid registration applications. In the simulation experiments described below, TPS interpolation was used to find point correspondence by choosing 40 points on the source surface to act as fiducials. The known displacements at these nodes were then interpolated to all surface nodes using TPS.

The Laplace, diffusion, and TPS methods for finding point correspondence described above were tested on two simulation data sets and a breast phantom.

2.3 Simulation experiments

To perform a controlled test of the methods described above on a breast-shaped surface, a CT image volume of a pendant breast (courtesy of the Dept. of Radiology, University of California-Davis) was segmented to create a source surface consisting of 6,313 points. Two types of deformations were simulated by assuming different contact geometries of an air bladder being inflated against the breast surface. Circular and rectangular cross-sectional areas of a Gaussian stress distribution positioned along the lateral aspect of the breast were used to define Type 2 boundary conditions for a finite element-based deformation; the base was made to be affixed to the chest wall. The displacement solutions, based on a three-dimensional linear elastic model of a Hookean solid, were applied to create the target surfaces for the two simulations (Figure 1).

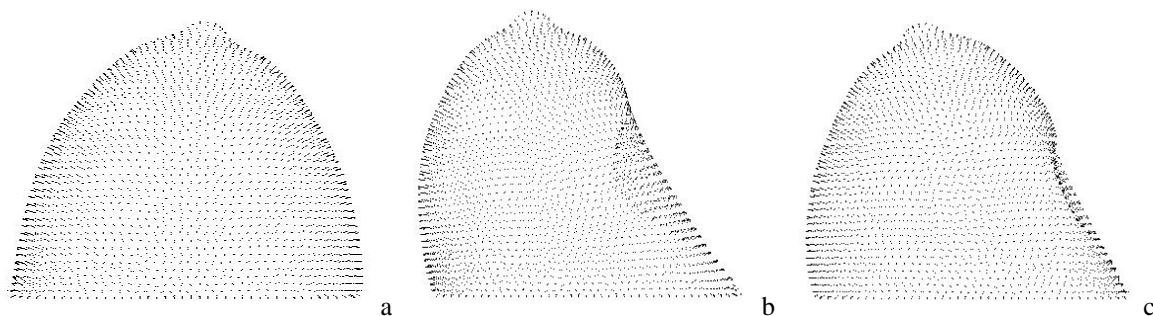


Figure 1. Breast surface point sets. (a) Source surface extracted from CT volume of a breast. (b) Target surface generated from first simulation using circular cross-section of a Gaussian stress distribution. (c) Target surface generated from second simulation using rectangular cross-section of a Gaussian stress distribution. The correspondence between the source and target surfaces was determined using the Laplace, diffusion, and TPS methods.

2.4 Phantom experiments

A breast phantom was constructed to test the point correspondence methods with real-world data. The phantom was fabricated from an 8% w/v solution of polyvinyl alcohol that was frozen in the upper half of a 2-liter beverage container for 16 hours. After 8 hours of thawing, thirty-four 1-mm stainless steel ball bearings were implanted directly under the surface of the resulting cryogel to act as fiducials.

The phantom was then imaged inside a custom-built rectangular chamber designed to deliver compression by means of an air bladder placed against the surface of the phantom (Figure 2). CT images (512 x 512 x 174, 0.54 x 0.54 x 1 mm voxel spacing) were acquired with the phantom at three different states of mechanical deformation (undeformed, 50% of maximum bladder pressure, and full inflation). Triangular surface meshes were obtained by semi-automatic segmentation of the image volumes using the surface extraction tools in ANALYZE 6.0 (Mayo Clinic, Rochester, MN), and the coordinates of the fiducial centroids were localized. These meshes contained approximately 8127, 6777, and 8260 nodes, respectively.

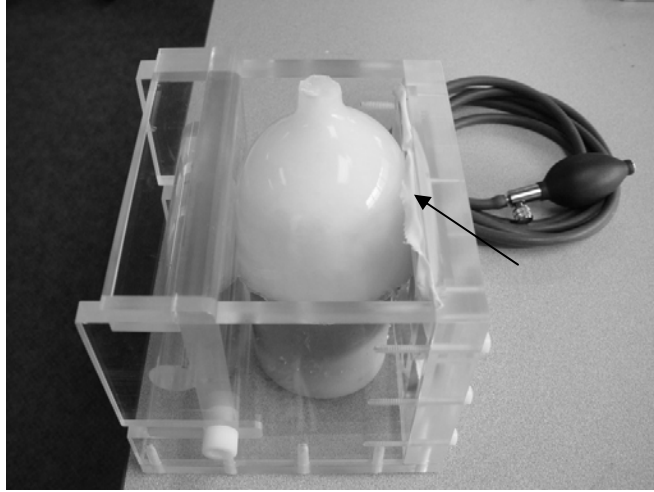


Figure 2. Experimental system for image data acquisition. A polyvinyl alcohol cryogel is placed within a Plexiglas chamber with its surfaces held in place against the walls. Compression is delivered through an air bladder (arrow) inflated manually through a bulb adapted from a standard sphygmomanometer.

The Laplace, diffusion, and TPS methods were tested on the phantom surface meshes. For the TPS method, 30 of the fiducials was used in the interpolation and the four remaining fiducials were reserved for validation. The fiducials used in interpolation and validation were selected such that the distribution for both groups over the surface was roughly even and included the deformed region.

2.5 Validation

In order to assess the accuracy of the simulation and phantom experiments, the target registration error (TRE) was calculated. The TRE measures the error between the correspondence determined by the registration method and the true correspondence [11]. For the simulation experiments, the TRE was calculated as the Euclidean distance between the corresponding target points determined by the Laplace, diffusion, or TPS method and the true target points. Since the true correspondence between the source and target surfaces was known, the TRE was calculated for each source node, and the average and maximum were reported. For the phantom experiment, the TRE was calculated using the centroids of the bead fiducials implanted directly under the phantom surface. Since the “gold standard” correspondence was known only at the fiducials, the TRE could only be calculated at these locations.

In addition, since one crucial step in both the Laplace and diffusion methods is to find point correspondence between the source and target isocontours (step 6 of algorithm summary), we evaluated how well the SCP algorithm performed in this step for the simulation data. To accomplish this, the SCP method was given a set of source isocontours and their true corresponding target contours, and the error (the Euclidean distance between the true target point and the corresponding target point determined by SCP) was calculated.

3. RESULTS

3.1 Simulation 1 (circular deformation source)

The Laplace and diffusion equations were solved over the surfaces generated from simulation 1 (cranial-caudal deformation source with maximum displacement of 33 mm) to find point correspondence between the source and target breast surfaces. For comparison, TPS interpolation using 40 simulated fiducials was also used to find point correspondence. The accuracy of each method was assessed by calculating the TRE at each surface node (Figure 3).

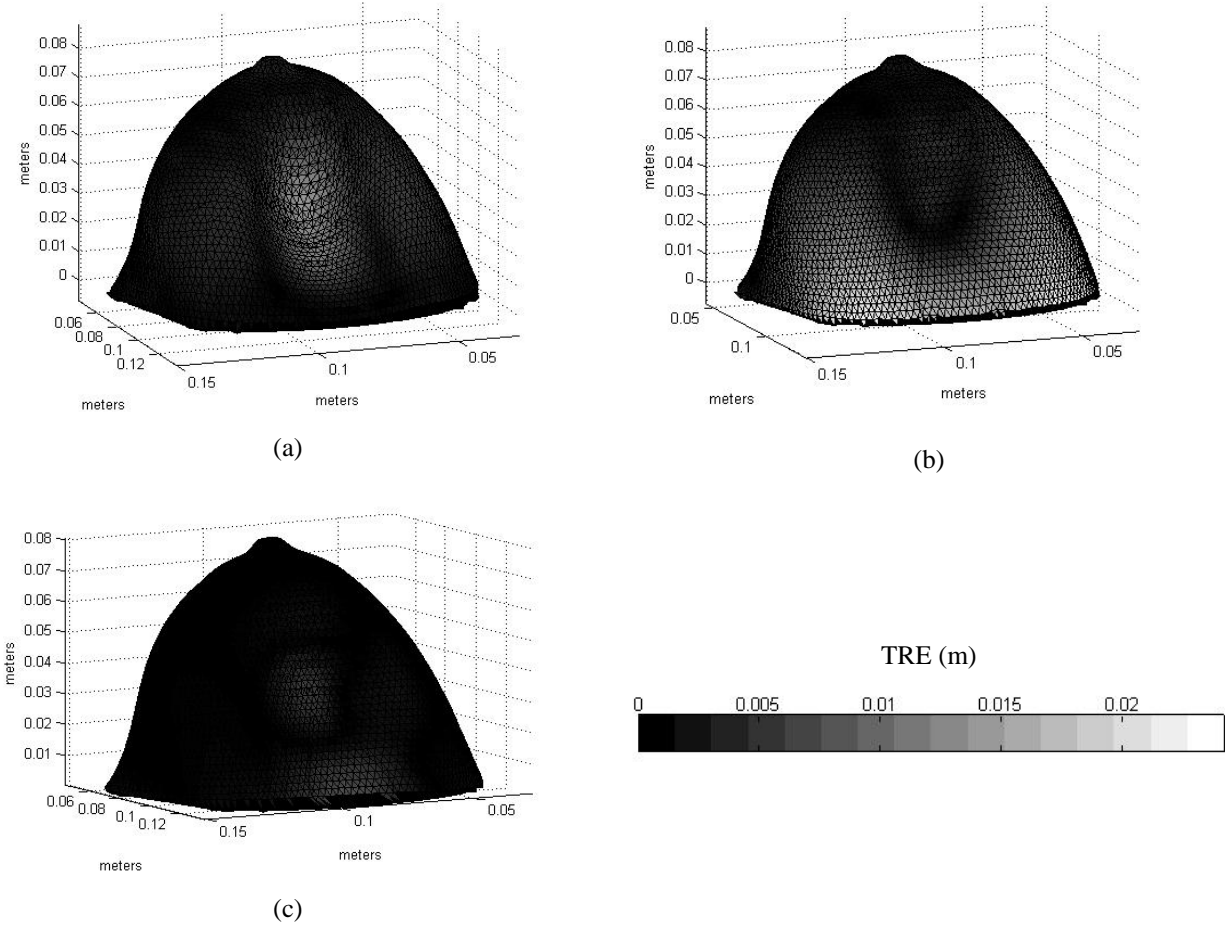


Figure 3. TRE displayed for breast simulation 1 (circular deformation source) when (a) Laplace equation, (b) diffusion equation, and (c) TPS interpolation were used to find point correspondence. The TPS method resulted in the lowest error overall (mean TRE 0.4 mm), followed by the Laplace method (mean TRE 2.3 mm) and diffusion method (max TRE 4.5 mm). The highest TRE is found in the deformed region when the Laplace method is used and in the base when the diffusion method is used.

The results (Table 1) indicated that the Laplace method performed more accurately overall than the diffusion method; however, the area with the highest amount of error differed. When the Laplace method was used, the deformed region had the highest error, whereas when the diffusion method was used, the area farthest from the diffusion source had the highest error. (In this case, since the diffusion source was located in the nipple area, the highest error occurred in the chest wall region.) The TPS interpolation had the lowest error overall, and the error distribution over the surface was related to the locations of the simulated fiducials.

The results given above pertain to a simulated compression with a maximum displacement of approximately 33 mm. Since this amount of compression may be larger than is needed for many applications and may introduce other unwanted effects for MIE due to non-linear elastic behavior, the point correspondence methods were also tested for lesser amounts of compression. The TRE for different amounts of compression when the Laplace method was used to find point correspondence is shown in Figure 4. The TRE appears in Figure 2 and increases linearly with more compression.

The mean and maximum error for the isocontour point correspondence determined by the SCP algorithm (detailed in methods section) was calculated (Figure 5). The isocontour correspondence given by the SCP algorithm had a maximum error of about 5 mm for the maximum compression of 33 m.

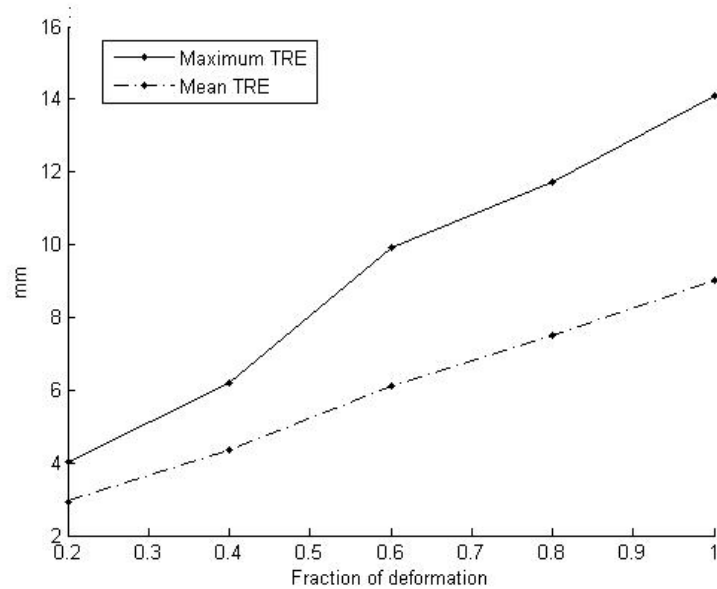


Figure 2. Maximum TRE (solid line) and mean TRE (dotted line) when the Laplace method was used to find point correspondence between the source and target surfaces at different levels of compression. A deformation of 100% indicates a maximum displacement of approximately 33 mm. The TRE seems to increase linearly with respect to the amount of deformation

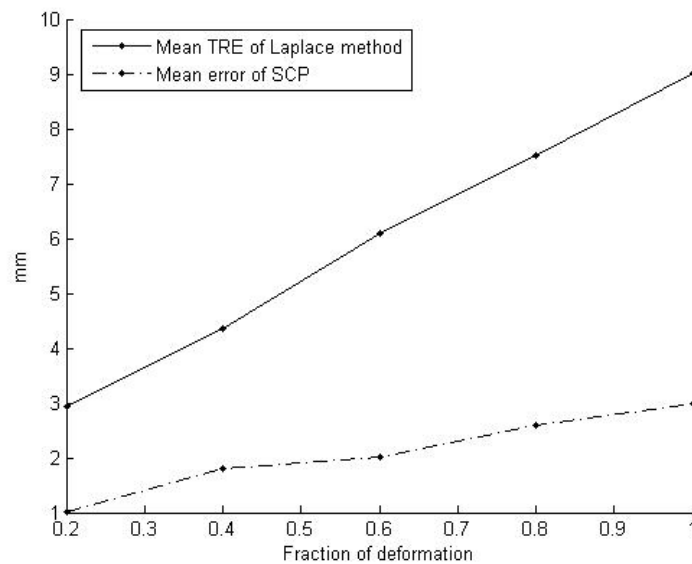


Figure 5. Evaluation of the accuracy of the SCP method used to find isocontour correspondence. The mean error of the SCP method (dotted line) is compared to the mean error of the Laplace method (solid line) when SCP method was used to find isocontour correspondence for simulation 1 data at different levels of compression. (A deformation of 100% indicates a maximum displacement of approximately 33mm.)

3.2 Simulation 2 (rectangular deformation source)

When the Laplace, diffusion, and TPS interpolation methods were used to find point correspondence between the breast surfaces generated by simulation 2 (a more realistic simulation using a rectangular deformation source with a maximum displacement of 13 mm), the results (Figure 6) were very similar to those from simulation 1. However, the TRE for all three methods (Table 1) was slightly lower, possibly due to the lower degree of compression simulated.

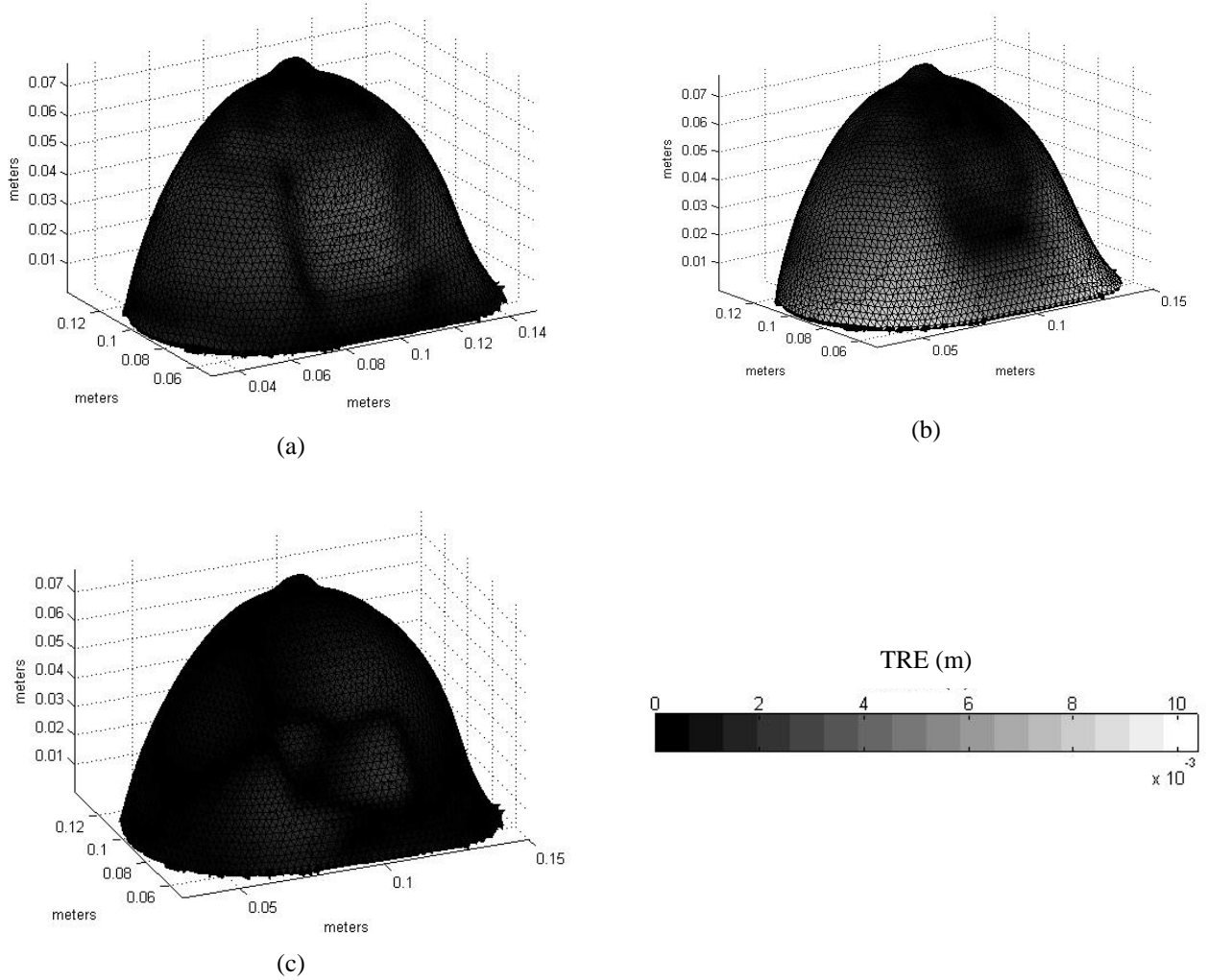


Figure 3. TRE displayed for breast simulation 2 (rectangular deformation source) when (a) Laplace equation, (b) diffusion equation, and (c) TPS interpolation were used to find point correspondence. The TPS method resulted in the lowest error overall (mean TRE 0.3 mm), followed by the Laplace method (mean TRE 1.0 mm) and diffusion method (mean TRE 2.1 mm). The results are similar to that of simulation 1

3.3 Phantom

The Laplace and diffusion methods were used to determine point correspondence between the noncompressed and compressed surfaces of a breast phantom. The results were validated by calculating the TRE at 34 fiducials located directly below the surface of the phantom. For comparison, TPS was used to interpolate the displacements of 30 fiducials to all surface nodes, and the TRE was calculated using the 4 remaining fiducials.

The results for a 50 and 100% compression (with a maximum displacements of about 20mm and 36 mm, respectively) are shown in Table 2. As in the simulations, the Laplace method performed better overall than the diffusion method and had lower TRE. The TRE for the TPS interpolation was lower than that for the Laplace and diffusion methods, but varied with the number and locations of fiducials used in the interpolation.

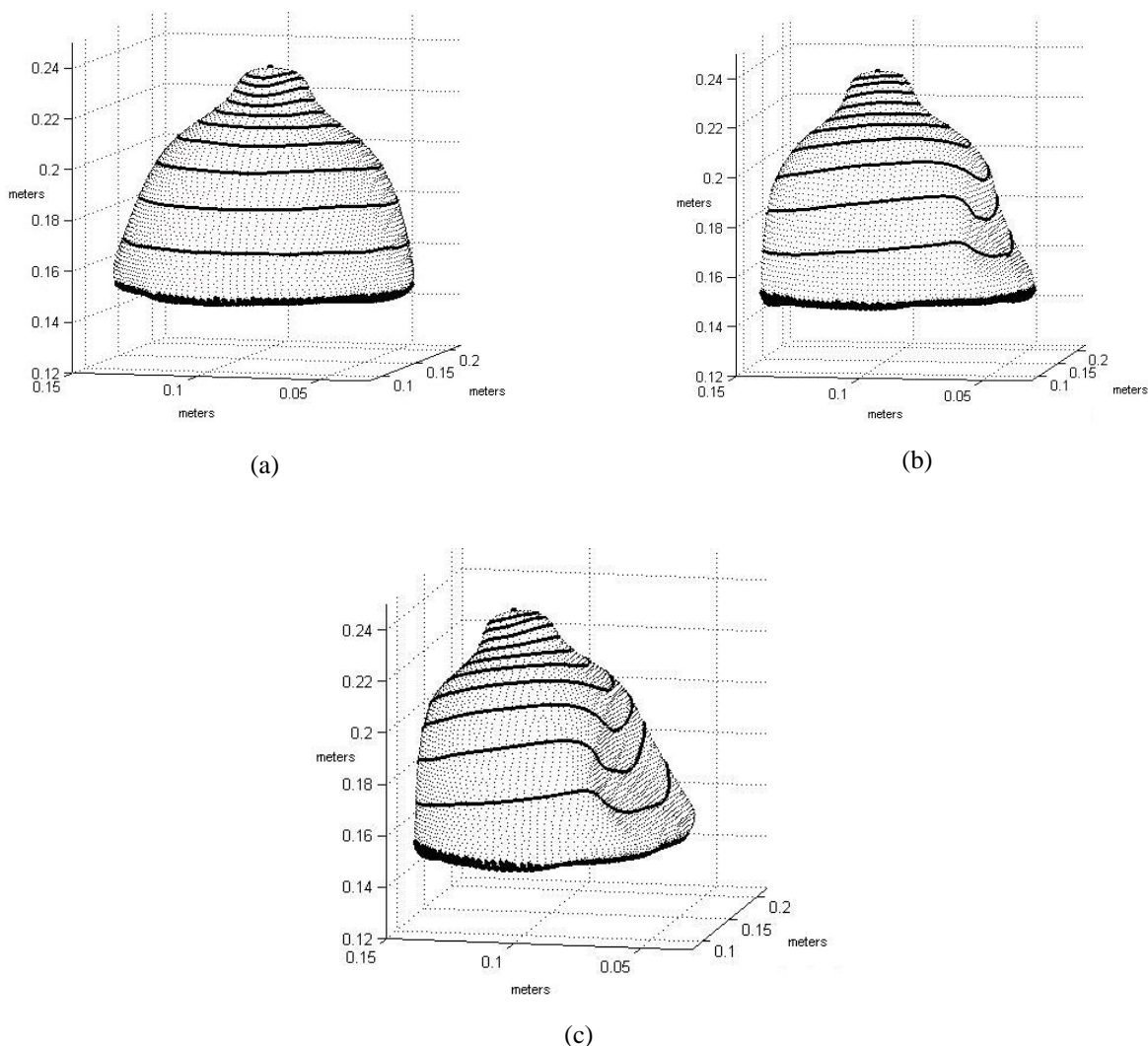


Figure 4. Breast phantom surfaces (a) before compression, (b) at 50% compression with maximum displacement of .020 m, and (c) at 100% compression with maximum displacement of .036 m.) Lines indicate isocontours at different values of k . Black nodes at the nipple and base indicate the nodes assigned boundary values.

Table 1. TRE for different point correspondence methods tested on breast surfaces generated from simulation 1 (point deformation source with max displacement of 33 mm) and simulation 2 (rectangular deformation source with max displacement of 13 mm) breast surfaces. The Laplace method outperformed the diffusion method, while the TPS method performed best of all.

	Simulation 1		Simulation 2	
	Max TRE (mm)	Mean TRE (mm)	Max TRE (mm)	Mean TRE (mm)
Laplace	14.6	2.3	4.6	1.0
Diffusion	24.2	4.5	10.3	2.1
TPS (40 fiducials)	7.6	0.4	2.6	0.3

Table 2. TRE for different point correspondence methods tested on breast phantom at approximately 50% and 100% compression, with max displacements of 20 and 36 mm, respectively. The Laplace method outperformed the diffusion method, while the TPS method performed best of all.

	50% Compression		100% Compression	
	Max TRE (mm)	Mean TRE (mm)	Max TRE (mm)	Mean TRE (mm)
Laplace	8.1	3.5	16.4	7.7
Diffusion	11.9	3.9	19.4	7.9
TPS *	1.5	1.1	2.6	1.9

* TPS interpolation using 30 fiducials; 4 fiducials were used to calculate TRE.

4. DISCUSSION

Of the three registration methods evaluated, the TPS method consistently outperformed the Laplace and diffusion methods and had the lowest error for both the simulation and phantom experiments. However, it is important to note that a comparison of the PDE-based methods and the TPS method is not entirely equal since the TPS method relies on fiducial information that the Laplace and diffusion methods do not require. The performance of the TPS method is dependent on both the number and placement of these fiducials. These results indicate that 30- 40 fiducials with an even distribution over the surface should be sufficient to register surfaces (with 13-33 mm deformations) with mean TRE ranging from 0.3 to 1.9 mm. Although further studies are needed to determine the optimal number and placement of fiducials, experience suggests that increasing the number of fiducials in the areas with greatest deformation increases registration accuracy, and conversely, lowering the number of fiducials in those areas causes a significant decrease in accuracy.

The results indicate that the Laplace method is a useable surface registration method. Although the Laplace method did not perform as accurately as the TPS method, it has the advantage of not requiring fiducial information. However, one of the challenges of the Laplace method is determining the regions to which boundary conditions are assigned. Accurate selection of these regions is important because the implicit correspondence between these regions is used by the Laplace equation to obtain the correspondence for the rest of the surface. For these studies, the nipple region and the chest wall boundary regions were selected manually. Further studies may be needed to find a method to automate the selection of the boundary regions and to evaluate how error in the selection of these regions affects the final registration error.

Although the diffusion method does have certain advantages over the Laplace and TPS registration methods, several problems prevent it from becoming a viable surface registration technique. The advantages of the diffusion method are that the correspondence near to the diffusion source (in this case, the nipple) is relatively accurate. In addition, the diffusion method only requires boundary conditions to be set in one region (in this case, the nipple), unlike the Laplace method, which requires boundary conditions at two regions (nipple and chest wall base), and the TPS method, which requires multiple points of constraint (at 34 fiducials).

However, the diffusion method does not appear to be an effective surface registration method for the following reasons: the results indicate a substantial amount of error, the registration and resulting error are highly dependent on the diffusion parameters chosen (time step and final time in particular), and the diffusion parameters must be manually adjusted for each different surface mesh since there is no automated method to find the optimal diffusion parameters. Since the diffusion described by the PDE is by definition a non steady-state process, an optimal registration requires that the diffusion front should travel over the entire surface between the nipple and base and stop at the base in order to assure correspondence for as much as the surface as possible. If the parameters are chosen such that the diffusion front does not reach the base, the correspondence for the regions not reached by the diffusion front cannot be constrained and must be interpolated from the displacements of the surrounding regions. Conversely, if the diffusion front travels for too long a time, the solution over the surface approaches saturation, resulting in a flat gradient and lack of isocontours from which to establish correspondence. Various modifications to the diffusion method employing curvature information and using different diffusion coefficients were tested, but none were successful. Therefore, the sensitivity of the diffusion method to parameters and substantial amount of error may prevent the diffusion method from being a viable surface registration method.

The TRE measured for each registration technique is not only dependent on the factors described above, but also on the amount of deformation of the target surface. The results suggest that the TRE increases roughly linearly with the amount of deformation. Using the simulation and phantom data presented here, one may be able to estimate the range of error expected when one of the described methods is used to register breast surfaces with a particular amount of compression. Conversely, the maximum amount of compression that will yield a registration within a given error bound can be roughly estimated. For the purposes of MIE, realistic compressions will be in the range of 1-2 cm.

Another factor related to the amount of compression is the distribution of TRE over the surface. The TRE was not evenly distributed; rather, the TRE in the areas of greatest deformation tended to be higher than the TRE elsewhere. Therefore, the mean TRE is not necessarily the best measure of the TRE over the surface; the max TRE may reflect the error in the deformed regions more accurately.

In addition to the evaluation of the three registration methods, the performance of the SCP algorithm was evaluated since the matching of the isocontours extracted from the source and target surface is a crucial step of the PDE-based registration methods. The results indicate that the amount of error the SCP algorithm contributes to the Laplace and diffusion methods is less significant small when compared to the total TRE (Figure 2) but is not negligible.

In comparison to previous studies, the Laplace method outperformed the modified SCP method implemented by Schuler, et al. The data generated by first simulation described in this paper was also used to test the modified SCP method, and whereas the Laplace method had a maximum error of 14.6 mm for a deformation of 33 mm, the modified SCP method had a maximum error of 27.8 mm [5].

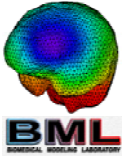
MIE is one application that may use the registration methods described in this paper, in this case to determine boundary conditions for its elasticity model. Preliminary studies indicate that TPS is the most viable registration method, the error of which is within the bounds required for a successful elasticity reconstruction (approximately 0.3 mm). The mean error for the Laplace registration method exceeds MIE's error bounds, and although the target boundary conditions produced the Laplace method resulted in a viable mesh, the resulting elasticity reconstruction contained a considerable amount of error. The diffusion method could not be used in conjunction with MIE because of the extreme distortion of the target finite element mesh generated from the surface registration.

5. CONCLUSION

The results of the simulation and phantom experiments indicate that while TPS interpolation is the most accurate surface registration method of those evaluated, the Laplace method is a viable surface registration technique if fiducials are not available. Although the TPS method consistently outperformed the Laplace method, its performance is dependent on the number and distribution of fiducials available. Both the Laplace and TPS methods have been used in MIE to register breast surfaces in order to determine boundary conditions for its elasticity model. In addition to MIE, the Laplace and TPS methods also have potential to be used for non-rigid registration in more general applications.

6. REFERENCES

1. American Cancer Society, "Cancer Facts and Figures 2007," <http://www.cancer.org/downloads/STT/CAFF2007PWSecured.pdf> (accessed Jan 18, 2007).
2. C. W. Washington and M. Miga, "Modality independent elastography (MIE): a new approach to elasticity imaging," *IEEE Transactions on Medical Imaging*, 23, 1117-28 (2004).
3. M. I. Miga, "A new approach to elastography using mutual information and finite elements," *Physics in Medicine and Biology*, 48, 467-80 (2003).
4. A. Goshtasby, "Registration of images with geometric distortions," *IEEE Transactions on Medical Imaging*, 26(1):60-64 (1988).
5. D. R. Schuler III, J. J. Ou, S. L. Barnes, M. I. Miga, "Automatic surface correspondence methods for a deformed breast," Proceedings of SPIE, Medical Imaging, 2006.
6. B. A. Brooksby, H. Dehghani, B. W. Pogue, and K. D. Paulsen, "Near-infrared (NIR) tomography breast image reconstruction with a priori structural information from MRI: algorithm development for reconstructing heterogeneities," *IEEE Journal of Selected Topics in Quantum Electronics*, 9, 199-209 (2003).
7. H. Frick and S. Morse, "The electrical capacity of tumors of the breast," *Journal of Cancer Research*, 10, 340-76 (1926).
8. T. A. Krouskop, T. M. Wheeler, F. Kallel, B. S. Garra, and T. Hall, "Elastic moduli of breast and prostate tissues under compression," *Ultrasonic Imaging*, 20, 260-74 (1998).
9. Y. Zho and Z. Gho, "A review of electrical impedance techniques for breast cancer detection," *Medical Engineering and Physics*, 25, 79-90 (2003).
10. X. Papademetris, A. J. Sinusas, D. P. Dione, R. T. Constable, and J. S. Duncan, "Estimation of 3-D Left Ventricular Deformation from Medical Images using Biomechanical Models," *IEEE Transactions on Medical Imaging*, 21, 786-800 (2002).
11. J. V. Hajnal, D. L. G. Hill, D. J. Hawkes, *Medical Image Registration*. CRC Press LLC, New York, 2001.



Using Laplace's Equation for Non-Rigid Registration of Breast Surfaces

Rowena E. Ong, Jao J. Ou, Michael I. Miga*

Vanderbilt University, Department of Biomedical Engineering, Nashville, TN 37235



INTRODUCTION

As breast cancer is estimated to kill over 40,000 women in 2007, the detection and treatment of breast cancer is an important area of scientific and medical research. Many novel techniques to aid in tumor detection are being developed that exploit the difference in physical properties between healthy and cancerous tissue. One such method is 'modality-independent elastography' (MIE), which involves an intensity-based non-rigid image registration of a tissue under varying static mechanical loading. In its application for the breast, images acquired before and after a compression can be used to spatially reconstruct the elastic properties of the organ. Therefore, it is critical for the algorithm to have a means of receiving an accurate set of boundary conditions to properly drive the physical model and highly desirable for that process to be as automated as possible. Surface registration and point correspondence techniques are potentially useful for determining displacement-based boundary conditions for MIE. In this work, two semi-automated methods that use the Laplace and diffusion equations to register breast surfaces before and after deformation were developed and compared to a standard thin-plate spline (TPS) interpolation method. Both simulation and phantom studies were used to evaluate the accuracy of these techniques.

METHODS

Laplace/Diffusion Registration Method

In this method, the potential energy field modeled by either the Laplace or diffusion equation over an undeformed source surface and a deformed target surface is used to register the two surfaces.

1. Obtain undeformed source mesh and deformed target mesh that define breast surface before and after deformation.
2. Solve the diffusion or Laplace equation over the source and target meshes using FEM. Laplace's equation is used to describe potential flow in thermal, fluid, and electrostatic systems and is given by:

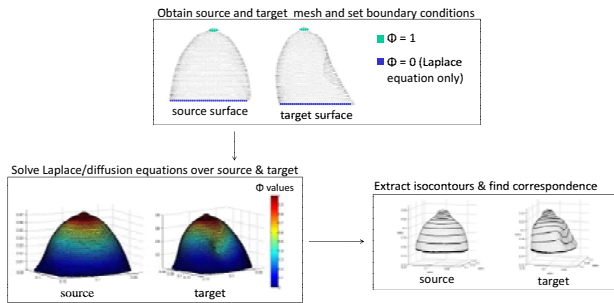
$$\nabla \cdot (\sigma \nabla \Phi) = 0$$

The diffusion equation allows for time-varying potential and is given by

$$\frac{d\Phi}{dx} = \nabla \cdot (\alpha \nabla \Phi)$$

where Φ represents the potential, σ the conductivity, and α the diffusion coefficient. Use following type 1 boundary conditions: set $\Phi=1$ at nipple nodes for both the Laplace and diffusion equations, and set $\Phi=0$ at chest wall for the Laplace equation.

3. Extract isocountours on the source and target surfaces.
4. Determine point correspondence between source and target isocountours using Symmetric Closest Point (SCP).
5. Interpolate displacements at source isocountours to all source nodes.
6. Assess accuracy by calculating the target registration error (TRE). (For the simulations described below, the TRE was calculated at each surface node. For the phantom, the TRE was only calculated at the 34 fiducials.)



Thin-Plate Spline (TPS) Registration Method

TPS interpolation was used to register the two surfaces by interpolating the displacements tracked by control points to all surface nodes. The displacements at each surface node were then used to establish the correspondence between the two surfaces. For the simulations described below, the displacements were interpolated using 40 evenly distributed surface nodes, and the TRE was calculated at each surface node. For the phantom experiment, the displacements at 30 fiducials were interpolated, and the TRE was calculated at the remaining 4 fiducials.

EXPERIMENTAL SETUP

Simulation Experiments

To test these methods, a CT image volume of a pendant breast was segmented to create a source surface. The breast was modeled as 3D linearly elastic, Hookean solid, and two types of deformations were simulated by assuming different contact geometries of an air bladder being inflated against breast surface. The first simulation used a circular cross-section of a Gaussian stress distribution while the second used a rectangular cross-section; the chest wall was fixed for both. The resulting target surface served as the gold standard for error evaluation.

Phantom Experiments

A phantom was fabricated from a polyvinyl alcohol cryogel and 34 1-mm stainless steel ball bearings were implanted directly under the surface to serve as fiducials. The phantom was imaged by CT inside a custom-built rectangular chamber designed to deliver compression through an air bladder (Figure 1), at three different levels of deformation (undeformed, at 50%, and 100% max inflation). Triangular surface meshes and coordinates of the fiducial centroids were obtained and used to test the registration methods.



Figure 1. Compression chamber for breast phantom. Arrow indicates inflation bladder.

RESULTS

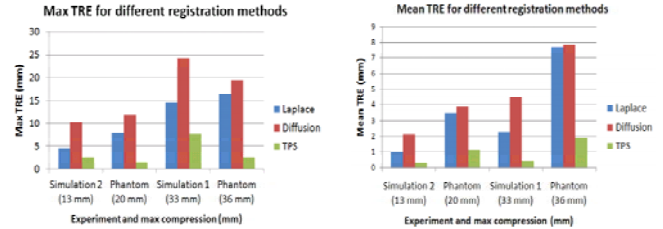
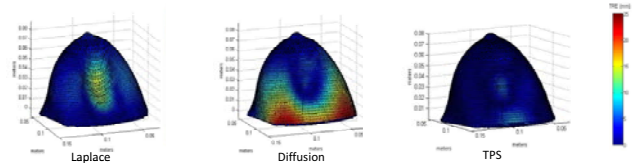


Figure 2. Accuracy of the Laplace, diffusion, and TPS methods when used to register breast surfaces from the simulation and phantom experiments at different levels of compression. The TPS method consistently had the lowest amount of error, followed by the Laplace, and the diffusion method had the highest amount of error. However, note that the TPS method cannot be directly compared to the Laplace and diffusion methods because it utilized fiducial information that the other methods do not require.

Simulation 1 (circular deformation source, max displacement 33 mm)



Simulation 2 (rectangular deformation source, max displacement 13 mm)

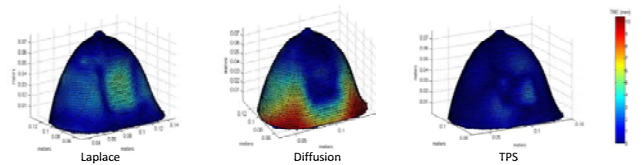


Figure 3. Error distributions (measured by TRE) when the Laplace, diffusion, and TPS methods are used to register breast surfaces from simulation 1 (top row) and simulation 2 (bottom row). The error distributions for simulation 1 and 2 are similar. For the Laplace method, the highest error occurs in the deformed region; for the diffusion method, the highest error occurs near the base. The error distribution for the TPS method varies depending on the placement of the fiducials.

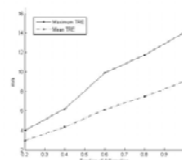


Figure 4. Effects of different levels of compression on the accuracy of Laplace registration. The max and mean TRE when the Laplace method is used to register breast surfaces from simulation 1 at different levels of compression are plotted. The amount of TRE seems to grow linearly with respect to the amount of compression.

CONCLUSION

The results of the simulation and phantom experiments indicate that while TPS interpolation is the most accurate surface registration method of those evaluated, the Laplace method may be a viable non-rigid surface registration technique if fiducials are not available. The diffusion method does not seem to be a usable registration method due to the high error and the difficulty of choosing diffusion parameters. Although the TPS method consistently outperformed the Laplace method, its performance is dependent on the number and distribution of fiducials available. Both the Laplace and TPS methods have been used in MIE to register breast surfaces in order to determine boundary conditions for its elasticity model.

REFERENCES AND ACKNOWLEDGMENTS

- *X. Papademetris, A. J. Sinusas, D. P. Dione, R. T. Constable, and J. S. Duncan, "Estimation of 3-D Left Ventricular Deformation from Medical Images using Biomechanical Models," IEEE Transactions on Medical Imaging, 21, 786-800 (2002).
- *C. W. Washington and M. Miga, "Modality independent elastography (MIE): a new approach to elasticity imaging," IEEE Transactions on Medical Imaging, 23, 1117-28 (2004).
- *A. Goshtasby, "Registration of images with geometric distortions," IEEE Transactions on Medical Imaging, 26(1):60-64 (1988).
- *D. R. Schuler III, J. J. Ou, S. L. Barnes, M. I. Miga, "Automatic surface correspondence methods for a deformed breast," Proceedings of SPIE, Medical Imaging, 2006.
- *H. Q. Dinh, "Implicit Shapes: Reconstruction and Explicit Transformation," Ph.D. Thesis, Georgia Institute of Technology, (2002).

This work was supported by a Whitaker Young Investigator Award.

* michael.i.miga@vanderbilt.edu